FLUORESCENCE IMAGING OF SINGLE MOLECULE ELECTROSTATIC INTERACTIONS

by

Eric M. Peterson

A dissertation submitted to the faculty of
The University of Utah
in partial fulfillment of the requirements for the degree of

Doctor of Philosophy

Department of Chemistry

University of Utah

August 2012

The University of Utah Graduate School

STATEMENT OF DISSERTATION APPROVAL

The dissertation of **Eric M. Peterson**

has been approved by the following supervisory committee members:

Joel M. Harris	, Chair	**5/11/12** Date Approved
Henry S. White	, Member	**5/11/12** Date Approved
John C. Conboy	, Member	**5/11/12** Date Approved
Jennifer Heemstra	, Member	**5/11/12** Date Approved
Steve Blair	, Member	**5/11/12** Date Approved

and by **Henry S. White** , Chair of the Department of **Chemistry**

and by Charles A. Wight, Dean of The Graduate School.

ABSTRACT

In this work, single molecule fluorescence microscopy techniques are used to investigate the role of electrostatics in deoxyribonucleic acid (DNA) hybridization, and in the interactions of DNA and colloidal particles with charged surfaces. Single molecule total internal reflection fluorescence (TIRF) microscopy provides the sensitivity and interfacial specificity needed to probe electrostatic interactions in the microscopic electrical double-layer region between charged molecules and surfaces. Image analysis has been developed to quantitatively detect single molecule spots in TIRF images by sampling their diffraction-limited point-spread function by multiple pixels on the imaging sensor. By detecting spots with multiple pixels above an intensity threshold, single molecules can be located with signal-to-noise ratios as low as 2.5, minimizing false positive and false negative probabilities.

Single molecule imaging was used to monitor the time-course of individual complementary strand DNA hybridization events. Target single stranded DNA (ssDNA) was immobilized at an interface, and its absolute surface density and association constant were determined from the binding isotherm of fluorescently labeled complimentary strand probe ssDNA. Dissociation rate constants of the DNA duplex were determined from the dissociation times, and association rates were calculated from the association constant and the dissociation rate assuming a two-state binding model. From the dependence of association constants, association rates, and dissociation rates on ionic strength, an Eyring model was used to determine the electrostatic contribution to the free energy of the transition state and the fully hybridized double-helix.

The electrostatic interactions between large DNA plasmids and a potential-controlled indium tin oxide (ITO) semiconductor surface were investigated by measuring DNA populations and diffusion near the semiconductor surface as a function of applied potential. DNA populations increased exponentially with positive applied potentials, while maintaining free-solution-like diffusion coefficients and no surface adsorption. A Boltzmann model indicates that interfacial DNA has a net charge less than one electron equivalent, suggesting that much of its charge is screened by counterions. Similar accumulation with increasing positive applied potential was observed with 100 nm carboxylate-polystyrene colloidal particles. These colloidal particles were used to investigate shifts in surface charge of the ITO-aqueous interface induced by photoexcitation of charge carriers in the semiconductor.

TABLE OF CONTENTS

ACKNOWLEGMENTS

I would like to extend my heartfelt thanks to everyone who assisted me over my graduate school career. My advisor, Dr. Joel Harris, was kind enough to welcome me into his group, and he always inspired enthusiasm in any project I was working on. Joel's extensive knowledge of chemistry and optics informed my research, and his clever ideas helped to inspire breakthroughs when progress stalled.

I would also like to thank my fellow Harris group researchers who were always willing to lend their help and answer my questions. Dr. Josh Wayment helped to get my research started by teaching me single molecule fluorescence imaging techniques. Doug Kriech has provided assistance and great conversations about instrument design and surface immobilization chemistry. Prof. Karl-Heinz "Charly" Gerricke and Dr. Moussa Barhoum helped inspire me to write Matlab code and develop the image analysis tools integral to this dissertation. Jonathan Schaefer and Grant Meyers have been fun to work with, and our lively science arguments have inspired great research ideas. Thanks go out to my office mates, Dr. Emily Heider and Justin Cooper, for their patience and company over the years. I also appreciate all the other Harris group members who have helped me, Jay Kitt, Dr. Charlie Ma, Dr. Christopher Fox, Dr. Jennifer Ramirez-Gasser, and Dr. Rory "Ziggy" Uibel.

Finally, I want to thank my lovely wife, Dr. Karen Thomas, for her patience and support as we both navigated graduate school, and my parents and family, who were always there for me.

CHAPTER 1

INTRODUCTION

1.1 Electrostatic Interactions at Interfaces

Electrostatic interactions between polyelectrolyte molecules and charged interfaces are important in many chemical systems. In environmental science, electrostatic interactions influence the adsorption of humic acid to metal oxide surfaces in soils.[1-3] In materials science, the assembly of polyelectrolyte multilayer films is necessary for the fabrication of dye-sensitized solar cells.[4,5] Interfacial electrostatic interactions are especially important in biology, since biological macromolecules, including deoxyribonucleic acid (DNA) and proteins, are typically highly charged polyelectrolytes. Electrostatic repulsion plays an important role in complementary DNA hybridization,[6,7] due to the high charge density on the sugar-phosphate backbone of DNA.[8] Highly charged peptides are thought to induce asymmetry in the composition of phospholipid bilalyer leaflets due to electrostatic interactions with charged phospholipid head groups.[9] In addition, many modern biosensors, including surface plasmon resonance,[10,11] fluorescence,[12-15] nanoaperture enhanced fluorescence,[16] and electrochemical[17,18] biosensors rely on biorecognition events at interfaces, and an understanding of electrostatic interactions with the interface could help to optimize these bioassays.

Electrostatic interactions in aqueous solution are typically only significant over microscopic distances due to screening by ions in solution. Theory developed by Gouy[19]

and Chapman[20] describes the accumulation of ions and the electrical potential profile in a diffuse "double-layer" near a charged interface. In this theory, ionic species "i" with concentration C^0_i in bulk solution and charge z_i accumulate near a charged interface, resulting in a solution charge density profile $\rho(x)$ with distance, x, from the interface according to a Boltzmann distribution, where $\varphi(x)$ is the spatial potential distribution, e is the elementary charge, k is Boltzmann's constant, and T is absolute temperature:

$$\rho_i(x) = ez_iC_i^0 e^{\frac{-ze\varphi(x)}{kT}} \quad 1.1$$

The potential distribution can be related to the charge density, $\rho(x)$, using the Poisson equation, where ε is the relative permittivity of water, and ε_0 is the permittivity of a vacuum:

$$\rho(x) = \varepsilon\varepsilon_0 \frac{d^2\varphi(x)}{dx^2} \quad 1.2$$

Combining these expressions and summing over all ionic species in solution leads to a differential equation for the potential profile in solution:

$$\left(\frac{d\varphi(x)}{dx}\right)^2 = \frac{2kTe}{\varepsilon\varepsilon_0}\sum_i C_i^0 e^{\frac{-ze\varphi(x)}{kT}} \quad 1.3$$

At low surface potentials, φ^0, the solution to this differential equation for a 1:1 electrolyte can be approximated with an exponential decay function:

$$\varphi(x) = \varphi^0 e^{-\kappa x} \quad 1.4$$

Electrical potentials decay into solution over a distance called the Debye length, κ^{-1}, which is inversely proportional to the square root of the electrolyte concentration, C^0:

$$\kappa^{-1} = \left(\frac{2C_0 z^2 e^2}{\varepsilon\varepsilon_0 kT}\right)^{-1/2} \quad 1.5$$

In typical aqueous electrolyte solutions the Debye length is very short, ranging from 10 nm to 0.4 nm for 1 mM and 500 mM ionic strength, respectively. If we wish to study chemical interactions with interfaces over these short length scales, we will require a highly sensitive, surface-specific analytical method.

1.2 Single Molecule Fluorescence Imaging

Over the past 20 years, single molecule fluorescence imaging has been used to investigate a wide range of chemical behavior, from the photophysics of single chromophores[21] to biochemical processes in live cells.[22] Single molecule fluorescence imaging provides a detailed picture of chemical behavior built from observations of individual molecular events, rather than measuring the ensemble average chemical behavior provided by traditional techniques. Single molecule imaging has been used to demonstrate the stochastic stepping movement of myosin molecules on actin filaments, as they consumes individual ATP molecules.[23] Diverse molecular behavior at interfaces, including diffusion,[24,25] peptide binding,[26,27] and complementary strand DNA hybridization,[28,29] has been studied by tracking individual molecules in fluorescence images. In addition, the adsorption and accumulation of individual highly charged biomolecules including DNA[30-32] and peptides[33,34] have been used to investigate the influence of electrical potential at interfaces. Photophysical phenomenon, such as fluorescence resonance energy transfer,[35] and photo-induced electron transfer[36,37] have also been investigated using single molecule techniques. In this work, we have developed single molecule imaging methods which improve molecular quantitation and

allow reliable counting of individual molecules and measuring their residence times in fluorescence imaging data.

1.3 Total Internal Reflection Fluorescence Imaging

To successfully measure chemical phenomenon at a surface, an imaging technique is needed which sensitively probes the interface while excluding unwanted signal from bulk solution. Total internal reflection fluorescence (TIRF) microscopy[38] achieves this goal by confining fluorescence excitation radiation to a thin evanescent field region near a glass-aqueous interface. We have assembled a TIRF microscope in-house which uses through-the-objective total internal reflection illumination as shown in Figure 1.1. The fluorescence excitation source is a gas ion laser coupled into a single-mode optical fiber with a focusing lens. Excitation light from the fiber is collected by a collimating lens and directed through a narrow band-pass filter to remove illumination wavelengths outside the desired excitation band. A final lens then directs the laser beam through a reflection off a high-pass dichroic mirror and focuses it onto the back focal plane of the microscope objective lens. Light from the focused spot is collected by the objective lens, generating a collimated fluorescence excitation beam that illuminates the sample beyond a glass coverslip. Translating the optical fiber normal to the optical axis shifts the angle of the excitation beam relative to the sample plane, and at sufficiently high angles, total internal reflection is achieved. The critical angle, θ_c, needed to achieve total internal reflection at a glass-aqueous interface is determined by Snell's law, microscope objectives, with NA > 1.45, have high acceptance angles, $\theta_{max} = \text{asin}(NA/n_g) > 72°$, able to support an excitation beam impinging on the surface beyond the critical angle. Because the excitation beam is internally reflected at the interface, no propagating

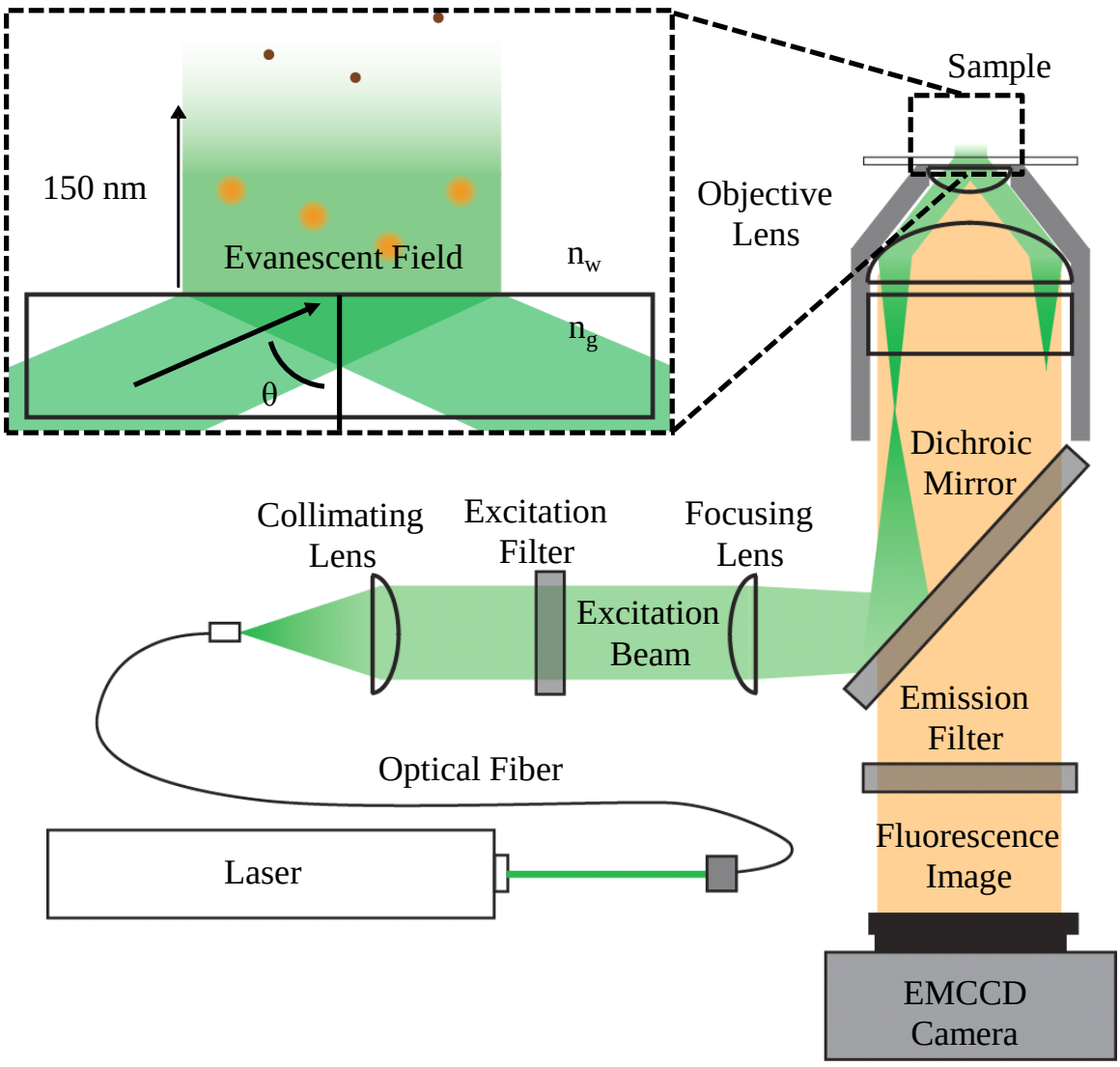

Figure 1.1. Block diagram of through-the-objective TIRF microscope; inset: excitation of fluorescent probes in the evanescent field.

electromagnetic waves illuminate the bulk of the sample. Instead, a non-propagating "evanescent field" is generated which decays exponentially from over ~150 nm into the sample.[39] The evanescent field provides the surface specificity in TIRF microscopy, since only fluorescent molecules that enter the evanescent field region are exposed to excitation radiation and generate fluorescence emission. Fluorescence emission from individual molecules is collected using the same high NA objective lens, passed through a high-pass dichroic mirror and an emission band pass filter to remove excitation radiation, and imaged onto an electron multiplying charge coupled device camera (EMCCD). Using this EMCCD camera, images of single molecules at the interface are collected *in situ*, at real-time imaging rates of up to 50 Hz.

1.4 Quantitative Detection of Single Molecules in Fluorescence Microscopy Images

To extract information about molecular diffusion, residence times and populations at interfaces, we need image analysis methodology able to quantitatively count and track single molecule fluorescence spots. Single molecule spots in images are typically located using two different methods that rely on sampling the finite spatial dimensions of the diffraction-limited point spread function (PSF) by multiple pixel elements on the imaging sensor: PSF fitting and intensity thresholding. Single molecules can be located with high spatial resolution by fitting an empirical function to spots in images; typically a two dimensional Gaussian function[40-42] is used to approximate the Airy-disk point spread function.[43] These methods form the basis of various high resolution imaging techniques, including STORM[44] and PALM,[45] designed to localize molecules to subdiffraction limited resolution by reporting the parameters from a PSF fit. These function fitting

methods have some limitations, however, as the PSF fitting typically requires the use of non-linear least squares algorithms which are prone to random failure, and require moderate signal-to-noise ratios (SNR) of ~5 to implement.[41] In our work, quantitative detection (counting) of single molecules in images with low SNR is more important than locating the molecules with high spatial resolution. In Chapter 2, we outline an image analysis algorithm based on intensity thresholds whose false positive and false negative probabilities can be determined from predictable noise statistics of the background and single molecule intensities respectively, rather than the random failure rate of PSF fitting routines.[46] In this algorithm, single molecules are located by detecting multiple adjacent pixels with photoelectron counts above an intensity threshold, I_{thold}, set n_{std} standard deviation above the mean background intensity, μ_{bg}. By requiring multiple adjacent pixels to be above the intensity threshold, we take advantage of sampling of the PSF by multiple pixels to exclude spurious noise and random cosmic ray events which produce single, isolated intense pixels in images. In addition, the multiple-pixel requirement allows the use of lower intensity thresholds than those required for thresholding individual pixels, since there is a low probability for multiple intense pixels to be in close proximity. The simplicity of this algorithm allowed us to develop an analytical expression which estimates the false positive probability based on the background noise distribution, the number of adjacent pixels detected, and the intensity threshold. This analytical expression for the false positive probability closely matches false positive probabilities measured in simulated images of background noise matching typical blank images.

We verified the effectiveness of the detection algorithm by using it to count rhodamine 6G fluorescent molecule populations deposited by dip coating onto substrates with known, optically-resolvable surface densities .[47,48] Using this deposition method, fluorescent probes were dosed onto glass coverslips by substrate-withdrawal from solutions containing 20 to 200 pM rhodamine 6G in methanol. Molecule surface densities can be estimated by theory by Landau and Levich,[49] which predicts the thickness of the solvent layer adhering to withdrawn substrate based on the solvent properties and withdrawal rate. Surface densities of rhodamine 6G were measured from TIRF images of the dip-coated substrates using the multiple pixel algorithm, and matched densities predicted by the deposition conditions. The false positive detection probability with the detection threshold set only 2.5 times the standard deviations of the background noise was only ~3 molecules per 50 × 50 μm region, which closely matched predictions from simulations of random background noise and the explicit false positive expression for the detection algorithm. False negative probabilities were determined from the intensity distribution of the single molecule "critical pixel," the third most intense pixel, which determines whether the spot exceeds the detection threshold. The false negative rate was determined from the fraction of molecules with critical pixels below the intensity threshold, and was less than 5% in all images.

1.5 Single Molecule Fluorescence Imaging of the Influence of Ionic Strength on DNA Hybridization

In Chapter 3, we use our quantitative single molecule detection methodology to study the influence of ionic strength on complementary strand oligonucleotide hybridization kinetics. Accurate knowledge of DNA hybridization kinetics is integral to

the design and understanding of chip-based DNA sequencing[50,51] and screening[13] applications. Single molecule fluorescence imaging has been proven as a sensitive method to detect DNA hybridization[28,52] and measure hybridization kinetic rates.[29] Kinetic rates determined with binding assays that measure average surface response, including surface plasmon resonance[10,11] and quartz crystal microbalance[7] techniques, are often limited by slow mass transport to the densely packed surface during concentration-step or wash-off experiments. Single molecule techniques avoid transport limitations by measuring kinetics rates under equilibrium conditions, where concentration-steps are not required.

We have developed a single-molecule fluorescence imaging assay for measuring hybridization association constants, K_a, association rate constants, k_{bind} and dissociation rate constants, k_{unb}, between fluorescently-labeled probe and surface-immobilized target 10-mer ssDNA under varying ionic strength, as shown in Figure 1.2. Quantitative single molecule imaging, described in Chapter 2, was used to measure target ssDNA surface populations in response to increasing solution probe ssDNA concentration. The absolute surface density of bound probe molecules from single molecule detection was used to calibrate the fluorescence intensity at high (saturation) coverage, which provided a measurement of the surface density of target ssDNA. The target DNA surface density was used to determine the fraction of sites bound from single molecule populations and calculate the association constant using a Langmuir binding model. Additionally, hybridization kinetic rate constants were determined by measuring the dissociation times of individual double-stranded DNA (dsDNA) complexes. By assuming a bimolecular

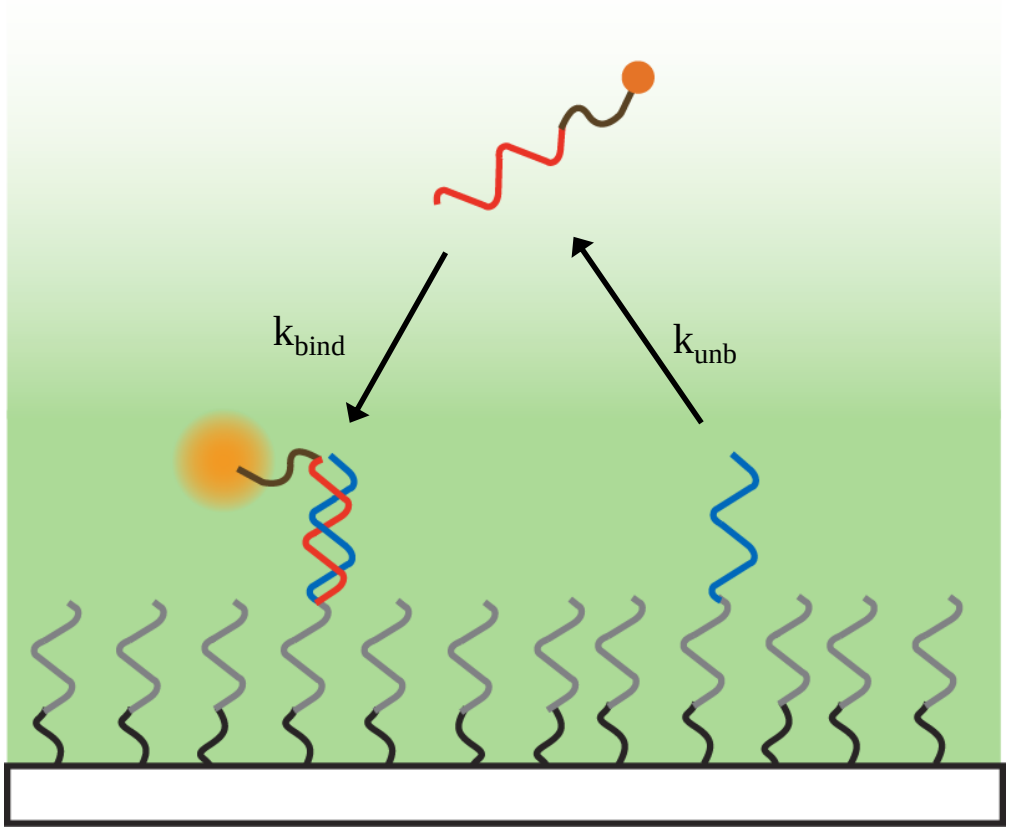

Figure 1.2. Individual DNA hybridization events detected when fluorescently labeled probe DNA associates with target DNA in the evanescent field at the surface, providing association, k_{bind}, and dissociation, k_{unb} rates.

binding model, association rates were determined from the product of the dissociation rate and K_a.

This methodology was used to characterize a 3000-fold increase in K_a upon increasing supporting electrolyte concentration from 25 to 750 mM. Changes in K_a were a result of changes in both the hybridization association and dissociation rates. The association rate dependence on ionic strength was used to model electrostatic and non-electrostatic contributions to the hybridization activation energy and total change in free energy upon association using an Eyring model of the transition state.[53,54] In this model, as ionic strength increases, small ions in solution screen the electrical potential from the charged phosphate-sugar backbones of DNA, reducing the electrostatic barrier to hybridization, and stabilizing the bound complex. The results indicate that at 20 mM ionic strength, the electrostatic repulsion between complementary strands reduces the stability of the bound complex by 20 kJ mol^{-1} compared to 750 mM ionic strength, where electrostatic repulsion is completely screened by electrolyte ions. Similar trends with ionic strength were observed in the activation energy for hybridization, where the electrostatic barrier to association was 12 kJ mol^{-1} higher at 25 mM ionic strength versus 750 mM. Electrostatics influence the total free energy of hybridization more than the hybridization activation energy, suggesting that the hybridized double-stranded DNA complex has more interacting charged bases, or higher effective electrical charge per base than the transition state.

1.6 Imaging of DNA and Colloidal Particles near an Electrical Potential-Controlled Interface

In Chapter 3, the electrical potential difference between individual hybridizing DNA strands could only be imprecisely modulated by varying the solution ionic strength. In Chapter 4, the interfacial population of DNA plasmids is monitored at a potential-controlled transparent electrode interface using TIRF microscopy. This methodology is based on pioneering work by Yeung and Porter, who have used highly charged biomolecules to probe the surface charge of bare glass,[30,55] self-assembled monolayers on gold,[31,56] and transparent carbon electrodes.[32] We investigate electrostatic interactions between a model polyelectrolyte, 15 kilobase double-stranded plasmid DNA labeled with oxazole yellow homodimer fluorescent dye (YOYO-1), and a transparent electrode material, indium tin oxide (ITO), as shown in Figure 1.3. The interfacial population of DNA was monitored under both varying applied electrical potential and ionic strength *in situ* by counting individual plasmids in TIRF images. At applied potentials above 0.7 V versus a Ag/AgCl reference electrode, interfacial DNA populations increased exponentially with increasing applied potential. The population response to the applied potential was interpreted by a simple Poisson-Boltzmann model, which accounts for the potential sensitivity, the potential threshold for accumulation, and the fraction of observed molecules under potential control. The potential sensitivity parameter decreased with increasing supporting electrolyte concentration as expected, due to the decreasing double-layer thickness. Even at the lowest ionic strength, the potential sensitivity corresponded to the plasmid having an effective charge less than one electron, suggesting that nearly all charge on the large DNA is screened by counterions. Diffusion

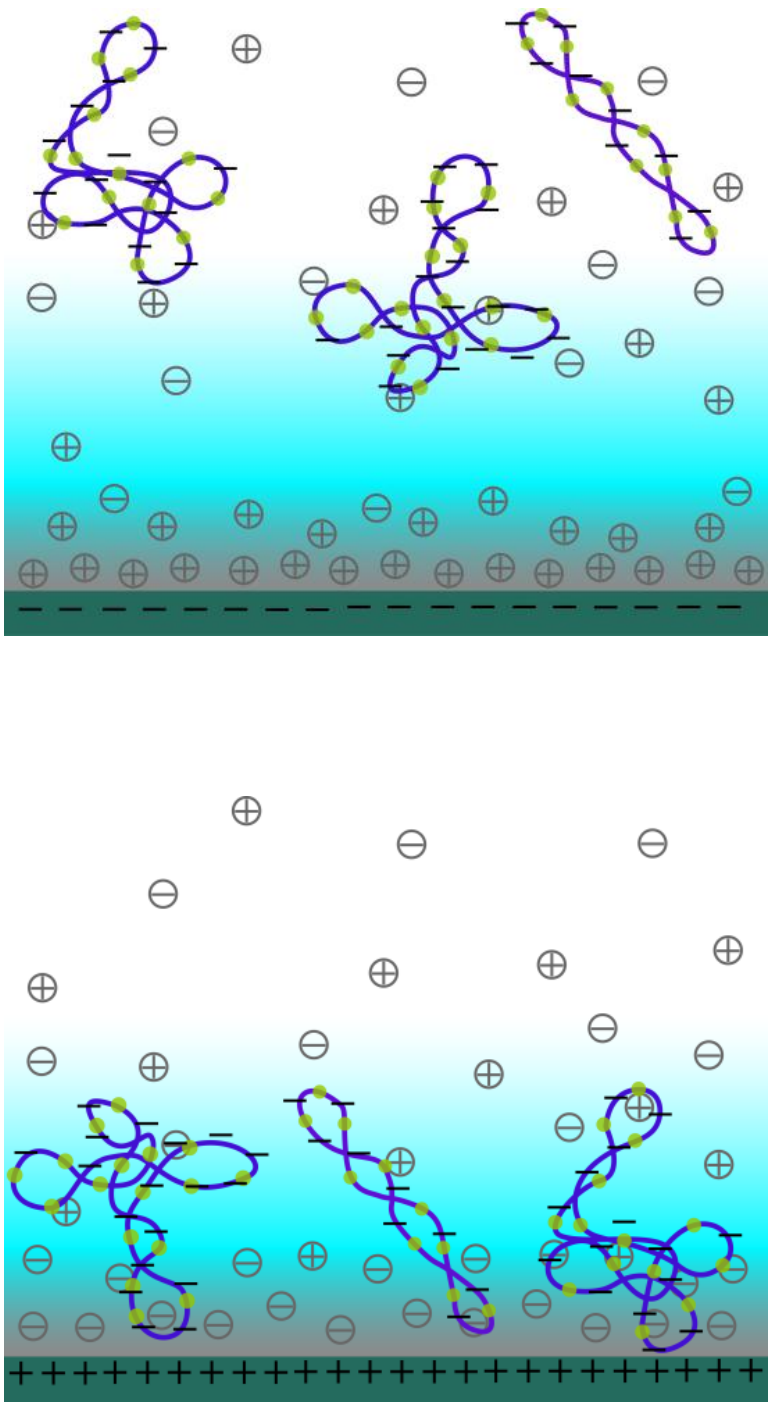

Figure 1.3. Fluorescently labeled DNA plasmids accumulate near electrode surfaces under positive applied potential.

of DNA at the interface was also measured by tracking individual molecules and generating plots of mean squared displacement versus time. The average diffusion coefficient near the interface was close to that in free solution, 1.11×10^{-8} cm^2s^{-1}, and showed no potential dependence. These results indicate that the applied potential does not cause DNA adsorption or interactions with the electrode strong enough to hinder their diffusion, even as the applied potential increased interfacial populations by a factor of 100.

In Chapter 5, the potential response of interfacial populations of charged colloidal particles was used to investigate photoinduced charging of an ITO electrode. Negatively charged carboxylate-polystyrene fluorescent particles accumulated reversibly at the electrode interface in a manner similar to DNA plasmids, and the potential sensitivity and onset potential for their accumulation was well described by the Poisson-Boltzmann model from Chapter 4. These colloidal particles were used to investigate anomalous accumulation behavior observed at the ITO interface, where at applied potentials beyond 0.7 V versus Ag\AgCl, particle populations at the interface increase with the intensity of fluorescence excitation at 488 nm. This anomalous accumulation of particles at the interface was investigated in more detail by measuring interfacial particle populations during potential scans performed at varying excitation intensities. It was observed that the potential sensitivity of particle population showed no dependence on excitation intensity, while the onset potential for particle accumulation shifted ≈ 0.3 V upon increasing the power density from 0.1 to 10 W cm^{-2}. This shift in surface potential was attributed to photoinduced charging of the ITO surface. Because of the relatively low power densities, other photomigration phenomenon, like optical trapping[57] and

photophoresis[58] are unable to account for the observed results. This photoexcitation behavior is surprising, because the excitation radiation, ≈2.4 eV, is lower in photon energy than the primary band gap for ITO, 3.5 to 4.2 eV.[57,58] To investigate the mechanism of photoexcitation, a kinetic model was developed to determine the reaction order of electron-hole generation by photons relative to the second order electron-hole recombination process. From the slope of a log-log plot of the equilibrium surface charge density versus the photon flux, the photoexcitation process was found to be first order with photon flux. This first order process suggests single photon excitation of either the indirect band gap, or defect sites, rather than two-photon excitation of the direct band gap in ITO. The excitation radiation matches an electronic transition measured for ITO which is believed to be either photoexcitation of an indirect band gap, or photoexcitation of lattice defect sites.[59-61] To further test this hypothesis, a control experiment was conducted in which populations of red-fluorescent 200 nm carboxylate-polystyrene particles were tracked versus applied potential using 647 nm excitation intensity between 1 and 15 W cm^{-2}. Illumination with radiation far outside the indirect band gap or defect site energy resulted in negligible shifts of onset potential with illumination intensity, consistent with the photoinduced charge separation hypothesis.

1.7 References

(1) Vermeer, A. W. P.; van Riemsdijk, W. H.; Koopal, L. K. *Langmuir* **1998**, *14*, 2810.

(2) Kaneco, S.; Itoh, K.; Katsumata, H.; Suzuki, T.; Masuyama, K.; Funasaka, K.; Hatano, K.; Ohta, K. *Environmental Science & Technology* **2003**, *37*, 1448.

(3) Weng; Van Riemsdijk, W. H.; Koopal, L. K.; Hiemstra, T. *Environmental Science & Technology* **2006**, *40*, 7494.

(4) He, J.-A.; Mosurkal, R.; Samuelson, L. A.; Li, L.; Kumar, J. *Langmuir* **2003**, *19*, 2169.

(5) Han, J.; Kim, H.; Kim, D. Y.; Jo, S. M.; Jang, S.-Y. *ACS Nano* **2010**, *4*, 3503.

(6) Quartin, R. S.; Wetmur, J. G. *Biochemistry* **1989**, *28*, 1040.

(7) Okahata, Y.; Kawase, M.; Niikura, K.; Ohtake, F.; Furusawa, H.; Ebara, Y. *Analytical Chemistry* **1998**, *70*, 1288.

(8) Ross, P. D.; Scruggs, R. L. **1964**, *2*, 231.

(9) Brown, K. L.; Conboy, J. C. *Journal of the American Chemical Society* **2011**, *133*, 8794.

(10) Altschuh, D.; Dubs, M. C.; Weiss, E.; Zeder-Lutz, G.; Van Regenmortel, M. H. V. *Biochemistry* **1992**, *31*, 6298.

(11) Haeussling, L.; Ringsdorf, H.; Schmitt, F. J.; Knoll, W. *Langmuir* **1991**, *7*, 1837.

(12) Watts, T. H.; Gaub, H. E.; McConnell, H. M. *Nature* **1986**, *320*, 179.

(13) Dalma-Weiszhausz, D. D.; Warrington, J.; Tanimoto, E. Y.; Miyada, C. G. In *Methods in Enzymology*; Alan, K., Brian, O., Eds.; Academic Press: 2006; Vol. Volume 410, p 3.

(14) Kalb, E.; Engel, J.; Tamm, L. K. *Biochemistry* **1990**, *29*, 1607.

(15) Asanov, A. N.; Wilson, W. W.; Oldham, P. B. *Analytical Chemistry* **1998**, *70*, 1156.

(16) Attavar, S.; Diwekar, M.; Blair, S. *Lab on a Chip* **2011**, *11*, 841.

(17) Steel, A. B.; Herne, T. M.; Tarlov, M. J. *Analytical Chemistry* **1998**, *70*, 4670.

(18) Yeung, S. S. W.; Lee, T. M. H.; Hsing, I. M. *Journal of the American Chemical Society* **2006**, *128*, 13374.

(19) Gouy, L. G. *J. Phys.* **1910**, *4*.

(20) Chapman, D. L. *Phil. Mag.* **1913**, *6*, 475.

(21) Zhang, J.; Kuznetsov, A. M.; Medvedev, I. G.; Chi, Q.; Albrecht, T.; Jensen, P. S.; Ulstrup, J. *Chemical Reviews* **2008**, *108*, 2737.

(22) Joo, C.; Balci, H.; Ishitsuka, Y.; Buranachai, C.; Ha, T. *Annual Review of Biochemistry* **2008**, *77*, 51.

(23) Funatsu, T.; Harada, Y.; Tokunaga, M.; Saito, K.; Yanagida, T. *Nature* **1995**, *374*, 555.

(24) Schmidt, T.; Schütz, G. J.; Baumgartner, W.; Gruber, H. J.; Schindler, H. *Proceedings of the National Academy of Sciences of the United States of America* **1996**, *93*, 2926.

(25) McCain, K. S.; Hanley, D. C.; Harris, J. M. *Analytical Chemistry* **2003**, *75*, 4351.

(26) Fox, C. B.; Wayment, J. R.; Myers, G. A.; Endicott, S. K.; Harris, J. M. *Analytical Chemistry* **2009**, *81*, 5130.

(27) Wayment, J. R.; Harris, J. M. *Analytical Chemistry* **2009**, *81*, 336.

(28) Kang, S. H.; Kim, Y. J.; Yeung, E. S. *Analytical and bioanalytical chemistry* **2007**, *387*, 2663.

(29) Jungmann, R.; Steinhauer, C.; Scheible, M.; Kuzyk, A.; Tinnefeld, P.; Simmel, F. C. *Nano Letters* **2010**, *10*, 4756.

(30) He, Y.; Li, H.-W.; Yeung, E. S. *The Journal of Physical Chemistry B* **2005**, *109*, 8820.

(31) Li, H.-W.; Park, H.-Y.; Porter, M. D.; Yeung, E. S. *Analytical Chemistry* **2005**, *77*, 3256.

(32) Donner, S.; Li, H.-W.; Yeung, E. S.; Porter, M. D. *Analytical Chemistry* **2006**, *78*, 2816.

(33) Xu, X.-H. N.; Yeung, E. S. *Science* **1998**, *281*, 1650.

(34) Kang, S. H.; Yeung, E. S. *Analytical Chemistry* **2002**, *74*, 6334.

(35) Ha, T.; Enderle, T.; Ogletree, D. F.; Chemla, D. S.; Selvin, P. R.; Weiss, S. *Proceedings of the National Academy of Sciences* **1996**, *93*, 6264.

(36) Lu, H. P.; Xie, X. S. *The Journal of Physical Chemistry B* **1997**, *101*, 2753.

(37) Palacios, R. E.; Fan, F.-R. F.; Bard, A. J.; Barbara, P. F. *Journal of the American Chemical Society* **2006**, *128*, 9028.

(38) Axelrod, D. *Methods in Cell Biology* **1989**, *30*, 245.

(39) Hansen, W. *Journal of the Optical Society of America* **1968**, *58*, 380.

(40) Michalet, X.; Weiss, S. *Proceedings of the National Academy of Sciences of the United States of America* **2006**, *103*, 4797.

(41) Anthony, S. M.; Granick, S. *Langmuir* **2009**, *25*, 8152.

(42) Ram, S.; Ward, E. S.; Ober, R. J. *Proceedings of the National Academy of Sciences of the United States of America* **2006**, *103*, 4457.

(43) Peter, L. M. *Chemical Reviews* **1990**, *90*, 753.

(44) Swint, A. L.; Bohn, P. W. *Langmuir* **2004**, *20*, 4076.

(45) Donley, C.; Dunphy, D.; Paine, D.; Carter, C.; Nebesny, K.; Lee, P.; Alloway, D.; Armstrong, N. R. *Langmuir* **2001**, *18*, 450.

(46) Peterson, E. M.; Harris, J. M. *Analytical Chemistry* **2009**, *82*, 189.

(47) Hanley, D. C.; Harris, J. M. *Analytical Chemistry* **2001**, *73*, 5030.

(48) Lacy, W. B.; Olson, L. G.; Harris, J. M. *Analytical Chemistry* **1999**, *71*, 2564.

(49) Landau, L.; Levich, B. *Acta Physiochim. U.R.S.S.* **1942**, *17*, 42.

(50) Fritz, J.; Cooper, E. B.; Gaudet, S.; Sorger, P. K.; Manalis, S. R. *Proceedings of the National Academy of Sciences* **2002**, *99*, 14142.

(51) Stagni, C.; Guiducci, C.; Benini, L.; Ricco, B.; Carrara, S.; Paulus, C.; Schienle, M.; Thewes, R. *Sensors Journal, IEEE* **2007**, *7*, 577.

(52) Lee, J.-Y.; Li, J.; Yeung, E. S. *Analytical Chemistry* **2007**, *79*, 8083.

(53) Pleskov, Y. V.; Gurevich, Y. Y. *Semiconductor Photoelectrochemistry*; Consultants Bureau: New York, NY, 1986.

(54) Faulkner, A. J. B. L. R. *Electrochemical Methods: Fundamentals and Applications*; Second Edition ed.; John Wiley & Sons, Inc.: Hoboken, NJ, 2001.

(55) Kang, S. H.; Shortreed, M. R.; Yeung, E. S. *Analytical Chemistry* **2001**, *73*, 1091.

(56) Park, H.-Y.; Li, H.-w.; Yeung, E. S.; Porter, M. D. *Langmuir* **2006**, *22*, 4244.

(57) Mason, M. G.; Hung, L. S.; Tang, C. W.; Lee, S. T.; Wong, K. W.; Wang, M. *Journal of Applied Physics* **1999**, *86*, 1688.

(58) Kim, H.; Horwitz, J. S.; Kushto, G.; Pique, A.; Kafafi, Z. H.; Gilmore, C. M.; Chrisey, D. B. *Journal of Applied Physics* **2000**, *88*, 6021.

(59) Weiher, R. *J. Appl. Phys.* **1966**, *37*, 299.

(60) McCann, J. F.; Bockris, J. O. M. *Journal of The Electrochemical Society* **1981**, *128*, 1719.

(61) van den Meerakker, J. E. A. M.; Meulenkamp, E. A.; Scholten, M. *Journal of Applied Physics* **1993**, *74*, 3282.

CHAPTER 2

QUANTITATIVE DETECTION OF SINGLE MOLECULES IN FLUORESCENCE MICROSCOPY IMAGES*

2.1 Introduction

Single-molecule fluorescence imaging microscopy has become an important technique for probing a variety of chemical phenomena, including imaging molecular diffusion at interfaces and in nanoporous materials,[1-6] biomolecular binding interactions,[7-10] kinetic studies of single enzymes,[11-14] and imaging of biomolecules with sub-diffraction resolution to investigate the structure of cells.[15-21] Single-molecule fluorescence imaging is also being developed as a quantitative analysis tool, where counting fluorescent spots in an image is related to a surface population of bound molecules. This approach has been applied to an *ex situ* analysis where fluorescent molecules are deposited onto a surface by controlled withdrawal of a substrate from solution, followed by imaging of the surface after evaporation of the solvent.[22] This method allows quantitative sampling of molecules on surfaces from low concentration (pM) solutions. Imaging and counting of single molecules on surfaces can also be used to measure adsorption equilibria and kinetics;[9,23,24] when these measurements are made in situ,[9,23] they require exclusion of signal from the solution-phase and are performed with

---

* Reproduced with permission from *Analytical Chemistry*, **2010**, *82*, 189-196.

total internal reflection excitation of the solid-liquid interface. Single-molecule imaging has also been employed to count the density of molecules covalently bound to a surface.[25,26] Fluorescence imaging can also quantify binding from solution of labeled analyte molecules to reaction sites immobilized on a surface, where the fraction of sites with bound molecules can be related to their concentrations in solution.[8,10,27,28] In experiments that measure chemical quantities using fluorescence images, it is critical to understand the systematic uncertainties in the methods used to count single molecules in images. For this reason, there is a need for single molecule imaging methodology that optimizes image analysis for detecting molecular events while excluding the influence of background noise and allowing for explicit determination of experimental uncertainties arising from false-positive and false-negative detection probabilities.

Counting single molecules adsorbed or bound to a surface is generally more reliable than counting them in free or flowing solution[29-31] because molecules remain stationary in the image, which allows signal to be integrated over time to the limit of either photobleaching or the residence time of the molecule on the surface or binding site. A second potential advantage of counting stationary single molecules on a surface is that the imaged fluorescent spot may be subjected to spatial criteria that improve confidence in detection; this is critical when counting single fluorescent labels, where the observed intensities are generally close to background noise levels.

In this paper, we describe a simple approach to incorporating spatial criteria for counting single fluorescent dye molecules by using a local intensity threshold to locate regions with multiple, adjacent intense pixels, where the size of the regions is guided by the point-spread function of the microscope. By requiring multiple, spatially correlated

bright pixels, false-positive events resulting from random samples of background noise are minimized, which allows molecules to be reliably detected and counted at a threshold that is near the background noise level. Setting thresholds closer to the background noise level is required for reliable detection of single-fluorescent labels, where spatial criteria for detection can lower false-positive probabilities by factors of 600 or more, to acceptable levels for quantitative work. The reliability of detection is established by quantitative knowledge of the distributions of background and signals.[32] By measuring and modeling both the background and single-molecule intensity distributions, false-positive and false-negative detection probabilities can be estimated for arbitrary threshold parameters by using simple counting statistics. From this theory, detection parameters can be optimized to minimize false-positive and false-negative probabilities.

In order to develop this analysis, controlled surface densities of rhodamine 6G were deposited onto glass coverslips by substrate withdrawal from varying concentrations of dye in methanol solution, as this method has been shown to generate predictable and quantitative surface fluorophore coverage predicted from the solvent viscosity, density, contact angle and withdrawal rate.[22,33-35] The fluorescence from single molecules was imaged by through-the-objective total internal reflection fluorescence (TIRF)[36] microscopy. Histograms of the photoelectron counts from background regions and from regions of fluorescent spots of single molecules were acquired from images and used to establish the detection threshold and quantify false-negative probabilities, β. False-positive probabilities, α, are quantified by applying the single-molecule detection algorithm to blank images, and compared to modeling of simulated images using a combinatorial statistical analysis.

2.2 Experimental Section

2.2.1 Chemicals and Materials

Spectroscopic grade methanol was purchased from Fisher Scientific (Hampton, NH) and used as received. Concentrated 95% sulfuric acid (EMD Chemicals) and 30% hydrogen peroxide solution ACS grade (EMD Chemicals) were purchased from VWR (West Chester, PA) and used as provided. Water was distilled in a quartz still and then further filtered with a Barnstead NANOpure® II system (Boston, MA) resulting in a resistivity of approximately 18 MΩ·cm. Rhodamine 6G (R6G) 99% purity (Acros Organics) was purchased from Fisher Scientific (Hampton, NH) and used as received. Glass 22 x 22 mm no. 1 coverslips were purchased from VWR (West Chester, PA).

2.2.2 Deposition of Dye Molecules onto Glass

Glass coverslips were prepared with known densities of rhodamine 6G molecules by withdrawing them from standard solution at a controlled velocity.[22,35] Prior to dye deposition, glass coverslips were cleaned by rinsing in 18 MΩ·cm water for 15 min, followed by 15 min of exposure to piranha solution (3:2 mixture of concentrated sulfuric acid and 30% hydrogen peroxide). After piranha cleaning, the coverslips were rinsed in 18 MΩ·cm water and methanol twice each for 10 min, allowed to dry, and then cleaned in a UV ozone cleaner (Jelight Co. model 342) for 25 min per side. A blank methanol sample plus R6G solutions in methanol were prepared at concentrations of 20, 40, 79, 155, and 283 pM for deposition. During deposition, the glass coverslip is held stationary in clamp above a moving platform that supports a beaker containing the blank or R6G solution. The platform is attached to a Velmex UniSlide platform mounted vertically on an angle bracket and driven by a Pittman stepper motor. The platform is first raised until

the solution covers the coverslip substrate, and then the platform is immediately lowered until the surface of the solution drops below the bottom edge of the substrate, leaving a thin solution film on its surface. The thin film deposited on the slide is allowed to evaporate, and one side of the coverslip is wiped with methanol-wetted lens tissue to remove any deposited dye from the surface that will be in contact with immersion oil of the microscope objective.

2.2.3 Fluorescence Microscopy

R6G coated glass coverslips were imaged using an Olympus iX71 inverted microscope with through-the-objective total internal reflection fluorescence (TIRF) illumination. Laser radiation at 514 nm from a Coherent® Innova® 300 argon ion laser is coupled into a single mode polarization maintaining optical fiber (Thorlabs) using a fiber collimating lens (Thorlabs). Light emitted from the opposite end of the fiber is collimated by a plano-convex achromatic lens, and passed through a quarter wave plate (Newport). The 1.2 mW collimated laser beam is then focused onto the back focal plane of a 60x 1.45 N.A. oil immersion objective lens. Total internal reflection is achieved by translating the fiber position horizontally until the laser beam is focused near the edge of the objective's back aperture. Fluorescence emission from the coverslip-air interface is collected by the same objective, passed through a filter cube with a dichroic beam splitter (Chroma Z514RDC), an emission band pass filter (Chroma HQ560/50m), and then through additional 1.6x magnification optics.

It has been shown previously that linearly polarized illumination can lead to significant variations in single-molecule emission intensity[7,37] because random excitation dipole orientations experience varying excitation electric field strengths. For this reason,

a quarter-wave plate was used to generate elliptically polarized excitation light with an s-polarized to p-polarized light ratio of 2.5:1, in order to provide a more isotropic light intensity at the interface. This polarization ratio generates approximately equal light intensities both normal to the interface and in the plane of the interface, normal to the reflection axis, in the evanescent wave.[38] The laser excitation intensity was minimized in order to prevent photobleaching of the dye molecules. The total laser intensity coupled into the objective lens was 1.2 mW, corresponding to a power density of approximately 16 Wcm^{-2}.

Images were collected with an electron multiplying charge coupled device (EMCCD) camera (Andor™ $iXon^{EM}$+ 897) using a 300 x 300 pixel region on the sensor (50 × 50 μm in the sample). Images were taken by collecting continuous videos at approximately four frames per second (275 ms integration time at an EM gain of 54) while translating the microscope stage in x-y manually from region to region on the coverslip. Images from unique regions were then cut out of the video and analyzed.

2.2.4 Data Analysis

Image processing and analysis were carried out using custom programs written in the Matlab® (Mathworks™) software environment. Analysis was largely performed on a PC with an Intel® 3 GHz Core™ 2 Duo processor and 8 GB of RAM running a 64 bit operating system. Single R6G molecules were located in each image using an automated routine which records the location and pixel intensity of each spot for analysis. The details of the algorithm are described below.

2.3 Results and Discussion

2.3.1 Quantitative Imaging of Rhodamine 6G on Glass

R6G molecules deposited on glass slides by substrate-withdrawal from standard solutions[22,35] were imaged using an inverted microscope with through-the-objective TIRF illumination at 514 nm from an argon ion laser. An example image is shown in Figure 2.1. Low laser excitation intensity, approximately 16 Wcm^{-2}, was used in order to minimize photobleaching of the fluorophore. The photobleaching rate was determined by observing R6G molecules bleach on the glass surface upon continuous exposure to laser radiation. A plot of the number of surviving molecules on the surface versus time has been fit to a biexponential decay function in order to determine the photobleaching rates; see Appendix A.2. The photobleaching rates are 0.22 s^{-1} and 0.014 s^{-1}, with relative pre-exponential factors of 0.71 and 0.29, respectively. To reduce the intensity variation due to photobleaching, the fraction of R6G lost to photobleaching was kept below 10% by collecting images within 0.8 seconds of illuminating a new region.

Images of single molecules were collected using an Andor iXon EMCCD camera using a low electron multiplying gain setting of 54, out of a maximum of 1000. The pixel intensity values in all images were converted from analog-to-digital unit (ADU) counts to actual photoelectron counts using calibration images of flat white-light background noise.[39] The ADU count variance in white light images measured with varying integration times was plotted against the corresponding ADU count mean, and fit to a linear function. The white light intensity-variance curve fit a straight line (see Appendix A.1), indicating Poisson behavior in the measured background intensities. The x-intercept

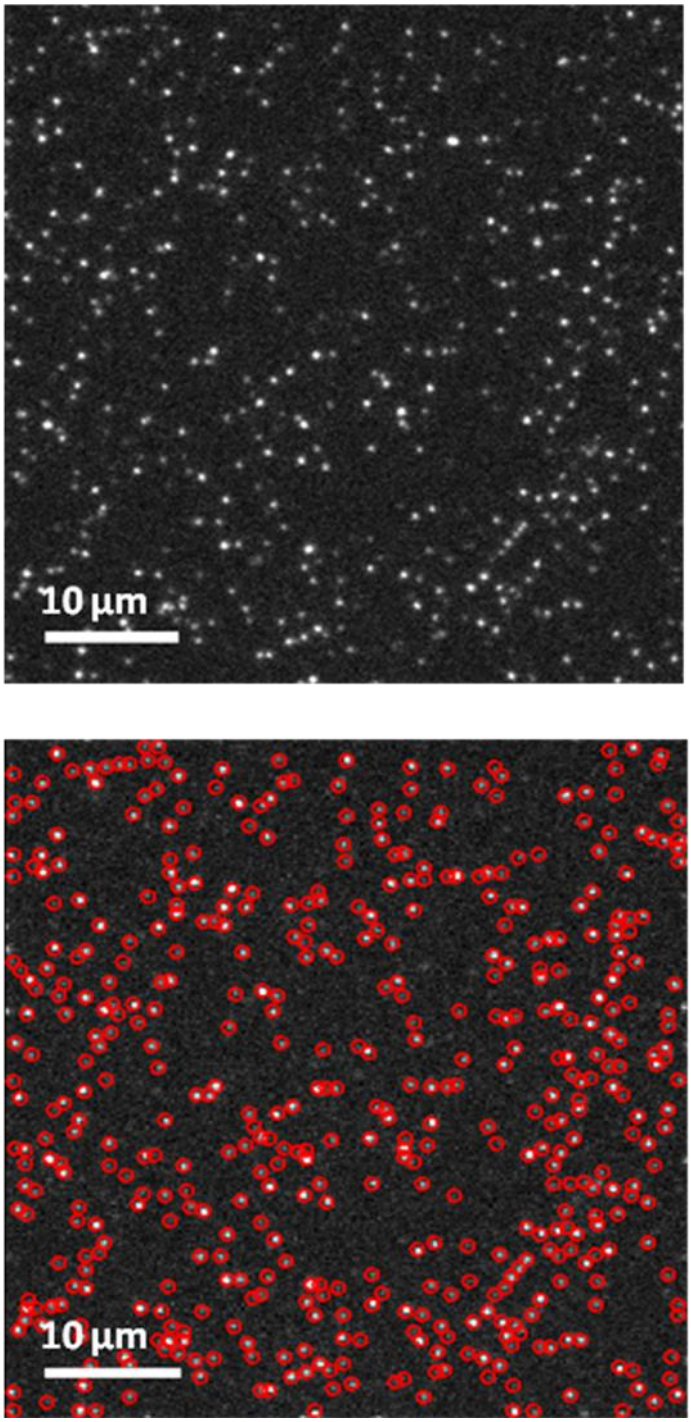

Figure 2.1. Image of R6G dip-coated onto a glass coverslip from 79 pM R6G solution in methanol. Images show before (above) and after (below) detecting all spots that meet the adjacent-pixel criterion. Image size is 50x50 µm.

of this fitted line is used correct for the detector offset, and the slope is used to convert between ADU counts and photoelectrons.[39]

Single-molecule spots in images were located using a detection algorithm that takes into account the size of the point-spread function of the microscope, which causes the images of single-molecule fluorescence spots to be distributed over several adjacent pixels on the CCD camera. This information can be used to exclude random noise from the detector by requiring that the intensity of detected molecular spots be spatially correlated, where several adjacent pixels are above a threshold. The choice of the number of adjacent bright pixels in the detection algorithm is based on the measured intensity distribution of single R6G molecules. This point-spread function (PSF) was determined by fitting a two-dimensional symmetrical Gaussian function to each of approximately 1,500 bright spots in an image; see example in Figure 2.2. From the average parameters extracted from these fits, the point-spread function was well modeled by a Gaussian spatial distribution with a radius (standard deviation) of 1.0 ± 0.2 pixels (16 μm on the camera, 170 nm in the sample). The radius of this distribution predicts that at 1 pixel away from center, the intensity will be 60% of the maximum signal at the center; while at 2 pixels away from the center, the intensity will be down to 13%. Pixels with only 13% of the brightness of the peak pixels are likely to be indistinguishable from noise, and so resulting in a detection volume of 3 × 3 pixels or 9 pixel^2 (500 × 500 nm in the sample). The distribution of individual pixel intensities in this detection volume can vary significantly due to variations in the position of the point-spread function in relation to the pixel locations. The smallest number of illuminated pixels is observed when the single-molecule intensity distribution is centered on the corner of four adjacent pixels,

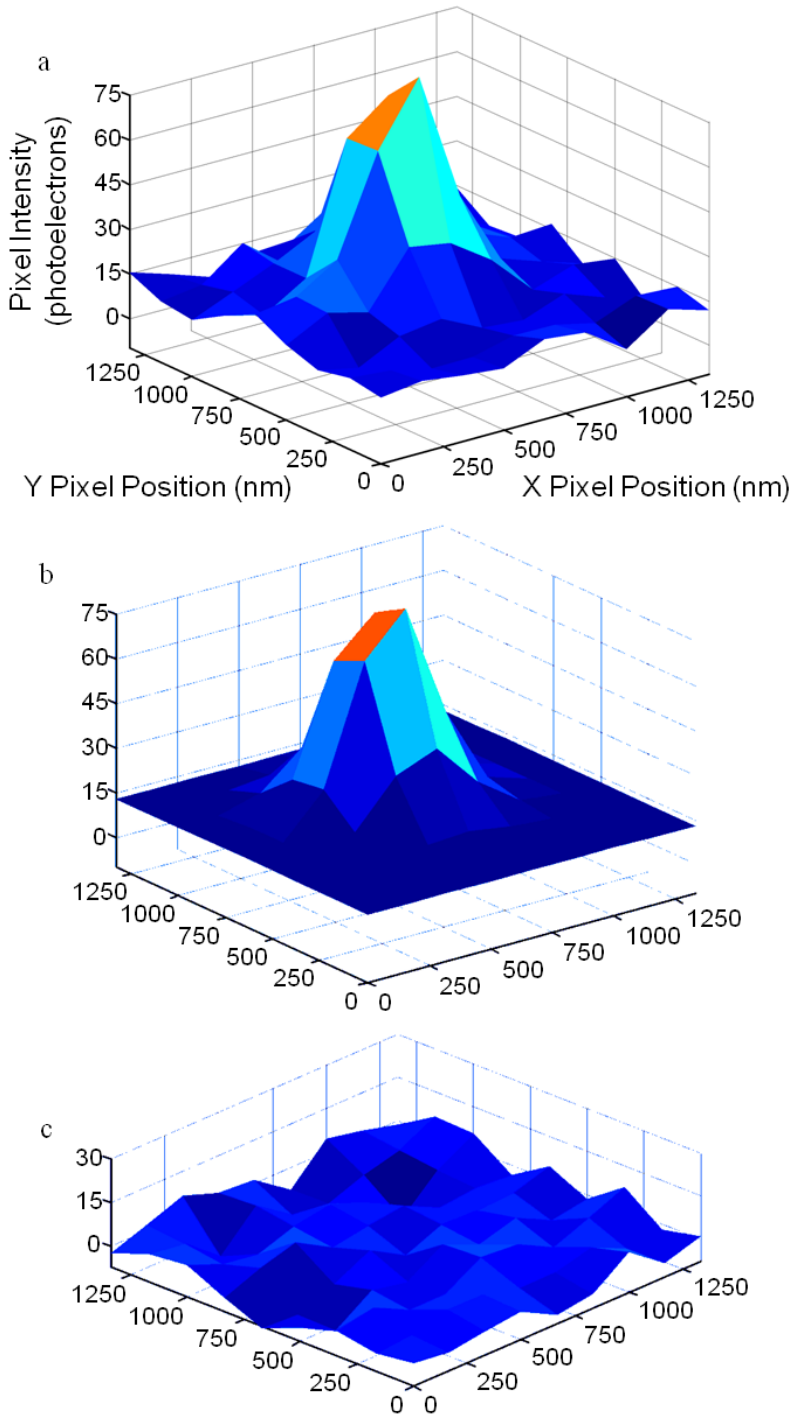

Figure 2.2. Example single-molecule fluorescence point-spread function sampled by the CCD camera in the reference frame of the sample; a) raw intensity data; b) fitted symmetrical 2-D Gaussian function, c) residuals of the fit.

only pixels adjacent to the center of the PSF, estimated as the brightest pixel in the measured PSF, will be detectable. There are 8 pixels adjacent to any maximum pixel, where those four pixels would accumulate most of the intensity. Moving the center of the distribution off of this corner increases the number of illuminated pixels that receive up to 60% of the maximum (see above). To assure that molecules are detected even when their intensity falls on a corner, we conservatively set the detection criterion such that two adjacent pixels, $p_{crit} = 2$, next to any bright pixel must also be above threshold. Note that adjacent bright pixels can share a corner or edge, and the criterion could be set higher than 2 if the point-spread function were larger relative to the pixel dimensions.

The algorithm for identifying spatially correlated bright pixels first requires a threshold for detecting significant signal intensity above background. This intensity threshold, I_{thold}, is defined as some multiple, n_{thold}, of the standard deviation of the background, σ_{BG}, above the mean background, $\mu_{BG:}$

$$I_{thold} = \mu_{BG} + n_{thold}\sigma_{BG} \qquad [2.1]$$

For each set of images, μ_{BG} and σ_{BG} were determined by fitting a Gaussian distribution to a histogram of photoelectron counts. The distribution of photoelectron counts in blank images follows a Poisson shot noise model, where the mean background value, 13.6 counts, is equivalent to the background variance, 13.3 counts. In order to accurately determine the Poisson mean, μ_{BG}, the histogram of blank intensities was fit to a Poisson distribution using least-squares methods. The blank intensity histogram and fitted Poisson distribution, with $\mu_{BG} = 13.0$ photoelectrons as the only fitted parameter, are plotted in Figure 2.3.

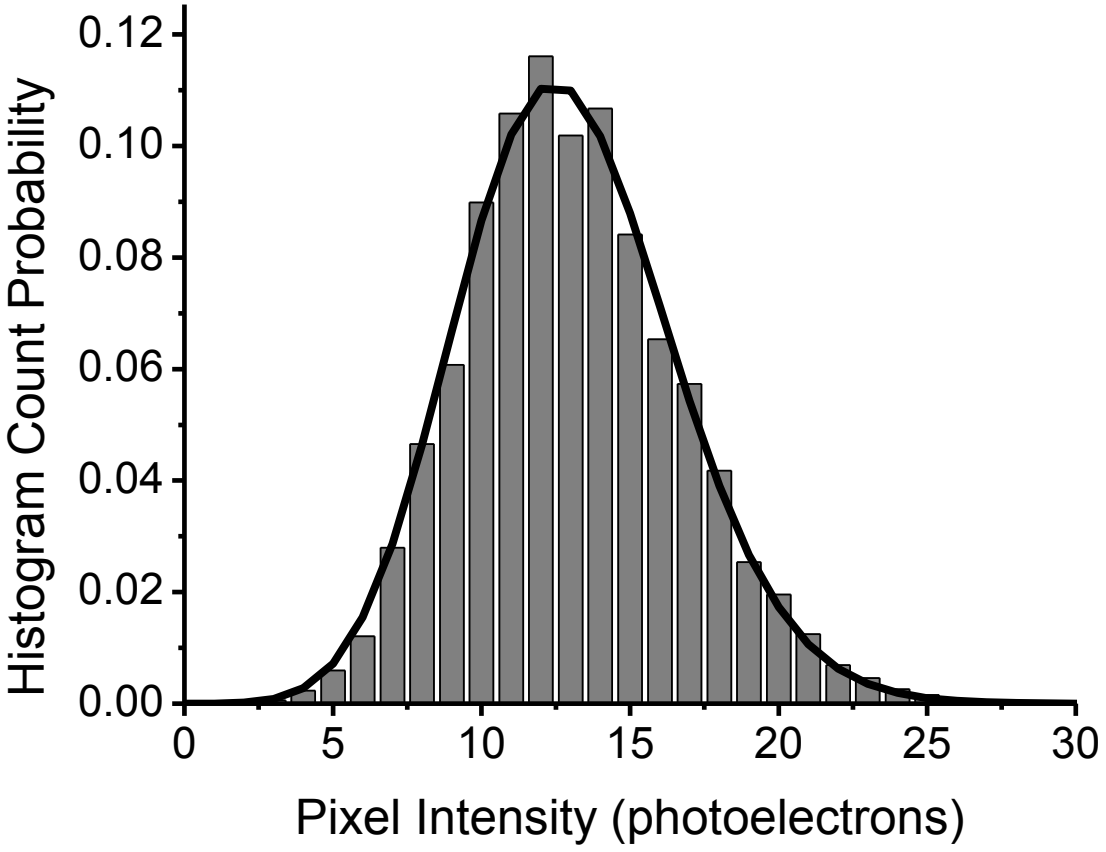

Figure 2.3. Histogram of integral-normalized blank image in photoelectron counts, fit to a Poisson distribution with μ_{BG} = 13.0 photoelectrons.

When R6G molecules are present in an image, the upper tail of the background intensity distribution is perturbed by the presence of bright single-molecule spots, making it impossible to fit a Poisson distribution. In order to circumvent this problem, the mean background in R6G images is estimated from a Gaussian fit and the standard deviation is estimated as: $\sigma_{BG} = \mu_{BG}^{1/2}$. A fit of the background intensity to a symmetrical Gaussian distribution slightly overestimates the Poisson mean because it does not capture the Poisson tail at high intensities; nevertheless, the error is less than 5% for a mean of 13 photoelectrons, and the error becomes smaller as the mean increases.[40,41] The 20, 40 and 79 pM R6G samples were found to have very similar μ_{BG} and σ_{BG} values, and so a single I_{thold} was chosen to simplify the false-positive probability calculation (see below). The background distribution parameters, μ_{BG}, σ_{BG}, and I_{thold}, are summarized in Table 2.1. Having established an intensity threshold, I_{thold}, for identifying adjacent bright pixels for detection of single molecules, the algorithm finds the brightest pixel in an image and then tests the eight adjacent pixels around that bright pixel to determine the number, q, that exceed I_{thold}. When $q \geq p_{crit} = 2$, then the bright spot is counted as a single molecule. Before locating the next highest bright spot in the image, the previous spot must be prevented from being double counted; therefore, a small region, typically 7 × 7 pixels (1.17 × 1.17 μm), around the spot is deleted from the search for brightest pixels. The algorithm then steps to the next brightest pixel in the image and the process repeats. An example image of R6G molecules deposited on glass out of a 79 pM R6G methanol solution is shown in Figure 2.1, along with the identified spots from the search algorithm. Measured R6G surface densities deposited on substrates from solutions with varying R6G concentration are shown in Figure 2.4.

Table 2.1

Experimental Results for Quantitative Single Molecule Detection

R6G Solution Concentration	Experimental Spot Density,[1] D_{meas} ($1/cm^2$)	Spot density uncertainty[2] ($1/cm^2$)	Theoretical Spot Density,[3] D_{meas}, ($1/cm^2$)	Mean Background,[4] μ_{BG} (photoelectrons)	Background Std. Dev.,[5] σ_{BG} (photoelectrons)	Intensity Threshold, I_{thold} (photoelectrons)	False Negative Detection Probability, β (%)	Theoretical False Positive Probability, α_{theor} (per image)	Measured false Positive Probability, α_{exp} (per image)
Blank	3.6×10^5	6×10^4	0.0	13.0	3.6	22	-	1.9	2.8
20 pM	4.1×10^6	3×10^5	5.9×10^6	12.1	3.5	22	4.4[6]	1.9	-
40 pM	7.7×10^6	4×10^5	1.2×10^7	12.4	3.5	22	4.4[6]	1.9	-
79 pM	2.1×10^7	1×10^6	2.2×10^7	12.7	3.6	22	4.4[6]	1.9	-
155 pM	4.5×10^7	2×10^6	4.2×10^7	13.9	3.7	23	1.3	1.9	-
283 pM	7.6×10^7	4×10^6	7.1×10^7	17.0	4.1	27	1.7	1.9	-

[1] Blank densities have been subtracted from total densities for 20 to 283 pM R6G

[2] Uncertainty is 2 standard deviations of the mean

[3] D_{meas} predicted by Equation 4.

[4] Determined by a Poisson distribution fit for the blank data, a Gaussian distribution for R6G samples (see text).

[5] Calculated from mean: $\sigma_{BG} = \mu_{BG}^{1/2}$

[6] Histograms were summed for 20, 40, and 79 pM data

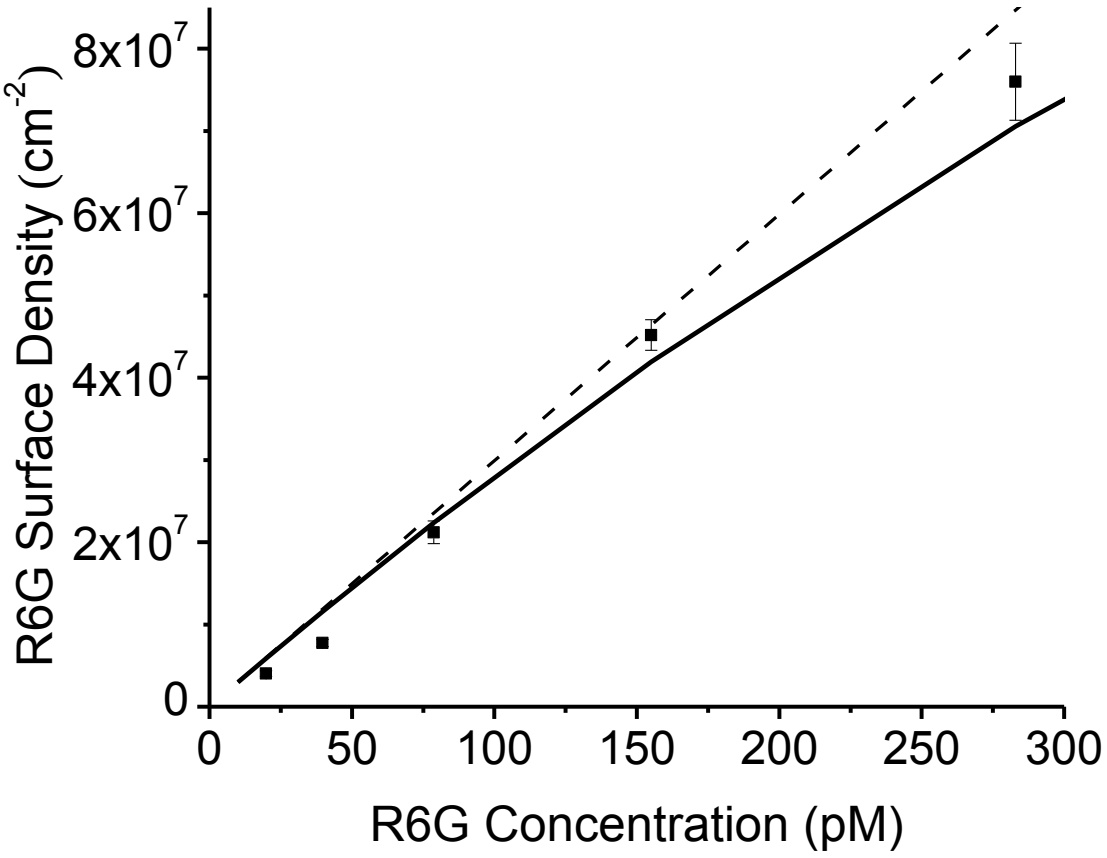

Figure 2.4. Measured dip coated R6G density (black squares) are plotted with expected molecular coverage, Γ(dashed line) and the expected detectable spot density, D_{meas} (full line) from equation 2.4; error bars represent 2 standard deviations of the mean.

2.3.2 Verifying the Detected Molecular Density with Standards

In order to verify the accuracy of the measured surface densities reported by the single-molecule detection algorithm, standard samples having known, optically-resolvable fluorophore densities are required. Samples that meet these criteria were generated by dosing glass substrates with rhodamine 6G by substrate-withdrawal from standard solutions.[22,34,35] This technique is based on theory by Landau and Levich,[42] which predicts the thickness of a liquid layer, t, that adheres to a solid surface above the liquid meniscus, as the substrate is withdrawn from the liquid at a velocity, *U*:

$$t = \frac{0.994(\eta U)^{2/3}}{(\rho g)^{1/2}\gamma^{1/6}} \qquad [2.2]$$

This thickness was evaluated for methanol as a solvent, where the density, ρ = 791.4 kg/m^3, the viscosity, $\eta = 5.97 \times 10^{-4}$ kg/m·s, the surface tension, $\gamma = 2.61 \times 10^{-3}$ N/m, and gravitational acceleration, g = 9.81 m/s^2. At a withdrawal rate, U = 0.60 cm/s, the predicted film thickness is t = 5.0 μm. If the solution contains a known concentration of fluorophores, C, the resulting density of molecules, Γ, that remain on the surface after solvent evaporation is the solution concentration times the film thickness,[22,35]

$$\Gamma = Ct \qquad [2.3]$$

If the fluorophore being deposited has strong interactions with the solid surface, the observed surface density could be higher than that predicted due to adsorption from solution prior to withdrawal. Adsorption of rhodamine 6G to silica surfaces has been tested by measuring its elution by methanol from a silica gel column using HPLC.[22,35] The adsorption equilibrium constant of rhodamine 6G was determined from the measured

capacity factor, k', mobile-phase volume and mass of silica gel in the column, and the specific surface area of the silica gel. The adsorption equilibrium constant of the dye onto silica from methanol was found to be small, $K_{ads} = \Gamma_{ads} / C = 2.5 \times 10^{-6}$ cm = 0.025 μm.[22]

This equilibrium constant is the ratio of the density of dye on the surface to the concentration of dye in solution and is the equivalent solution depth that contains the same number of molecules per unit area as are adsorbed to the surface at equilibrium. This solution depth can be compared directly to the adherent solution film following withdrawal from solution, to determine whether adsorption or deposition governs the number of molecules per unit area on the surface.[22] Compared to the thickness of the liquid film that adheres to the substrate upon withdrawal from solution, t = 5.0 μm, the adsorption equilibrium constant corresponds to an equivalent solution depth that is a small fraction (0.5%) of the deposited solution film thickness (at the withdrawal velocity, U = 0.60 cm/s). Therefore, adsorption of R6G prior to substrate withdrawal from solution will account for an insignificant number of molecules on the surface compared to those deposited by evaporation of the adherent solution film. From the R6G concentrations used in depositing dye for this work, 20 to 280 pM, the predicted surface densities range from $\Gamma = 6.0 \times 10^{6}$ to 8.5×10^{7} cm^{-2}, and are plotted in Figure 2.4.

As Figure 2.4 shows, the predicted R6G surface deposition density, Γ, agrees with measured results at low concentrations, but is higher than the measured surface density at higher concentrations. The lower measured densities are due to the algorithm being unable to resolve multiple molecules within the 7 x 7 pixel area corresponding to a detected spot and deleted from further searching. This area represents the resolution limit for locating and counting single molecules. At higher surface densities, the distances

between molecules approach this resolution limit, and the number of spots counted will be less than the actual number of deposited molecules, as individual single-molecule spots fail to be resolved. Because the countable numbers of molecules on the surface are drawn with low probability from a much larger population in solution and dispersed randomly over the surface, the occupation of resolvable areas on the surface and the likelihood of multiple occupation molecular overlap should follow Poisson statistics.[40]

Poisson statistics have been used to account for peak overlap developed for chromatographic separations,[43] saturation of single-molecule counting in capillary electrophoresis,[29] and more recently to estimate the peak capacity single-molecule images.[22] This Poisson model predicts the measured density of spots in an image from the maximum density of resolvable spots, D_{max}, times one minus the probability of no molecules being detected:

$$D_{meas} = D_{max}[1 - e^{-\frac{\Gamma}{D_{max}}}] \qquad [2.4]$$

where D_{meas} is the measured spot density, Γ is the actual molecular coverage, and D_{max} is the density of spots that can be resolved. D_{max} can be calculated explicitly for the detection algorithm above using the size of the region that is deleted from the search for brightest pixels after every detected spot is found. A 7 × 7 pixel region is deleted around each detected spot, meaning that the closest bright spot can be 4 pixels away. Starting in the corner of the image and arranging spots 4 pixels apart in x and y, a 300 × 300 pixel image can be occupied by $300^2 / 4^2 = 5625$ spots, corresponding to $D_{max} = 2.25 \times 10^8$ spots/cm^2. Using this value of D_{max}, the measured density of spots D_{meas} can be predicted from equation 2.4 with the molecular density predicted by equation 2.3. In Figure 2.4,

the a priori predictions of equation 2.4, *which are not fitted to the measured surface densities*, are plotted together with the measured results, which agree within the uncertainty of the measurements.

2.3.3 Determining the False-Negative Probability

The false-negative detection probability, β,[32] is the fraction of single-molecule spots that do not exceed the intensity threshold, I_{thold}. Because the algorithm used to identify single-molecule spots requires that three adjacent pixels be brighter than I_{thold}, successful detection depends entirely on the intensity of the third-most-intense pixel within the point-spread function. For convenience, this critical, third-most-intense pixel will be called "pixel-3." We can determine β by fitting a histogram of pixel-3 intensities from each located single-molecule spot to a distribution in order to determine what fraction of the pixel-3 distribution lies below I_{thold}.

A histogram of pixel-3 intensities from images of samples deposited from 155-pM R6G solution is shown in Figure 2.5; these data are fit to an empirical, asymmetric double-sigmoid function,[44] which follows the observed histogram shape over its entire range. The asymmetry of the single-molecule intensity distribution is due in part to the random orientation of molecules on the surface which affects the excitation and collection efficiency;[45]additional intensity variation arises from the sampling of the point-spread function by the 3rd pixel, which depends sensitively on position of the spot relative to the pixel array. The fitted distribution in Figure 2.5 is integrated numerically to determine the total area and the area that is below the threshold, I_{thold}. The ratio of the area below threshold to the total area defines β, which was found to be 1.2%. The 155 pM and 283 pM images contained sufficient molecule spots (greater than 70,000) to

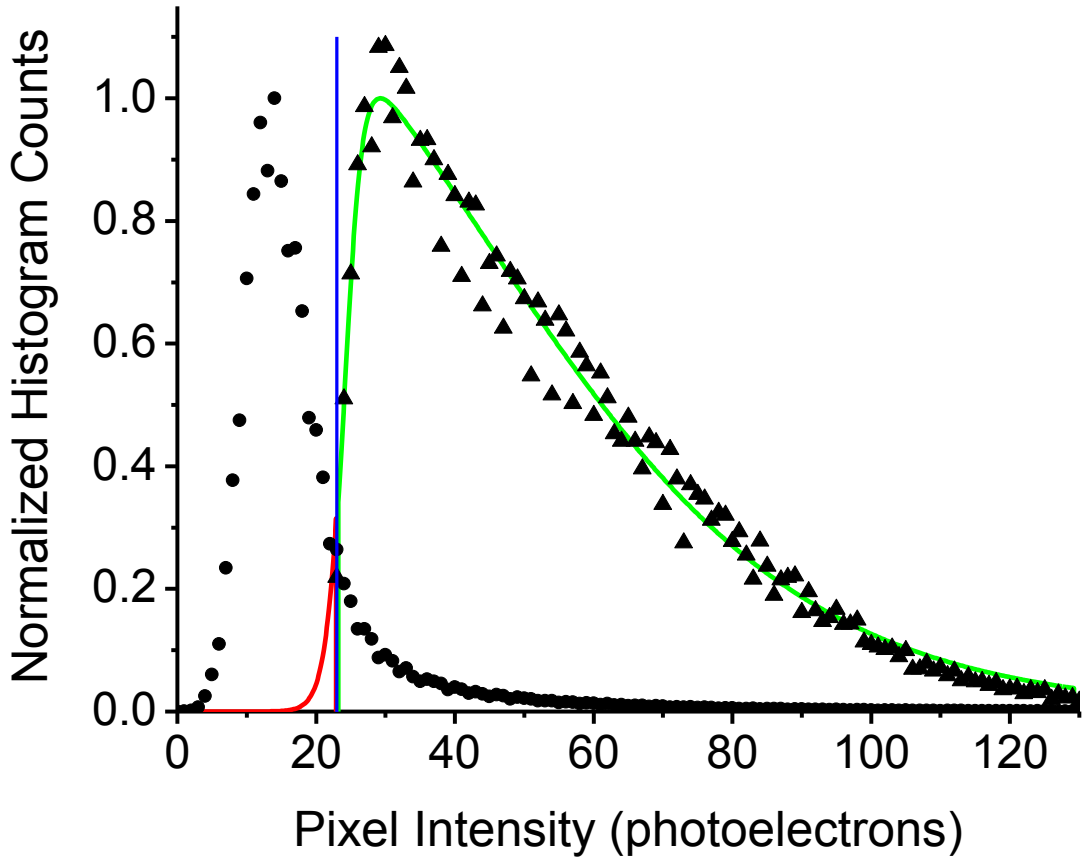

Figure 2.5. Histogram of pixel intensities for all pixels in the image (black circles) and the third most intense pixel in the single molecule spot (black triangles). The red and green regions represent the area of a double asymmetric sigmoid function fit to the molecule histogram below (red region) and above (green region) the intensity threshold (blue line).

generate clean histograms and β statistics. For the 20, 40 and 79 pM images it was necessary to sum their pixel-3 histograms to collect sufficient observations to determine β. Because the mean backgrounds and standard deviations were very close for these lower-density samples, the same I_{thold} was used for the 20, 40, and 79 pM images which also allowed the histogram areas from these data to be combined. The average β for all data sets (see Table 2.1) was found to be 2.5%, indicating that 97.5 % of all R6G molecules are detected, which is consistent with the measured molecular densities agreeing with the substrate-withdrawal standards, described in the previous section. The slightly higher false-positive probability in the lower concentration samples, 4.4%, is an artifact of false-positive events, which comprise a greater fraction of the detected spots in lower density images. False negative probabilities determined for n_{thold} values between 1.5 and 3.5 have been calculated by numerical integration of the empirical function fit to the 155 pM pixel-3 distribution, and are plotted in Figure 2.6a.

2.3.4 Determining the False-Positive Probability

A major advantage of this multipixel single-molecule detection scheme is that false-positive detection probabilities can be calculated explicitly, using combinatorial statistical analysis,[46] from the detection algorithm parameters and the background intensity distribution. These mathematical techniques are analogous to calculating statistical thermodynamics partition functions. Theoretical false-positive probabilities, $\alpha_{(theor)}$ are defined by the number ways to arrange intense pixels derived from noise that trigger a false positive, N_{detect}, divided by the total number of ways intense noise pixels can be arranged, N_{total}:

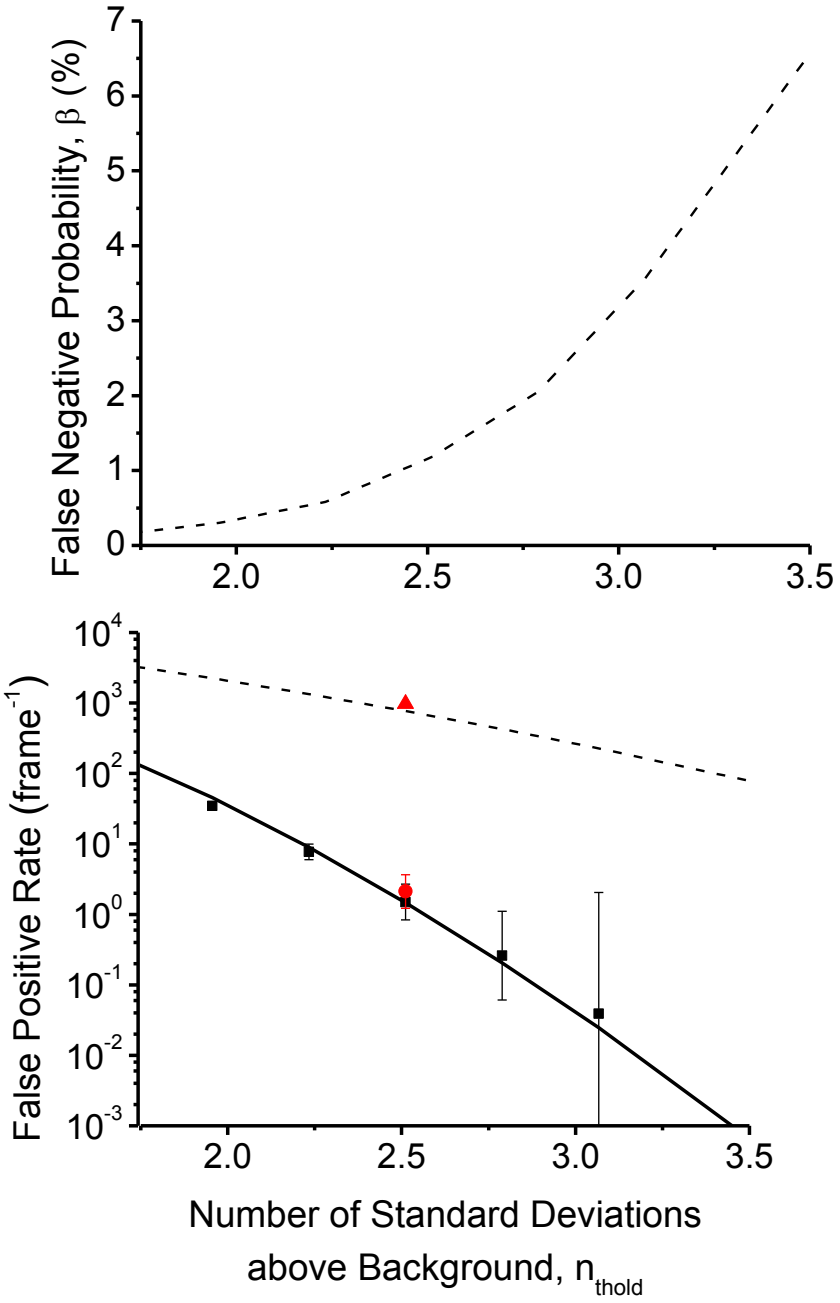

Figure 2.6. False negative and false positive probabilities for molecule detection, a) The false negative probability, β, for the 155 pM concentration is plotted against the detection intensity threshold, n_{thold}. b) The false positive rate per 300 x 300 image for detection with three-pixel spatial correlation is plotted (log scale) against the detection intensity threshold, n_{thold}, for simulated results run on images of Poisson distributed random noise with $\mu = 13.0$ (black squares) and theoretical results from equation 2.7 (black line). The false positive rate for detection using no pixel is also shown (black dashed line). The experimentally determined false positive rates with spatial correlation (red circle) and without spatial correlation (red triangle) are also plotted.

$$N_{total} = \frac{p_{total}!}{p_{total}!(p_{total}-p_{thold})!} \quad [2.5]$$

N_{total} is calculated from the number of pixels in an image, p_{total}, and the number of noise pixels, p_{thold}, brighter than the intensity threshold, I_{thold}. For background noise comprised of photoelectron shot noise, p_{thold} is calculated by multiplying p_{total} by the integral of the background Poisson distribution that is above the intensity threshold for ways the remaining p_{thold} - p_{crit} pixels can be arranged in the entire image. This expression must then be summed over an index q from p_{crit} to p_{adj}. Finally, this value is multiplied by the total number of pixels above threshold, p_{thold}, to generate an expression for N_{detect}:

$$N_{detect} = \sum_{q=p_{crit}}^{q=p_{adj}} \frac{p_{thold}p_{adj}!(p_{total}-p_{adj})!}{q!(p_{adj}-q)!(p_{thold}-q)!(p_{total}-p_{adj}-p_{thold}+q)!} \quad [2.6]$$

Dividing N_{detect} by N_{total} yields the final expression for the theoretical false-positive probability per video frame, α_{theor}:

$$\alpha_{theor} = \frac{p_{thold}p_{adj}!p_{thold}!(p_{total}-p_{adj})!(p_{total}-p_{thold})!}{p_{total}!} \sum_{q=p_{crit}}^{q=p_{adj}} \frac{1}{q!(p_{adj}-q)!(p_{thold}-q)!(p_{total}-p_{adj}-p_{thold}+q)!} \quad [2.7]$$

The function was evaluated for only $q = p_{crit} = 2$, as the probability contribution from larger q is quite small in this case, although it could be greater for spot images that are magnified over a greater number of pixels. The resulting truncated α_{theor} was evaluated, using Stirling's approximation carried to four terms, with the experimental detection parameters used in the blank images (μ_{BG}, σ_{BG}). The accuracy of this

expression was tested by locating false-positive spots in simulated images of random, Poisson-like noise modeled after blank images with $\mu_{BG} = 13.0$ photoelectrons. The simulated false-positive probability, α_{sim}, and the theoretical false-positive probability, α_{theor}, were found to agree within the simulation uncertainty, as shown in Figure 2.6. At a threshold of 2.5 standard deviations above the background, $n_{thold} = 2.5$, α_{theor} predicted 1.9 events per 300 × 300 pixel image, while α_{sim} averaged 2.0 ± 1.4 false positives.

The false-positive probabilities in actual experimental images were determined from blank images of slides that were dip coated by withdrawal from pure methanol containing no R6G. Short 6 to 15 frame videos of 6 stationary regions on blank slides were collected and bright spots were located in each video frame. False-positive probabilities resulting from random noise were determined by counting spots located in only one video frame. Any spots found with the same coordinates in multiple frames were likely the result of actual fluorescent defects in the glass or contamination on the surface and were excluded from the false-positive probability determination. The total blank spot count was 9 ± 3 per image, while the false-positive probability resulting from background noise alone (non-spatially correlated detected spots) was found to be $\alpha = 2.8 \pm 1.6$ false positives per image. The experimentally measured $\alpha = 2.8 \pm 1.6$ FP per image, and theoretical $\alpha_{theor} = 1.9$ FP per image as shown on Figure 2.6b, agree remarkably well, further indicating that the background intensity is well modeled by a Poisson distribution. Similar calculations and simulations based on a Gaussian background pixel distribution greatly underestimate the false-positive probability, predicting $\alpha = 0.17$ per image.

False positive rates are significantly reduced by detecting three spatially-correlated intense pixels rather than a single, intense pixel. The false positive rate, for a detection scheme using no spatial correlation criteria where only a single intense pixel is detected, was determined by numerically integrating the background pixel Poisson distribution at varying values of n_{thold}, and the results are also plotted in Figure 2.6b. At $n_{thold} = 2.5$ used in our experiments, the single-pixel false positive rate agrees with the prediction and is ~600-times greater (over 1,500 events per frame) than when spatial criteria are added to the detection scheme. Detecting true single molecule events in images with low signal-to-noise ratios typical of a single-fluor response would be impossible without adding spatial criteria to the detection scheme. Finally, a comparison of the false-negative and false-positive results in Figure 2.6 clearly illustrate the trade-offs that exist in setting a threshold for single-molecule detection. Lowering the threshold can decrease the probability of missing molecules that should be counted; however lowering the threshold also dramatically raises the numbers of false events that are included in the count. The appropriate trade-off depends on the average molecular density in an image, where greater numbers of true fluors in an image will lower the relative error caused by a higher number of false-positive events allowing a lower threshold. The upper bound to an acceptable molecular density depends on the spot-capacity of the image, D_{max}, limited by the optical resolution of the microscope.

2.4 Summary

The goal of this research was to develop and demonstrate methodology capable of quantitatively detecting single dye labels in fluorescence images. Quantitative, optically-resolvable densities of rhodamine 6G fluorophores were deposited onto glass surfaces

and imaged using total internal reflection fluorescence microscopy. Using a multiple-pixel intensity threshold detection algorithm, individual rhodamine 6G dye molecules were located and counted in images of the dye deposited onto glass at varying surface densities. Measured R6G spot densities were shown to correspond to expected molecular coverages, validating the detection algorithm. Theory has been developed to evaluate false-negative and false-positive detection probabilities using simple parameters, such as the background and the single molecule pixel photoelectron distribution, which can be evaluated for any single molecule imaging experiment. False-negative probabilities were evaluated from histograms of located single molecules, and average from higher concentration samples to be 1.5%. False-positive detection probabilities, as measured in blank images and evaluated using theoretical and simulation techniques, were greatly reduced by incorporation of spatial criteria in the analysis, from over 1,500 events per frame to approximately two to three events per image.

Samples in this experiment were imaged using relatively low laser intensities, with resulting low signal to noise levels, in order to minimize photobleaching, which is critical to measuring the kinetics of molecules carrying a single fluorescent label in order to minimize the influence of photobleaching on the observed kinetics. Despite low signal-to-noise ratios, single dye labels can be reliably detected with reasonable uncertainties. Reliable single-molecule detection is relevant to applications where the results will be subjected to quantitative interpretation (counting molecule populations, measuring residence times). The techniques described in the present work can help to design, optimize, and evaluate the uncertainty in quantitative applications of single-molecule imaging measurements.

2.5 Acknowledgments

This research was supported by the U.S. Department of Energy under grant DE-FG03-93ER14333. Additional support from the National Science Foundation for the construction of the TIRF microscope under grant CHE-0654229, is gratefully acknowledged.

2.6 References

(1) Schmidt, T.; Schütz, G. J.; Baumgartner, W.; Gruber, H. J.; Schindler, H. *Proceedings of the National Academy of Sciences of the United States of America* **1996**, *93*, 2926.

(2) Ludes, M. D.; Wirth, M. J. *Analytical Chemistry* **2002**, *74*, 386.

(3) McCain, K. S.; Hanley, D. C.; Harris, J. M. *Analytical Chemistry* **2003**, *75*, 4351.

(4) He, Y.; Li, H.-W.; Yeung, E. S. *Journal of Physical Chemistry B* **2005**, *109*, 8820.

(5) Higgins, D. A.; Collinson, M. M. *Langmuir* **2005**, *21*, 9023.

(6) Lu Li, X. T., Guizheng Zou, Zhikun Shi, Xiaoli Zhang, Wenrui Jin *Analytical Chemistry* **2008**, *80*, 3999.

(7) Tokimoto, T.; Bethea, T. R. C.; Zhou, M.; Ghosh, I.; Wirth, M. J. *Applied Spectroscopy* **2007**, *61*, 130.

(8) Elenko, M. P.; Szostak, J. W.; van Oijen, A. M. *Journal of the American Chemical Society* **2009**.

(9) Fox, C. B.; Wayment, J. R.; Myers, G. A.; Endicott, S. K.; Harris, J. M. *Analytical Chemistry* **2009**, *81*, 5130.

(10) Wayment, J. R.; Harris, J. M. *Analytical Chemistry* **2009**, *81*, 336.

(11) Funatsu, T.; Harada, Y.; Tokunaga, M.; Saito, K.; Yanagida, T. *Nature* **1995**, *374*, 555.

(12) Tokunaga, M.; Kitamura, K.; Saito, K.; Iwane, A. H.; Yanagida, T. *Biochemical and Biophysical Research Communications* **1997**, *9*, 47.

(13) Roeffaers, M. B. J.; De Cremer, G.; Uji-i, H.; Muls, B. o.; Sels, B. F.; Jacobs, P. A.; De Schryver, F. C.; De Vos, D. E.; Hofkens, J. *Proceedings of the National Academy of Sciences* **2007**, *104*, 12603.

(14) Min, W.; English, B. P.; Luo, G.; Cherayil, B. J.; Kou, S. C.; Xie, X. S. *Accounts of Chemical Research* **2005**, *38*, 923.

(15) Carrington, W. A.; Lynch, R. M.; Moore, E. D. W.; Isenberg, G.; Fogarty, K. E.; Fay, F. S. *Science* **1995**, *268*, 1483.

(16) Thompson, R. E.; Larson, D. R.; Webb, W. W. *Biophysical Journal* **2002**, *82*, 2775.

(17) Yildiz, A.; Forkey, J. N.; McKinney, S. A.; Ha, T.; Goldman, Y. E.; Selvin, P. R. *Science* **2003**, *300*, 2061.

(18) Ober, R. J.; Ram, S.; Ward, E. S. *Biophysical Journal* **2004**, *86*, 1185.

(19) Juette, M. F.; Gould, T. J.; Lessard, M. D.; Mlodzianoski, M. J.; Nagpure, B. S.; Bennett, B. T.; Hess, S. T.; Bewersdorf, J. *Nature Methods* **2008**, *5*, 527.

(20) Betzig, E.; Patterson, G. H.; Sougrat, R.; Lindwasser, O. W.; Olenych, S.; Bonifacino, J. S.; Davidson, M. W.; Lippincott-Schwartz, J.; Hess, H. F. *Science* **2006**, *313*, 1642.

(21) Rust, M. J.; Bates, M.; Zhuang, X. *Nature Methods* **2006**, *3*, 793.

(22) Hanley, D. C.; Harris, J. M. *Analytical Chemistry* **2001**, *73*, 5030.

(23) Wang, L.; Xu, G.; Shi, Z.; Jiang, W.; Jin, W. *Analytica Chimica Acta* **2007**, *590*, 104.

(24) Li, L.; Tian, X.; Zou, G.; Shi, Z.; Zhang, X.; Jin, W. *Analytical Chemistry* **2008**, *80*, 3999.

(25) Tani, T.; Yamaguchi, Y.; Ohuchi, K.; Oda, M. *Journal of Luminescence* **2004**, *107*, 42.

(26) Wayment, J. R.; Harris, J. M. *Analytical Chemistry* **2006**, *78*, 7841.

(27) Lee, J.-Y.; Li, J.; Yeung, E. S. *Analytical Chemistry* **2007**, *79*, 8083.

(28) Jiang, D.; Wang, L.; Jiang, W. *Analytica Chimica Acta* **2009**, *634*, 83.

(29) Chen, D.; Dovichi, N. J. *Analytical Chemistry* **1996**, *68*, 690.

(30) Keller, R. A.; Ambrose, W. P.; Goodwin, P. M.; Jett, J. H.; Martin, J. C.; Wu, M. *Applied Spectroscopy* **1996**, *50*, 12A.

(31) Fister, J. C.; Jacobson, S. C.; Davis, L. M.; Ramsey, J. M. *Analytical Chemistry* **1998**, *70*, 431.

(32) Currie, L. A. *Analytical Chemistry* **1968**, *40*, 586.

(33) Landau, L.; Levich, B. *Acta Physiochim. U.R.S.S.* **1942**, *17*, 42.

(34) Marques, D.; Costanza, V.; Cerro, R. L. *Chemical Engineering Science* **1978**, *33*, 87.

(35) Lacy, W. B.; Olson, L. G.; Harris, J. M. *Analytical Chemistry* **1999**, *71*, 2564.

(36) Axelrod, D. *Methods in Cell Biology* **1989**, *30*, 245.

(37) Bartco, A. P.; Dickson, R. M. *Journal of Physical Chemistry B* **1999**, *103*, 11237.

(38) Hansen, W. *Journal of the Optical Society of America* **1968**, *58*, 380.

(39) Mortara, L.; Fowler, A. *Proc. SPIE* **1981**, *290*, 28.

(40) Barlow, R. J. *Statistics: A Guide to the Use of Statistical Methods in the Physical Sciences*; John Wiley: Chichester, 1989.

(41) Taylor, J. R. *An Introduction to Error Analysis: The Study of Uncertainties in Physical Measurements*; Second Edition ed.; University Science Books: Sausalito, CA, 1997.

(42) L. Landau, B. L., 17, 42-54. *Acta Physiochim. U.R.S.S.* **1942**, *17*, 42.

(43) Davis, J. M.; Giddings, J. C. *Analytical Chemistry* **1985**, *57*, 2168.

(44) Krustok, J.; Collan, H.; Yakushev, M.; Hjelt, K. *Pysica Scripta* **1999**, *T79*, 179.

(45) Plakhotnik, T.; Moerner, W. E.; Palm, V.; Wild, U. P. *Optics Communications* **1995**, *114*, 83.

(46) Bogart, K. P. *Introductory Combinatorics*; Pitman Publishing Inc.: Marshfield, MA, 1983.

CHAPTER 3

SINGLE MOLECULE FLUORESCENCE IMAGING OF THE INFLUENCE OF IONIC STRENGTH ON DNA HYBRIDIZATION

3.1 Introduction

The complete sequencing of the human genome,[1] has created a large demand for high speed genetic screening and sequencing in clinical diagnosis and bioscience. High-throughput genomic screening typically relies on interactions between solution-phase probe DNA and target DNA immobilized at a solid-aqueous interface.[2] Interfacial assays offer advantages over bulk-solution methods including small sample volumes, high sensitivity, and parallel sampling and readout. Array-based interfacial DNA sensors employ a range of detection schemes, such as fluorescence,[3] capacitance[4] and field effect[5] solid state detectors to measure DNA hybridization. To better understand and design these sensors, we must understand how experimental parameters such as temperature,[6,7] sequence,[8] strand length,[7] net electrical charge[9] and ionic strength[9,10] affect surface-immobilized DNA hybridization.

Many surface-sensitive detection schemes have been used to measure interfacial DNA hybridization, including total internal reflection fluorescence (TIRF),[11] surface plasmon resonance,[12,13] plasmonic nanostructure enhanced fluorescence,[14] and quartz crystal microbalance[10] based assays. These techniques measure an average surface response upon binding of probe DNA to a near-monolayer of surface-immobilized

targets. These methods are good for measuring association constants, but they present some disadvantages for quantifying binding kinetics. Instrument response is difficult to convert to absolute surface molecule density, making binding site density and rates difficult to determine with confidence. In addition, kinetic rates measured in these assays are often limited by slow mass transport to the densely packed surface during concentration-step or wash-off experiments.

One approach to eliminate the influence of mass transport on kinetic rates is to employ a technique that is sufficiently sensitive to measure binding kinetics under equilibrium conditions. TIRF microscopy[15] is able to image individual fluorescent molecules in the 150 nm thick evanescent field generated by excitation radiation internally reflected at the interface. Single molecule TIRF microscopy has been used to measure RNA aptamer-ligand binding,[16] biotin-streptavidin binding,[17] and peptide interactions with lipid bilayers.[18] In their recent work, Jungmann et al.[7] measured hybridization association constants and kinetics for oligonucleotides attached to DNA origami superstructures using single molecule imaging. In these single molecule binding assays, binding rate constants are measured at equilibrium conditions from the lifetimes of bound states for individual molecules, avoiding any artifacts in the kinetics from mass transport.

In this present work, we have employed single molecule TIRF microscopy to measures kinetics and association constants between complementary probe and target single-stranded DNA (ssDNA) molecules, as outlined in Figure 3.1. Target ssDNA was covalently immobilized to glass surfaces using copper-catalyzed azide-alkyne cycloaddition “click” chemistry.[19,20] Click immobilization results in covalent attachment

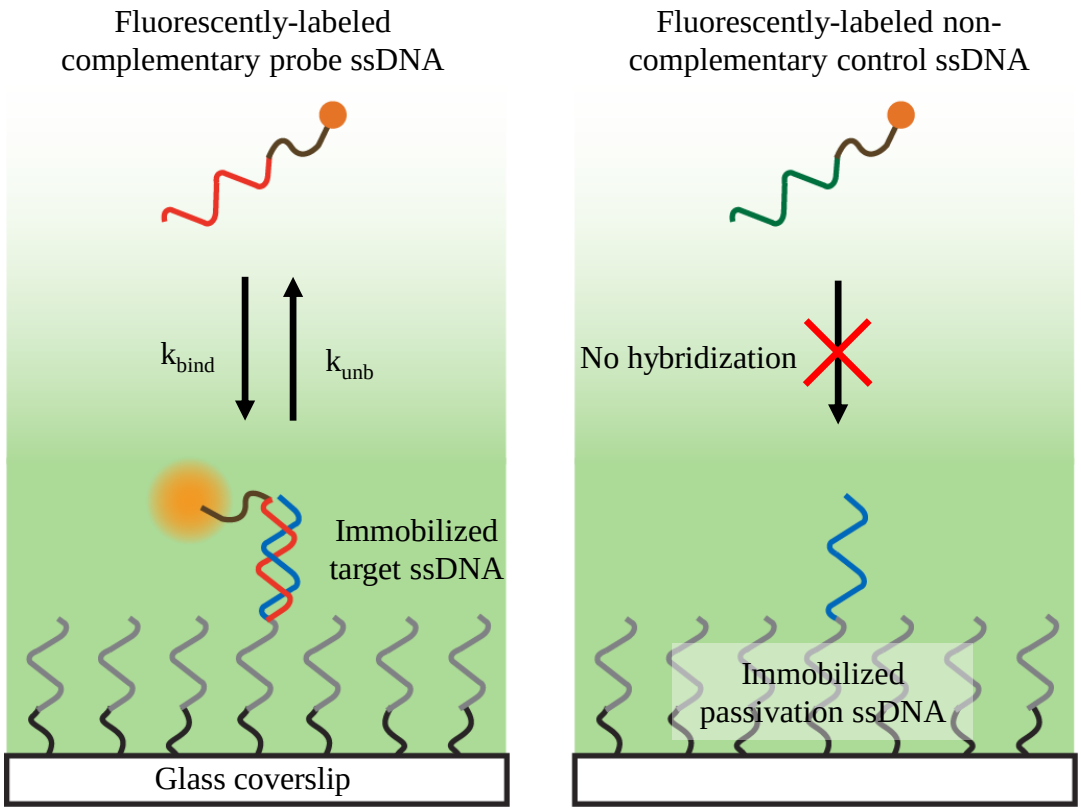

Figure 3.1. Illustration of complementary strand hybridization between solution-phase fluorescently labeled "probe" ssDNA and surface-immobilized "target" ssDNA.

of target DNA to substrates and is potentially more resistant to degradation than non-covalent immobilization (e.g., biotin-streptavidin binding, electrostatic adsorption). Association constants between fluorescently-labeled 10-mer probe ssDNA and immobilized target DNA were determined by counting hybridized double-stranded DNA (dsDNA) complexes in fluorescence images. Hybridization is reversible at room temperature with oligonucleotides shorter than 10 base pairs, and the lifetime of hybridized dsDNA complexes was determined from single molecule residence times. In interfacial binding assays, binding site surface density is often uncertain, making it difficult to quantify the association rates for binding. The binding site density was determined in this work by fitting the Langmuir equation to a fluorescence intensity binding isotherm calibrated with single molecule populations measured on the same capture surface at low concentrations.

We used this methodology to quantify the effect of ionic strength on DNA hybridization. The backbone of DNA is highly charged, with between 0.1 and 0.5 net electron charges per phosphate group,[21] so that complementary DNA strands must overcome significant electrostatic repulsion in order to hybridize. Increasing electrolyte concentration screens this charge-charge repulsion, resulting in more stable bound duplexes,[9] increased binding rates and decreased unbinding rates.[10] The results show that by varying ionic strength in probe DNA solutions by a factor of 30, association constants increased by three orders of magnitude. Ionic strength influenced both binding and unbinding kinetics; the binding rate constant increased 100 fold, and unbinding rates decreased 30 fold. An Eyring transition state model has been developed to estimate the electrostatic and nonelectrostatic contributions to the free energies of the transition state

and the stability of the hybridized dsDNA complex from the changes in kinetic rate constants with ionic strength. Results from this model indicate that the free energy of the dsDNA complex has a stronger dependence on ionic strength than the free energy of the hybridization transition state. This is a result of greater charge repulsion in the hybridized DNA duplex compared to the transition state; the results suggest that only a fraction of the DNA bases interact at the transition state between separated DNA strands and the bound duplex.

3.2 Experimental Section

3.2.1 Chemicals and Materials

Chemically modified oligonucleotides for surface immobilization and fluorescence binding detection, shown in Figure 3.2, were synthesized and HPLC purified by the University of Utah HSC Core DNA synthesis facility. Oligonucleotide with attached alkyne, polyethylene glycol, and Cy3 fluorescent target were assembled with solid phase phosphoramidite chemistry, and were used as received. Buffers and DNA stock solutions were prepared with water purified to a solution resistivity of 18 MΩ·cm using a Barnstead NANOpure II system (Boston, MA). Oligonucleotides stock solutions were dissolved in purified water, and their solution concentration determined from their absorbance at 260 nm.[22] Copper (I) iodide (Alfa Aesar, 99.998 %), sodium azide (Alfa Aesar, 99%) GR ACS grade dimethylsulfoxide (DMSO) (EMD Chemical), spectroscopy grade Omnisolve methanol (EMD chemicals), dimethylformamide (DMF) (Fisher Scientific, 99%), UltimAR n-heptane (Macron Chemicals) and Gold Seal glass 22 x 22 mm no. 1.5 coverslips were purchased from VWR. Bioxtra sodium L-ascorbate (Sigma Life Science, 99% +), and tris [(1-benzyl-1*H*-

Fluorescently labeled ssDNA

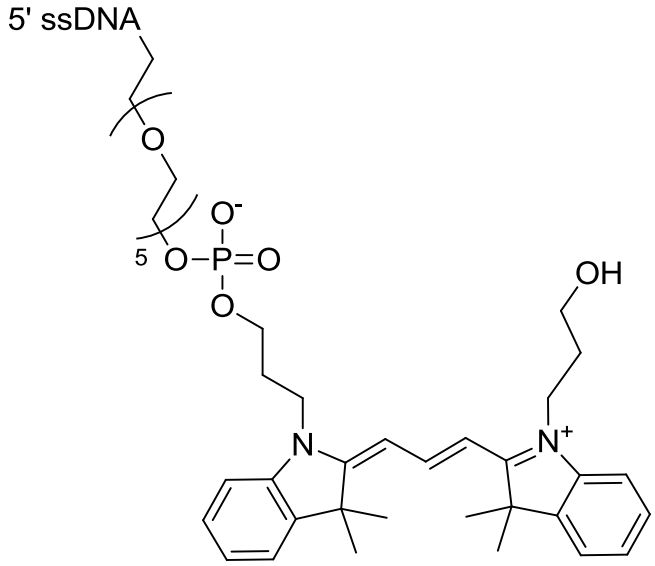

Alkyne-terminated ssDNA

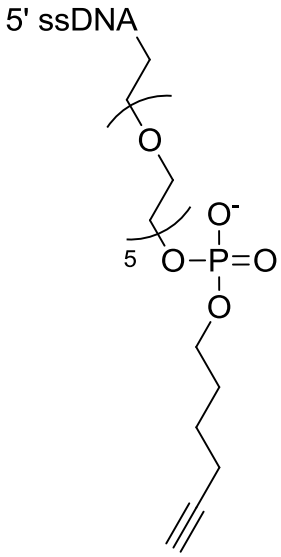

Passivation ssDNA:
5'-C≡C-PEG$_6$-TGT TCA TCA TGC-3'
Target ssDNA:
5'-C≡C-PEG$_6$-TGT TCA TCA TGC GTC GTC GGT ATA TCC CAT-3'
Probe ssDNA: 3'-A TAT AGG GTA-PEG$_6$-Cy3-5'
Control ssDNA: 5'ACT CGA TGA TGA-PEG$_6$-Cy3-5'

Figure 3.2. Chemical structures of fluorescently labeled probe and control ssDNA, left, and alkyne terminated probe and passivation ssDNA, right; sequences of passivation, target, probe and control ssDNA, below.

1, 2, 3-triazol-4-yl) methyl] amine (TBTA) (97% Aldrich) were purchased from Sigma Aldrich. 3-bromopropyl trimethoxy silane (BPTMS) was purchased from Gelest. Phosphate buffers were made using ACS grade monobasic sodium phosphate, adjusted to pH using concentrated sodium hydroxide solution, with additional sodium chloride (all Malinckrodt) added.

3.2.2 "Click" Oligonucleotide Immobilization on Glass

Glass coverslips for DNA immobilization were first cleaned by rinsing in 18 MΩ·cm water, followed by methanol, and cleaned for 25 minutes per side with an ultraviolet ozone cleaner, Jelight Co. model 342. Clean glass surfaces were silanized via assembly of BPTMS out of dry n-heptane, similar to a method described by Wayment et al.[23] Before use, n-heptane was dried for at least 24 h over sodium metal, and then filtered through a 0.2 μm Whatman Puradisc polyether sulfone 25 mm syringe filter. Clean glass slides were immersed in 10 mM of BPTMS dissolved in dry n-heptane to deposit a monolayer. After 2.0 h, glass slides were removed, rinsed in n-heptane, toluene, and methanol sequentially, and placed in a 110º C oven for 1.5 h to allow adsorbed water to crosslink the BPTMS monolayer. Coverslips showed changes in water contact angle after BPTMS deposition, from 0º for cleaned slides to 60º for modified slides. The terminal bromide on BPTMS modified coverslips was substituted for azide by exposing the coverslips to saturated sodium azide dissolved in DMF for 24 h, followed by rinsing in DMF and methanol.[24-26] Caution: sodium azide is toxic and can react violently with halogenated solvents, Brönsted acids, and transition metals; users of this reagent should take appropriate precautions.[27]

Alkyne terminated oligonucleotides were covalently linked to surface azide groups[28] via copper catalyzed 1,3-dipolar cycloaddition "click" chemistry,[19,20] assisted by polytriazole copper (I) stabilizing ligand.[29] A 1:40 reaction mixture of "target" 30-mer ssDNA (complementary to the fluorescent "probe" ssDNA) and "passivation" 12-mer ssDNA (noncomplementary to probe ssDNA) was immobilized; sequences are shown in Figure 3.2, and the immobilization scheme is shown in Figure 3.3. Oligonucleotides were linked to the azido-coverslips out of a mixture of 50 nM alkyne passivation ssDNA, 2 μM alkyne target ssDNA, 0.5 mM copper (I) iodide solubilized with 1 mM TBTA, 0.5 mM sodium ascorbate and 130 mM KCl in 33% water and 67 % DMSO. The coverslip reaction proceeded for 24 h, followed by rinsing in DMSO, 1% ammonium hydroxide, and water, and storage in methanol. 1,3-dipolar cycloaddition between terminal alkynes and azides result in stable 1,4-disubstituted 1,2,3-triazoles, and copper (I) catalysis speeds this reaction at room temperature.[19,20] Addition of a polytriazole ligand such as TBTA increases cycloaddition yield,[29] and inhibits generation of reactive oxygen species by copper (I) which can damage DNA.[30] Without TBTA present, we saw inconsistent hybridization to surface-bound DNA. Sodium ascorbate was present to reduce any copper (II) generated by oxygen reduction back to copper (I). Potassium chloride was present to reduce electrostatic repulsion between DNA phosphate groups and thus ensure high surface coverage.

3.2.3 TIRF Microscopy

DNA modified coverslips were assembled into an imaging flow cell consisting of a 145 μm thick acrylic-polyester double-stick gasket (3M, part number 9495MPF) sandwiched between the coverslip and a glass top-plate with sample inlet and outlet ports.

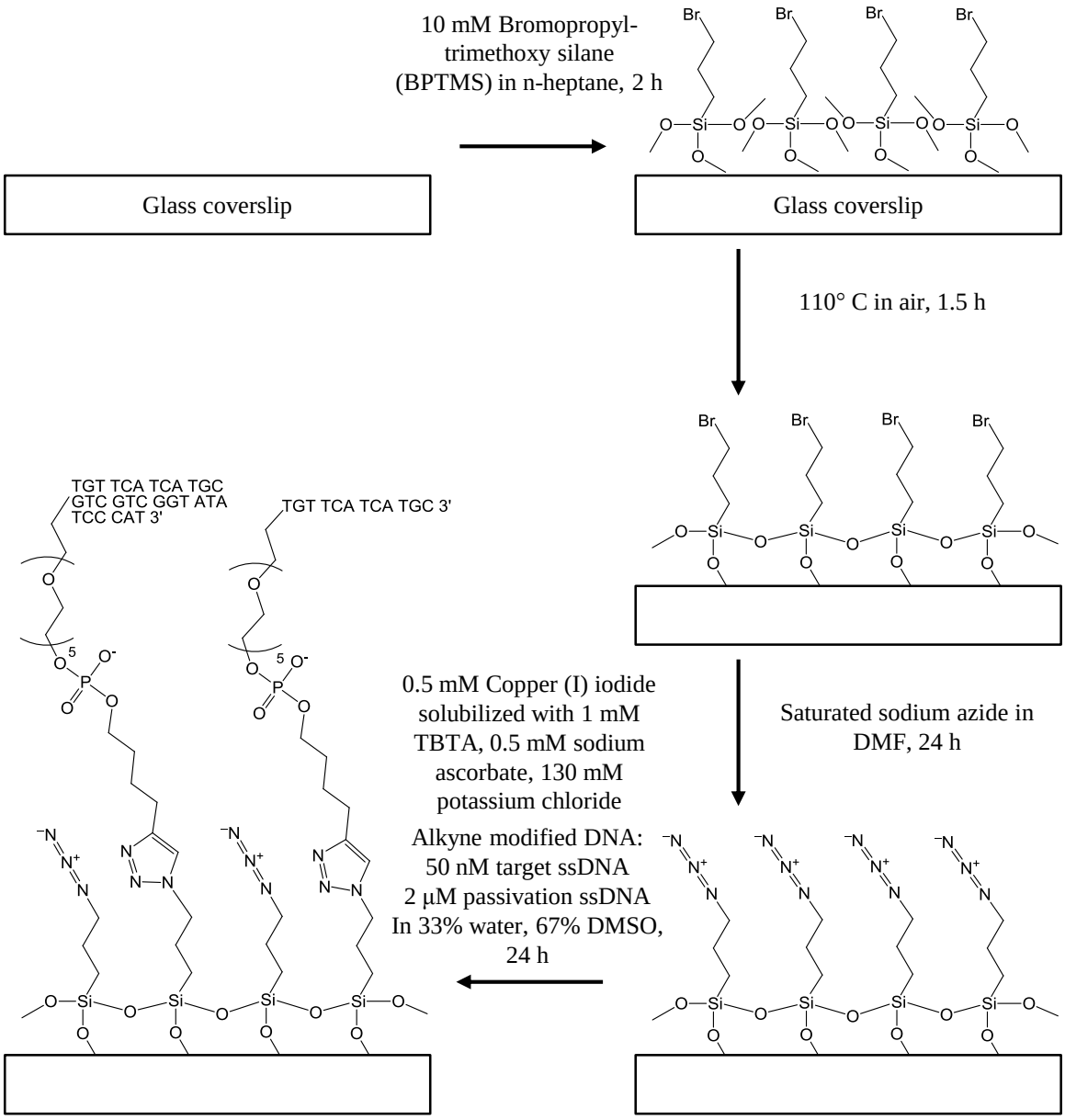

Figure 3.3. Target ssDNA immobilization chemistry on glass coverslips, clockwise from top left: BPTMS adsorption to surface, BPTMS crosslinking, nucleophilic substitution of terminal bromide for terminal azide, copper catalyzed “click” covalent attachment of ssDNA.

A 10 mm x 3mm channel cut out of the gasket connected the top-plate inlet and outlet ports. Probe ssDNA solutions were flowed through the channel at 30 μL min^{-1} with a PHD 2000 Harvard Apparatus syringe infusion pump during hybridization experiments, replacing the channel volume seven times per minute to ensure a constant concentration of probe DNA over the surface. Experiments were conducted at 23 ± 1 °C. Hybridization was monitored in situ using a Nikon TE200 microscope equipped with a home-built through-the-objective TIRF illumination system. The TIRF illumination path began with 514.5 nm emission from a Lexel model 95 argon ion laser coupled into a single-mode polarization-maintaining optical fiber (Thorlabs) with a focusing lens (Thorlabs PAF-X-5-A FiberPort). Low intensity illumination light (165 μW) from the opposite end of the optical fiber was collected by a collimating plano-convex lens, directed through a band pass filter (Semrock), and focused onto the back focal plane of the microscope objective by a second plano-convex lens. The oil immersion microscope objective (100x apo TIRF 1.49 numerical aperture, Nikon) generated a collimated beam that illuminated the sample. Translating the optical fiber normal to the optical axis shifts the angle of the illumination beam to the sample surface, and at sufficiently high angles, total internal reflection is produced at the glass-aqueous interface.

Images of fluorescence interface were detected with a Photometrics Cascade II electron multiplying charge coupled device (EMCCD) camera in a 32 x 32 μm (200 x 200 pixel) region. Images were collected using 500 ms integrations, either in real time or in 4.0 s time lapse intervals, at electron-multiplying gain set at 3250 (in arbitrary units) and a readout speed of 10 MHz. For the high-coverage binding assay, the average fluorescence intensity was measured by averaging pixel charge in a 16 x 10 μm (100 x 65

pixel) region near the center of the image. For this average fluorescence measurement, the camera was operated with 500 ms integrations, electron-multiplying amplification deactivated, and 1 MHz readout speed. The DC offset (dark counts) drifted downward over the first 60 images collected in videos, to a steady-state offset. To simplify background correction, the first 60 frames of all videos were discarded to achieve a uniform offset. All images were collected as 16-bit monochrome TIF image stacks using Metamorph imaging software version 6.2r6 (Molecular Devices).

3.2.4 Image Analysis for Detecting and Counting Single Molecules

Image analysis for counting molecules, measuring residence times, and measuring fluorescence intensities was performed using programs written in for Matlab 7.12.0 (Mathworks). Images were prepared for analysis by converting pixel intensity values from arbitrary counts in analog-to-digital units (ADU), I_{ADU}, into photoelectron (PE) counts, I_{PE}, using a scaling factor described by Mortara et al.[31] Photoelectron counts exhibit Poisson-like error where the mean counts equal twice their variance, $\mu_{PE} = 2\nu_{PE}$, and the electron multiplying amplifier on the EMCCD camera doubles the variance of the measured charge relative to the Poisson photoelectron limit.[32] The measured mean and variance in ADU and ADU^2, respectively, for images of uniform white noise follow the expected linear relationship as shown in Figure 3.4. The slope and intercept of a line $y = F(x + I^0)$ fit to a plot of pixel ADU mean and variance exhibits a slope, F, and the DC sensor offset intensity, I^0, respectively. I_{ADU} is converted to I_{PE}, using equation 3.1.

$$I_{PE} = \frac{2}{F}(I_{ADU} - I^0) \qquad [3.1]$$

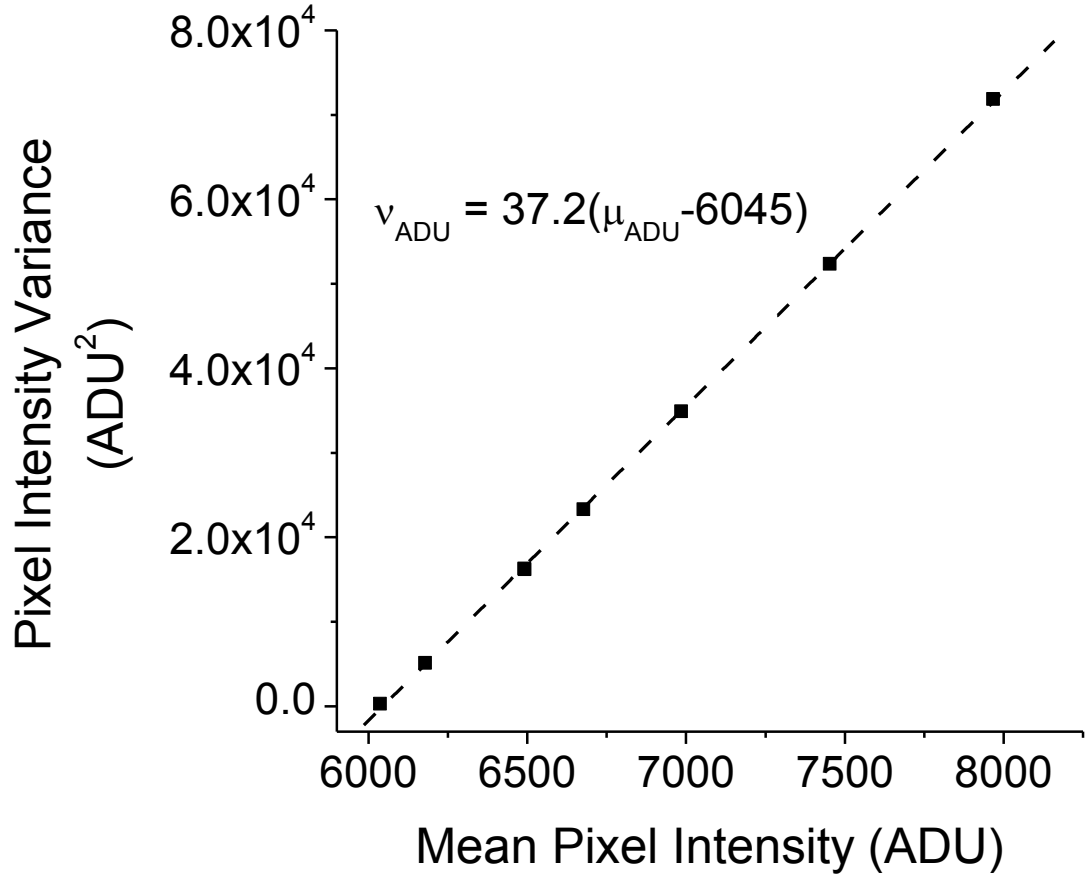

Figure 3.4. ADU mean-variance plot to determine photoelectron conversion factor, I_{ADU} is plotted as black squares, and the best fit line plotted as the dashed line, with equation shown.

Single molecule spots with signal-to-noise ratios of ~2.6 were detected using an intensity threshold which relies on the finite size of the diffraction-limited point spread function (PSF).[33] Single molecule spots were detected by locating 0.480 x 0.480 μm (3 × 3 pixel) regions with three or more pixels brighter than an intensity threshold, I_{thold}, set at n_{std}-times the background standard deviation, σ_{bg}, above the mean background intensity, μ_{bg}: $I_{thold} = n_{std}\sigma_{bg} + \mu_{bg}$. The resolution limit of the detection scheme was set by a 0.6 μm radius circle defining the minimum separation distance between molecules. Within the minimum separation distance, the coordinate for each molecule was measured to sub-pixel precision by calculating its intensity center-of-mass.

Mean background intensities for each video were estimated by locating the peak value in a histogram of I_{PE}. An example I_{PE} histogram for blank 500 mM ionic strength phosphate buffer is shown as the open squares in Figure 3.5. When more single molecule spots appear in images μ_{bg} increases,[33] requiring μ_{bg} and σ_{bg} to be measured for every image. We cannot measure σ_{bg} in images of many single molecule spots directly because intensity from single molecules skews the tail of the I_{PE} histogram. We avoid this problem by taking advantage of the Poisson-like error of the background intensity. Since $\nu_{bg} = 2\mu_{bg}$ (see above) the background noise standard deviation can be estimated from the mean background value: $\sigma_{bg} = (2\mu_{bg})^{½}$. Mean backgrounds are measured from the peak value of the I_{PE} histogram. By increasing n_{std}, I_{thold} increases and fewer spurious noise spots are detected as false positives. If the threshold is set too high, the intensity of actual molecule PSFs will not exceed I_{thold} and molecules will be missed, increasing the false negative probability. When detecting single molecules, see Figure 3.6a for an example image, n_{std} was tuned between 2.8 and 3.4 depending on noise in the image background

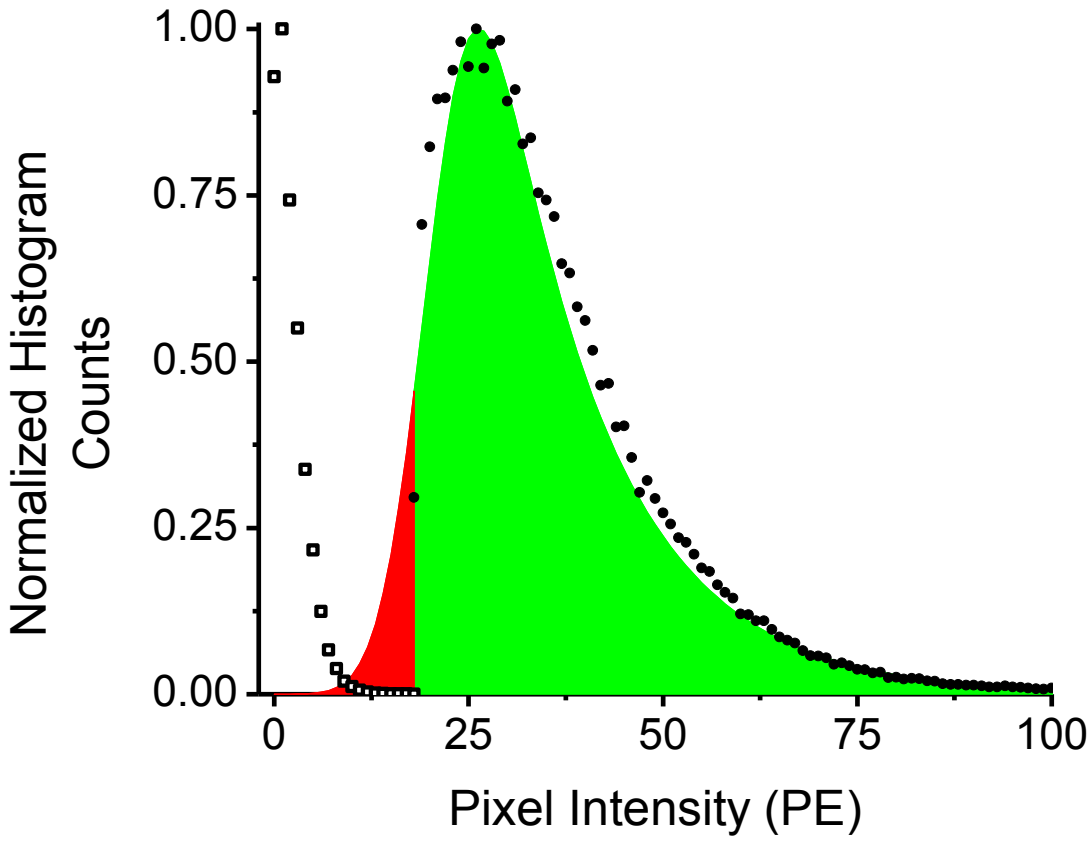

Figure 3.5. I_{PE} histograms: comparison of blank background (open squares) and third most intense (critical) pixel intensity (black circles); an exponentially modified Gaussian function fit as shown with fraction below threshold colored red (5 %), and section above threshold colored green (95%).

and the number of molecules detected. We adjusted n_{std} to minimize the false negative probability, and keep the false positive probability below 0.5 % of the total molecules counted. The false positive probability for this algorithm has been described previously[33] and varies from 1 to 0.005 molecules per frame for n_{std} = 2.8 and 3.4, respectively.

False negative probabilities were determined from histograms of the "critical pixel" intensity, I_{crit}. The critical pixel is the third most intense pixel in the PSF, and determines whether the molecule meets the intensity threshold. A histogram of I_{crit} for molecules detected in 1.6 pM DNA and 500 mM ionic strength is plotted in Figure 3.5, along with an empirical exponentially modified Gaussian function fit.[33] The lower edge of the I_{crit} histogram is cut off by I_{thold}, set at 19 PE; any molecules less intense than the threshold will not be counted. The fraction of molecules above the intensity threshold can be calculated from the ratio of the area above I_{thold} to the total area integral. The fraction of molecules detected is 95 %, resulting in a false negative probability of only 5%.

To calculate equilibrium surface populations, probe complexes were counted in 5 to 30 individual images captured 20 min after sample injection. Videos were sampled in time intervals corresponding to twice the molecule unbinding time, 4 to 100 s, to ensure sampled populations were uncorrelated and accurately represented counting uncertainties. In addition, raw molecule counts were adjusted using a Poisson statistical model[33,34] to account for any unresolved overlapping molecules, where actual populations, N_{act}, are calculated from measured populations of fluorescent spots, N_{meas}, as follows:

$$N_{act} = N_{max} \ln\left(1 - \frac{N_{meas}}{N_{max}}\right) \qquad [3.2]$$

The quantity N_{max} is the maximum number of molecules resolvable by the detection algorithm. For 1024 μm^2 images, and a minimum area per molecule defined by the minimum separation distance for the detection algorithm, $(0.64\ \mu m)^2 = 0.41\ \mu m^2$, N_{max} = 2500 molecules. At surface densities below 0.2 μm^{-2} (~200 molecules) this correction factor is negligible, but at 0.6 μm^{-2} (~600 molecules) the correction is about 15 %.

3.2.5 Measuring Single Molecule Residence Times

The residence time for each molecule on the surface was measured by tracking its intensity center of mass in sequential video frames. Starting at the beginning of a video, for every molecule coordinate the analysis program looks ahead in the subsequent video frame for a coordinate within a detection radius of 0.32 μm of the previous coordinate. If a match is found, the program continues stepping forward in time and repeats this process. When the molecule unbinds, no more matching coordinates will be found, and the program logs the residence time. Probe ssDNA used in this study is labeled with one fluorophore and is subject to photobleaching and photoblinking. Photobleaching molecules appear to unbind prematurely when they enter a dark state. Permanent photobleaching is mitigated by using low illumination intensities and time lapse imaging; see below for details. Photoblinking or transitions to long-lived dark states cause a molecule to flicker in intensity,[35,36] and each brief light-dark transition may be mistaken for a binding event. The impact of photoblinking was reduced by defining a "frame skip" time, τ_{fs}, which allows the tracking program to look ahead several frames after a molecule has disappeared to see whether it returns. At sufficiently low densities of DNA, the probability of a new probe ssDNA binding at the same coordinate as a molecule that departed seconds ago is negligible; therefore, it is probable that the label on the original

bound ssDNA entered a brief dark state. We evaluated the impact of τ_{fs} on single molecule residence times, where τ_{fs} between 0 and 3.5 s increases apparent residence times, as photoblinking events are corrected, but τ_{fs} beyond 4.0 s had minimal impact on residence times. The frame skip time could artificially extend residence times if new probe ssDNA binds near a previously detected molecule within τ_{fs}. The number of new molecules, N_{bind}, that bind within the frame skip window can be determined from the area of the site correlation tolerance, $A = 0.322\ \mu m^2$, the highest measured probe ssDNA binding rate, $r_{bind} = 1.9 \times 10^{-5}\ s^{-1}$, the binding site density, $\Gamma_{max} = 2500\ \mu m^{-2}$, and $t_{fs} = 4.0$ s:

$$N_{bind} = \Gamma_{max} A r_{bind} t_{fs} \qquad [3.3]$$

For the values listed above, corresponding to the highest binding rate measured at 150 mM electrolyte and 9.5 pM probe ssDNA, $N_{bind} = 0.06$ per τ_{fs}. This binding rate results in a negligible probability of site binding during τ_{fs}. In the worst case, only 6 % of molecule residence times are affected by the frame skip algorithm.

3.3 Results and Discussion

3.3.1 Complementary DNA hybridization to Immobilized DNA

Hybridization of fluorescently labeled ssDNA was monitored in situ according to Figure 3.1. A mixed layer of 30-mer "target" ssDNA and 12-mer "passivation" ssDNA was immobilized on a glass surface in a 1:40 ratio as described above. Target ssDNA was diluted into passivation DNA to avoid barriers to hybridization caused by crowding,[28] while still maintaining a dense surface coverage of ssDNA similar to DNA screening chips. Hybridization with target ssDNA was detected using a Cy3 labeled 10-

mer “probe” strand complementary to the last 10 bases of the solution-facing 3’ end of the target. In order to verify that interactions between probe ssDNA and the surface were due to hybridization and not nonspecific adsorption, a fluorescently labeled “control” 12-mer with no complementary overlap with target ssDNA was tested. Control ssDNA has similar base pair content, but a scrambled sequence relative to the probe ssDNA.

To initiate hybridization experiments, solutions of fluorescently labeled ssDNA containing 0.5 mM pH 8.0 phosphate buffer and varying amounts of sodium chloride were flowed over target ssDNA-modified surfaces. Probe or control ssDNA hybridization or non-specific interactions were detected in situ using fluorescence imaging. Figure 3.6a shows example 32 × 32 μm images of a buffer blank, 1.25 pM control ssDNA, and 1.6 pM probe ssDNA in 500 mM ionic strength buffer. Individual molecules have been located and highlighted via the intensity threshold detection scheme described above. Figure 3.6b shows the average number of molecules counted in images of hybridization at equilibrium; error bars are two standard deviations of the average. The probe ssDNA population is significantly higher than either blanks or control ssDNA populations, which we attribute to strong complementary strand hybridization. DNA capture surfaces exhibit excellent selectivity; from a 1.6 pM solution, the probe ssDNA produces a population that is 20 times higher than the blank spots, and 16 times higher than blank subtracted control ssDNA populations. The response of probe DNA populations to solution concentration is linear; Figure 3.7 shows the bound probe DNA populations for solutions ranging from 0 to 3.2 pM probe ssDNA in 500 mM ionic strength buffer. In order to interpret this accumulation result and determine binding

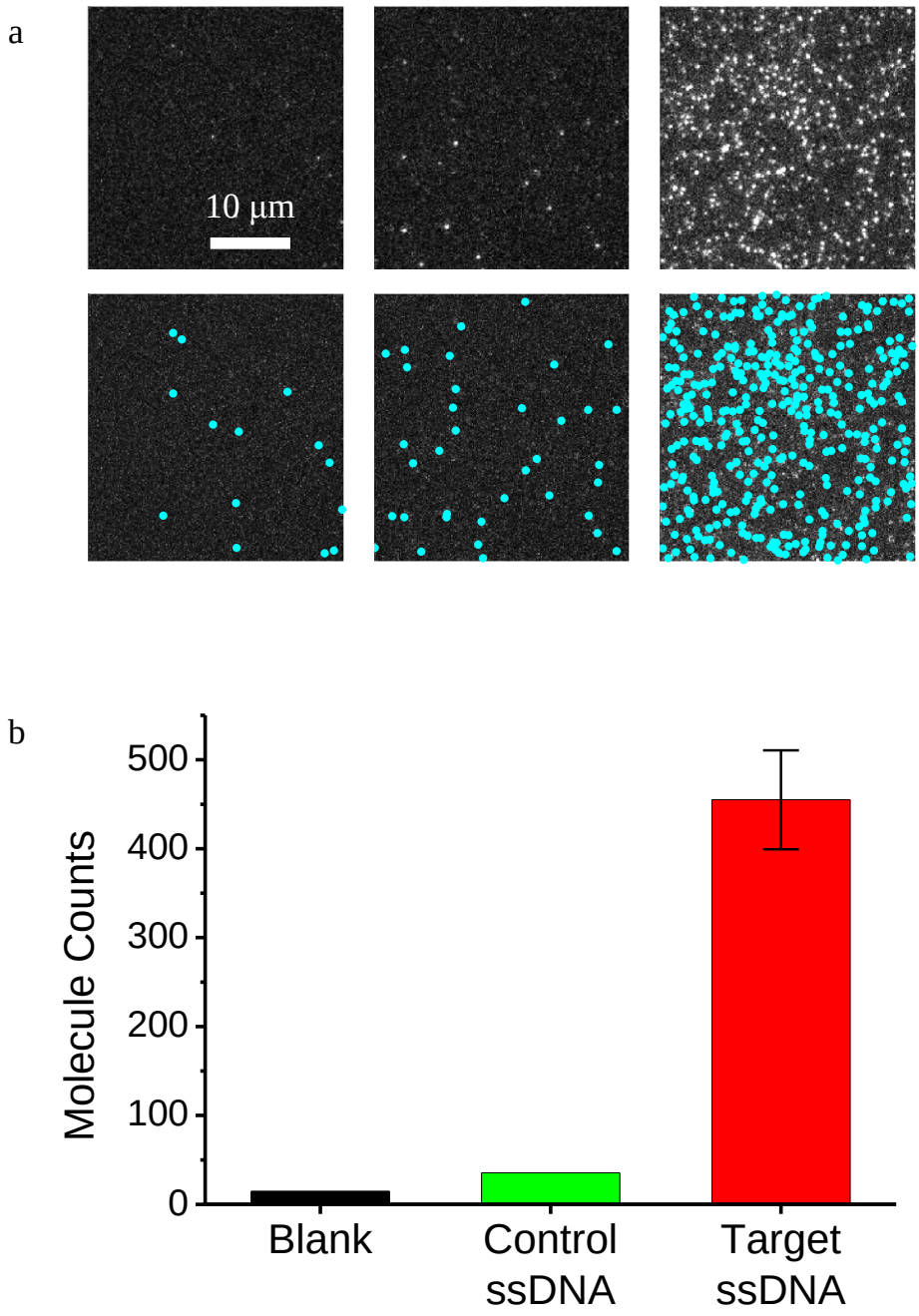

Figure 3.6. Comparison of blank controls and images of hybridized complexes: a) above: images of buffer blank (left), 1.25 pM NC ssDNA (center), and 1.6 pM FC ssDNA (right), in 0.5 mM pH 8 phosphate buffer with 500 mM sodium chloride; below: highlighted locations of single molecules; b) mean single molecule counts in images from the above solution conditions. Error bars are 2 standard deviations of the mean for target ssDNA, and are too small to be visible for the blank and control ssDNA.

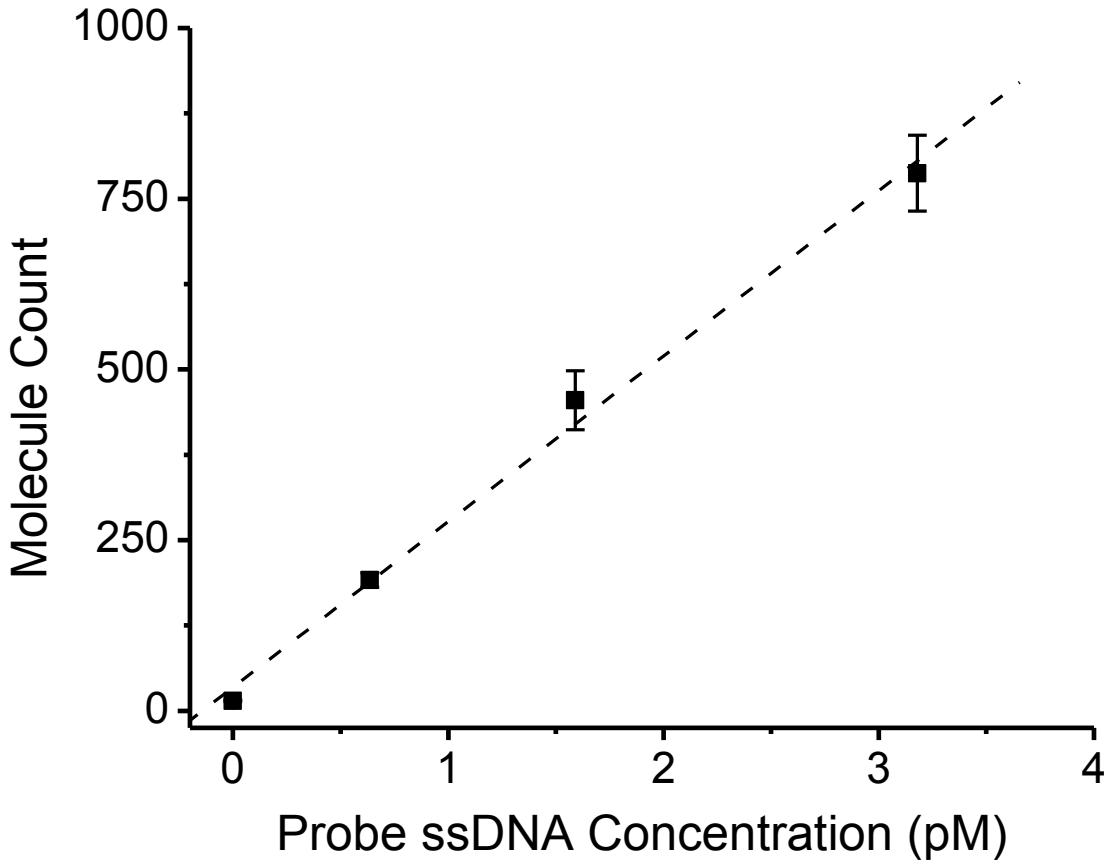

Figure 3.7. Probe-target dsDNA complex concentration response, populations of probe ssDNA hybridized at surface in 0.5 mM pH 8 phosphate buffer and 500 mM sodium chloride counted in 32 × 32 μm images. Error bars are 2 standard deviations of the mean.

association constants, a Langmuir binding model is needed to describe DNA hybridization at an interface.

3.3.2 Combined Fluorescence Intensity and Single Molecule Binding Assay

The bimolecular reaction between probe and target complementary ssDNA to form dsDNA was modeled using a Langmuir binding isotherm, equation 3.4, where Γ is the surface density of the hybridized dsDNA complex, Γ_{max} is the total surface density of bound and unbound target DNA, K_a is the association constant, and $[DNA_p]$ is the concentration of probe ssDNA in solution:

$$\Gamma = \Gamma_{max} \frac{K_a[DNA_p]}{1+K_a[DNA_p]} \quad [3.4]$$

At low probe ssDNA concentration, $K_a[DNA_p] << 1$ and equation 3.4 simplifies to a linear Langmuir model:

$$\Gamma \approx \Gamma_{max} K_a[DNA_p] \quad [3.5]$$

We can first estimate Γ_{max} from literature data on similar DNA capture surfaces; Devaraj et al.[28] used click chemistry to attach ssDNA to self-assembled monolayers on gold and evaluated DNA surface density electrochemically.[28] In both of our immobilization schemes, the radius of ssDNA is greater than the radius of individual surface reaction sites, so we expect similar ssDNA-size-limited immobilization densities. Assuming target and passivation ssDNA react to the surface based on their stoichiometric ratio in solution, we expect surface site densities similar to those in Devaraj of 2.75×10^{11} cm^{-2}, or 2.8 million binding sites per 32 × 32 μm image. The most molecules per

frame which can be resolved reliably is approximately 1000, corresponding to only 0.04% of the total binding sites. The maximum bound single molecule populations (Figure 3.7) are within the linear region of the Langmuir model, but surface coverage must approach Γ_{max} to fit the roll-over in equation 3.4 in order to measure Γ_{max} and K_a independently. Another technique, therefore, is needed to measure higher Γ.

TIRF intensity assays detect binding of fluorophores by measuring their integrated fluorescence intensity from the interfacial evanescent field region. These assays have been used to detect biotin-streptavidin binding,[37] antibody-antigen interactions,[38] and small molecule-lipid association.[39] Due to uncertainties in light collection, interface illumination, fluorophore absorption, and quantum yield, it is difficult to quantify actual surface populations with fluorescence intensity alone. We can overcome this challenge by performing a TIRF fluorescence assay with the same imaging instrument used to count single molecules. When populations exceed the limit for single molecule counting, the total image intensity can be integrated, using the same camera as a sensitive photodetector. The TIRF microscope can seamlessly transition from single molecule counting to measuring fluorescence intensity on the same sample.

We have measured a fluorescence intensity binding isotherm at high ionic strength, 750 mM sodium chloride, to minimize electrostatic repulsion between surface bound DNA and ensure complete hybridization of target sites. A plot of bound DNA surface density, calculated from single molecule populations, for probe ssDNA solution concentrations between 0.125 and 0.635 pM is in Figure 3.8a. A calibration line, corresponding to equation 3.5 with slope $\Gamma_{max}K_a = 0.18 \pm 0.2$ cm, was fit using linear least squares and plotted as a dashed line in Figure 3.8a. Higher surface densities were

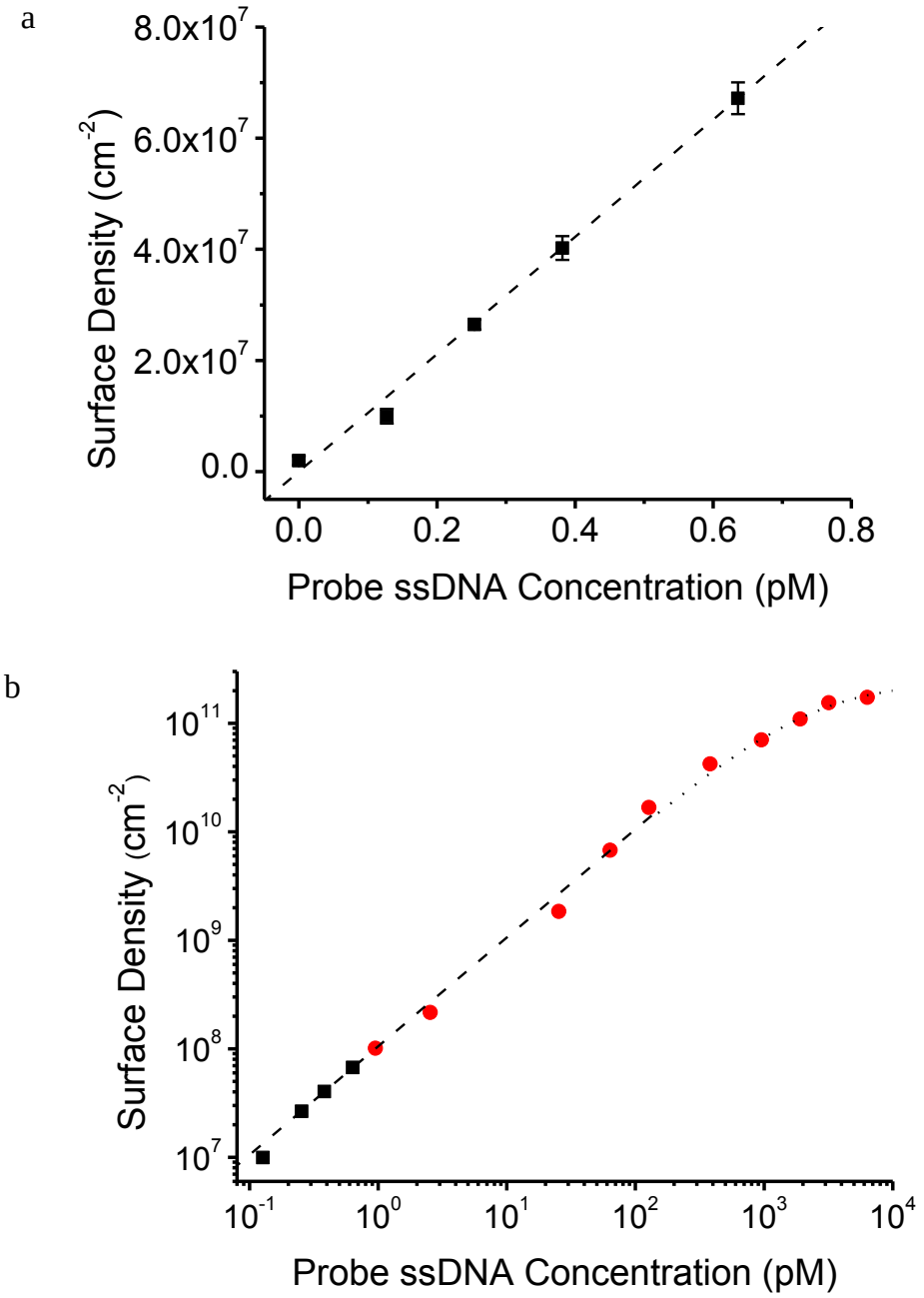

Figure 3.8. Single molecule-fluorescence intensity calibration curve, a) single molecule surface density (black squares), with best fit calibration line (dashed line), b) single molecule surface density and calibration line as above, with average fluorescence intensity calibrated by single molecule best fit line (red circles), with nonlinear Langmuir isotherm fit (dotted line), measured in 0.5 mM pH 8 phosphate buffer and 750 mM sodium chloride.

observed at 750 mM ionic strength compared to those at 500 mM (shown in Figure 3.7) as a result of a significantly higher K_a due to less electrostatic repulsion (see below). Fluorescence intensity was measured for concentrations ranging from 1 pM to 6.35 nM by integrating a 16 × 10 μm image region *on the same sample and field of view used to count single molecules.* Fluorescence intensities were standardized to single molecule populations by multiplying the linear part of the isotherm, 1.0 to 380 pM, by a scaling factor to fit the single molecule best-fit calibration line by weighted linear least squares. These scaled, calibrated intensity data are plotted in Figure 3.8b. Finally, a Langmuir isotherm, equation 3.4, was fit to the calibrated Γ curve to determine Γ_{max} and K_a individually, while fixing the product $\Gamma_{max}K_a$ to the calibration line slope. This fitted Langmuir isotherm is shown as the combined dashed and dotted line in Figure 3.8b.

The measured binding site density, $\Gamma_{max} = 2.5 \pm 0.3$ cm^{-2}, is very close to the value predicted by stoichiometric dilution of densities reported by Devaraj et al.[28] This suggests that the "click" immobilization scheme may allow quantitative control of mixed ssDNA surface compositions on glass, but further work is needed to investigate Γ_{max} scaling with ssDNA composition and structure. With a reliable measure of Γ_{max}, K_a can be determined from single molecule counting data using equation 3.5. From the results in Figure 3.8a for 750 mM ionic strength, we determine a DNA hybridization $K_a = 4.3 \pm 0.6 \times 10^8$ M^{-1}.

The combination of high K_a, Γ_{max}, and sensitivity makes single molecule TIRF imaging a sensitive DNA hybridization sensor. The probe ssDNA limit of detection, determined from the buffer blank uncertainty, is presently 15 fM, which is similar to limits of detection reported for single molecule assays using longer probe ssDNA.[40] The

detection limit is governed by the DNA binding sensitivity, the product $\Gamma_{max}K_a$ from equation 3.5, which could be increased further by using longer probe ssDNA resulting in a higher K_a, where increasing oligonucleotide length by one base should increase K_a by an order of magnitude.[7] Single molecule TIRF imaging could be used to study interactions between other biomolecules and immobilized oligonucleotides with association constants in the 10^8 to 10^9 M^{-1} range, such as RNA aptamer-ligand[16] and peptide nucleic acid hybridization.[41] Association constants alone do not completely describe these interactions; knowledge of binding and unbinding kinetic rates can help further elucidate their mechanisms.

3.3.3 Measuring Unbinding Rates with Single Molecule Residence Times

Using methodology described above, the residence time of individual molecules on the surface was also measured, and the characteristic probe-target ssDNA unbinding time was determined from the histogram of molecule cumulative residence times fit to an exponential decay function. The cumulative histogram is an integral form of the residence time histogram which reduces noise on the tail of the distribution where there are fewer events. Experimental residence histograms measured at high ionic strength exhibited biexponential decay, such as the unbinding data measured at 500 mM ionic strength shown in Figure 3.9. Biexponential histograms were fit to a function where the histogram counts, N_{surv}, are represented by the sum of two exponential functions with pre-exponential factors A_1 and A_2, and unbinding times of τ_{unb1} and τ_{unb2}, shown in equation 3.7.

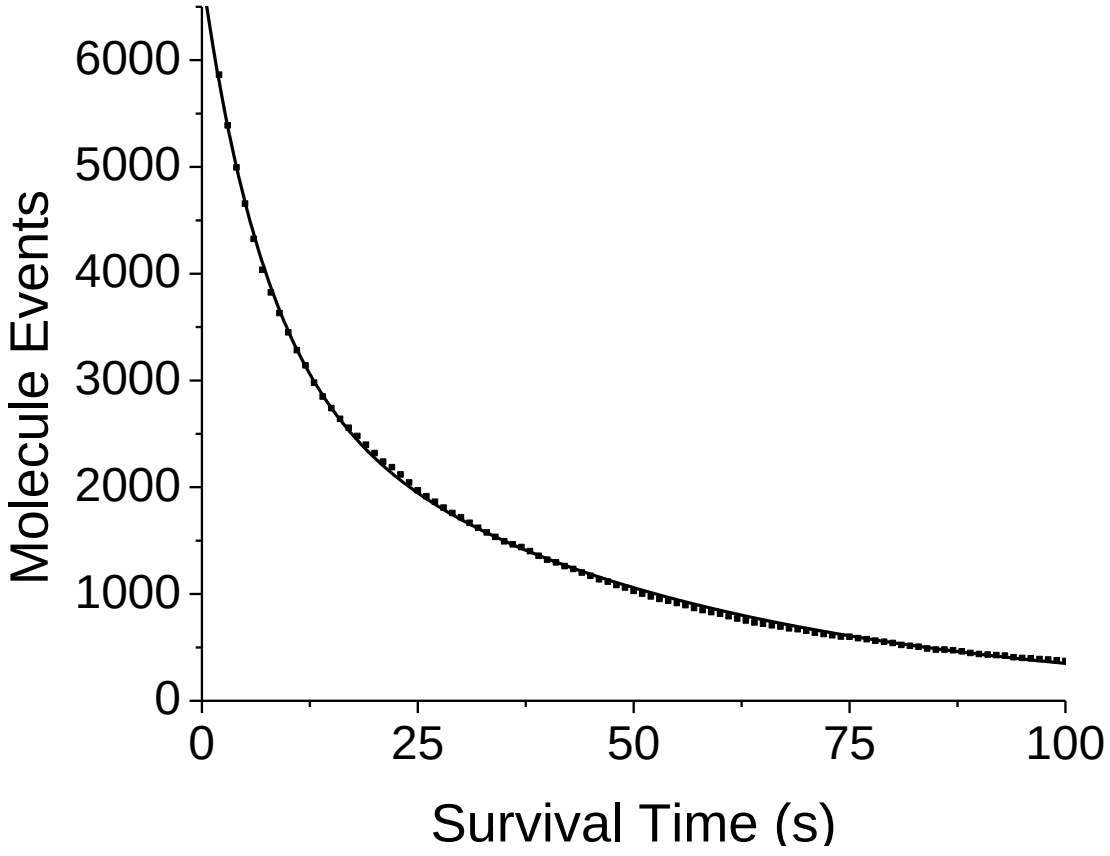

Figure 3.9. Single molecule survival time histogram (black squares) for 1.6 pM target ssDNA, 0.5 mM pH 8 phosphate buffer and 500 mM sodium chloride fit by double exponential decay function (black line).

$$N_{surv} = A_1 e^{-t/\tau_{unb1}} + A_2 e^{-t/\tau_{unb2}} \quad [3.6]$$

The best-fit curve of equation 3.6 is plotted as a dashed line in Figure 3.9, with unbinding times of $\tau_{unb1} = 46 \pm 3$ s and $\tau_{unb2} = 7 \pm 1$ s, corresponding to unbinding rates of $k_{unb1} = 2.17 \pm 0.06 \times 10^{-2}$ s^{-1} and $k_{unb2} = 1.4 \pm 0.1 \times 10^{-1}$ s^{-1}. The first time bin of the histogram, 0.5 s, was excluded from the fit to avoid measuring spurious noise, cosmic rays or other false-positive events. Uncertainties were estimated by breaking the total pool of unbinding event measurements into three subpopulations and averaging the rates fit to each subpopulation. From a time-weighted average of the pre-exponential constants, 85 % of the surface population of probe ssDNA unbinds with rate k_{unb1}. We hypothesize that the fast k_{unb2} corresponds to non-specific interactions with the surface, rather than complementary strand hybridization. This is plausible because k_{unb2} closely matches the mean unbinding rate measured for noncomplementary control ssDNA, $k_{unb} = 1.8 \pm 0.1 \times 10^{-1}$ s^{-1}. Control ssDNA has similar base pair content to probe ssDNA, and is expected to have similar nonspecific interactions with the surface. Since the slow unbinding rate, k_{unb1}, dominates the population on the surface, and is unique to the complementary probe, we report this value as k_{unb} for the fully hybridized DNA dissociation. At ionic strengths below 100 mM, the lifetimes of nonspecific interactions were less than the discarded 0.5 s initial time bin, and histograms were fit well by a single-exponential decay term from equation 3.6.

Kinetics measured using a single fluorescent label[17,18] can be influenced by photobleaching, photoblinking, and other photochemical phenomena.[35] Fluorophore photobleaching or formation of long-lived triplet states can mimic actual unbinding events because all result in the disappearance of a fluorescent spot. The impact of

photoblinking and has been reduced by tracking probe ssDNA coordinates for several seconds after apparent unbinding to see if they return, as described above. We measured the influence of photobleaching by determining k_{unb} at varying illumination intensities. Photobleaching rates are typically proportional to illumination power density;[36] if the photobleaching rate is comparable to k_{unb}, the apparent unbinding rate will increase with illumination intensity. Figure 3.10 shows unbinding rates, ~ 2×10^{-2} s^{-1}, for probe ssDNA in 500 mM ionic strength at illumination intensities between 165 and 500 μW. Within the measurement uncertainty, illumination intensity has no impact on k_{unb}, indicating photobleaching is not an issue for k_{unb} greater than 2×10^{-2} s^{-1}. For k_{unb} less than 2×10^{-2} s^{-1}, intermittent imaging with 0.5 s light exposures at 4.0 s intervals was used to reduce light exposure while still sampling long residence times. At 4.0 s intervals, the average excitation intensity was reduced by a factor of 8, allowing unbinding rates up to ~ 2.5×10^{-3} s^{-1} to be reliably measured.

With K_a and k_{unb}, the binding rate constant, k_{bind}, can be calculated for bi-molecular binding using equation 3.7.

$$k_{bind} = K_a k_{unb} \qquad [3.7]$$

From the slope of probe ssDNA accumulation at 500 mM ionic strength in Figure 3.7, $K_a = 1.0 \pm 0.1 \times 10^8$ M^{-1}, and from residence time histograms, $k_{unb} = 2.17 \pm 0.07 \times 10^{-2}$ s^{-1}, which results in $k_{bind} = 2.1 \pm 0.3 \times 10^6$ $M^{-1}s^{-1}$. The binding rate constant is within a factor of 2 of k_{bind} measured in free solution for 10-mer ssDNA using fast mixing and fluorescence resonance energy transfer to measure the dsDNA in solution.[42] In addition, the binding rates from this work match binding rates from

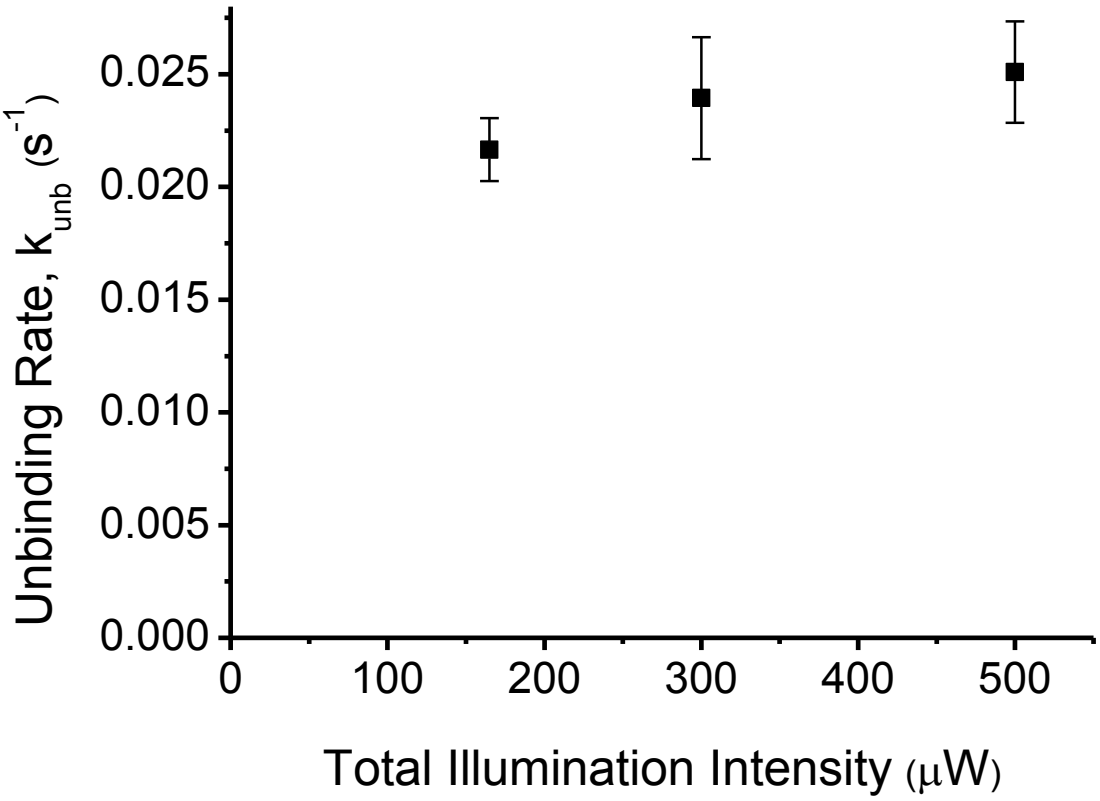

Figure 3.10. Photobleaching analysis: unbinding rates (black squares) for 1.6 pM probe ssDNA, 0.5 mM pH 8 phosphate buffer and 500 mM sodium chloride measured at varying illumination intensity.

Jungman et al.[7] measured for single molecule hybridization between dilute surface-bound target ssDNA and complementary fluorescent 10-mer probes.

In contrast with kinetics measured in free solution and on dilute surfaces, hybridization kinetics measured on high density surfaces, > 10^{13} target molecules cm^{-2}, differ from our results. Association constants are generally slightly lower for high-density techniques; for example Okahata et al.[10] measured a four-fold lower $K_a = 2.4 \times 10^7$ M^{-1}, for 10-mer ssDNA hybridization using QCM at a crowded surface. However, the rate constants that determine K_a differ by even greater factors: binding rates are 10 times[6] to 20 times[10] slower, and k_{unb} is 10 times slower.[10] These rates are likely limited by slow mass transport from dilute solution to occupy a large fraction of densely-packed binding sites. Hybridization may also be hindered at densely packed ssDNA surfaces due to steric and electrostatic repulsion contributing to lower k_{bind} and K_a.[43]

3.3.4 Influence of Ionic Strength on Hybridization

Having developed methods to measure association constants, binding rate constants and unbinding rates, we are able to study the influence of ionic strength on the kinetics and thermodynamics of DNA hybridization. The sugar-phosphate backbone of DNA is highly charged, with up to 0.5 electron equivalents of net excess charge per base pair.[21] As a result, electrostatic repulsion between complementary ssDNA strands creates a kinetic barrier to forming dsDNA, and weakens the dsDNA complex. Electrostatics can be tuned with solution ionic strength; excess ions screen electrical charge and reduce electrostatic repulsion.[9,10] We have investigated this charge-screening mechanism by measuring both K_a and hybridization kinetics with supporting electrolyte ionic strength between 25 and 750 mM. For each ionic strength, equilibrium populations and unbinding

kinetics were measured by injecting a series of target ssDNA concentrations in 0.5 mM pH 8.0 phosphate buffer and excess sodium chloride to establish the ionic strength. A single target ssDNA-modified surface was used for all measurements; after each ionic strength series, the surface was regenerated by denaturing all dsDNA complexes with deionized water for 10 minutes. Association constants were measured from slopes of single molecule accumulation curves and Γ_{max}, and are shown in Figure 3.11a, and summarized in Table 3.1. DNA hybridization is highly sensitive to ionic strength: by increasing ionic strength a factor of 30, *association constants increase over 4000 fold*, from $K_a = 1.0 \pm 0.2 \times 10^5$ to $4.3 \pm 0.6 \times 10^8$ M^{-1}. Binding and unbinding rate constants from molecule survival histograms (see above) were measured over the same range of ionic strength, shown in Figure 3.11b and also summarized in Table 3.1. Both rate constants contribute significantly to increasing K_a, k_{unb} decreases by a factor of 30, and k_{bind} increases by a factor of 100.

The Debye length, κ^{-1},[44,45] is a measure of the distance scale of electrostatic interactions in electrolyte solutions. The Debye length of a 1:1 electrolyte is a function of the bulk electrolyte concentration, C^0, the ion charge, z, the elementary charge, e, the electrical permittivity of a vacuum, ε_0, the relative permittivity, ε, Boltzmann's constant, k_B, and the solution temperature, T:

$$\kappa^{-1} = \left(\frac{\varepsilon\varepsilon_0 k_B T}{2C^0 z^2 e^2}\right)^{1/2} \qquad 3.8$$

Below 100 mM ionic strength, the Debye lengths is greater than the radius of dsDNA, ~1.2 nm, meaning electrostatic repulsion between complementary ssDNA influences both k_{bind} and k_{unb}. Binding rates slow because electrostatic repulsion hinders probe and target

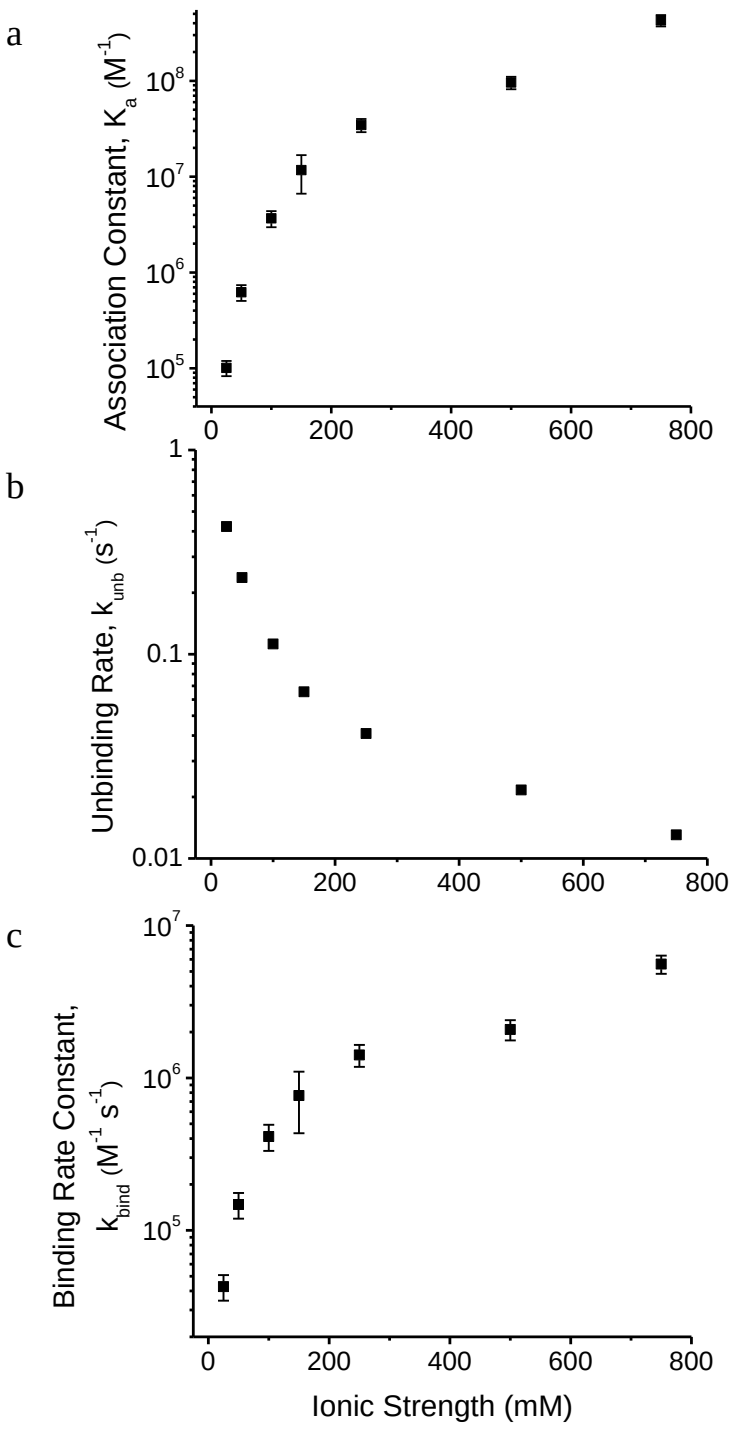

Figure 3.11. Ionic strength dependence of association rates, dissociation rates, and the affinity constant. a) Association constant for probe ssDNA in 0.5 mM pH 8 phosphate buffer and varying ionic strength, b) unbinding rates measured from survival time histograms, error bars are too small to be visible, and c) binding rate constants, from Equation 6. Error bars are 2 standard deviations of the mean.

Table 3.1

Thermodynamic and Rate Constants for DNA Hybridization at Ionic Strength from 25 to 750 mM

Ionic Strength (mM)	Association Constant, K_a ($M^{-1} \times 10^{-6}$)	Hybridization Rate, k_{bind} ($M^{-1}\ s^{-1} \times 10^{-6}$)	Unbinding Rate, k_{unb} ($M^{-1}\ s^{-1} \times 10^{-1}$)	Total Free Hybridization Energy, $\Delta G°$ (kJ mol^{-1})	Electrostatic Hybridization Free Energy, $\Delta G°_{es}$ (kJ mol^{-1})	Total Hybridization Activation Energy, $\Delta G^{‡}$ (kJ mol^{-1})	Electrostatic Hybridization Activation Energy, $G^{‡}_{es}$ (kJ mol^{-1})	Total Unbinding Activation Energy, $\Delta G^{‡'}$ (kJ mol^{-1})	Electrostatic Unbinding Activation Energy, $\Delta G^{‡'}_{es}$ (kJ mol^{-1})
25	0.10 ± 0.02	0.043 ± 0.008	4.2 ± 0.3	-28.4 ± 0.5	20 ± 3	46.2 ± 0.5	11.8 ± 0.9	74.6 ± 0.2	-8 ± 1
50	0.62 ± 0.1	0.15 ± 0.03	2.4 ± 0.1	-32.8 ± 0.5	15 ± 3	43.2 ± 0.5	8.7 ± 0.9	76.0 ± 0.1	-7 ± 1
100	3.7 ± 0.7	0.41 ±0 .08	1.12 ± 0.04	-37.2 ± 0.5	11 ± 3	40.7 ± 0.5	6.2 ± 0.9	77.9 ± 0.1	-5± 1
150	12 ± 5	0.77 ± 0.3	0.66 ± 0.02	-40 ± 1	8 ± 4	39 ± 1	5 ± 1	79.2 ± 0.1	-4 ± 1
250	35 ± 5	1.4 ±0 .2	0.41 ± 0.02	-42.7 ± 0.4	6 ± 2	37.6 ± 0.4	3.2 ± 0.9	80.3 ± 0.1	-3 ± 1
500	96 ± 10	2.1 ± 0.3	0.217 ± 0.006	-45.2 ± 0.4	3 ± 2	36.7 ± 0.4	2.2 ± 0.9	81.9 ± 0.1	-1 ± 1
750	430 ± 60	5.6 ± 0.8	0.130 ± 0.002	-48.9 ± 0.3	0 ± 3	34.2 ± 0.3	0 ± 0.8	83.2 ± 0.1	0 ± 1

Uncertainties are reported to 2 standard deviations of the mean.

ssDNA from approaching close enough to undergo base-pair hydrogen bonding, increasing the activation energy to binding. Unbinding rates increase because electrostatic repulsion destabilizes the double strand, reducing the depth of the bound duplex energy well, thus reducing the kinetic barrier to dissociation. At ionic strengths between 250 mM to 750 mM, κ^{-1} is a fraction of the radius of dsDNA, and we see diminished influence on rates from electrolyte ion screening.

Hybridization rate constants have been used to estimate the activation energy of dsDNA-complex formation, $\Delta G^{\ddagger}$, which can help describe mechanisms of hybridization. Rate constants, are related to $\Delta G^{\ddagger}$ through the Eyring equation, k_B is Boltzmann's constant, T is temperature, h is Planck's constant, and assuming the transmission coefficient and standard concentration are unity:

$$k = \frac{k_B T}{h} e^{\frac{-\Delta G^{\ddagger}}{RT}} \qquad 3.9$$

From the linearized form of the Eyring equation the activation energy can be determined from the slope of a plot of $\ln(k_{bind})$ versus T^{-1}:

$$\ln(k) = \ln\left(\frac{k_B T}{h}\right) - \frac{\Delta G^{\ddagger}}{RT} \qquad 3.10$$

Changing temperature affects hybridization association rates, and activation energies have been determined from the temperature-dependent binding of short oligonucleotides.[6,42,46] As our data show, ionic strength has a large impact on hybridization rate constants and is expected to have a significant impact on association activation energies.

To describe the contribution of ionic strength to hybridization activation energy, we have developed a simple model to map the potential energy landscape of the DNA hybridization process, shown in Figure 3.12. We begin by describing the binding process, by relating the binding rate constant to the activation energy for binding, $\Delta G^{\ddagger}$. In this model, the binding activation energy is represented as a sum of electrostatic, $\Delta G^{\ddagger}_{es}$, and nonelectrostatic, $\Delta G^{\ddagger}_{nes}$, components as shown in equation 3.11.

$$\Delta G^{\ddagger} = \Delta G^{\ddagger}_{es} + \Delta G^{\ddagger}_{nes} \quad 3.11$$

By combining this description of $\Delta G^{\ddagger}$ with equation 3.10, we get a new expression for $\ln(k_{bind})$:

$$\ln(k_{bind}) = \ln\left(\frac{k_B T}{h\kappa C^0}\right) - \frac{\Delta G^{\ddagger}_{nes}}{RT} - \frac{\Delta G^{\ddagger}_{es}}{RT} \quad 3.12$$

Electrostatic interactions are screened by ions in solution, so $\Delta G^{\ddagger}_{es}$ is expected to vary with ionic strength, while $\Delta G^{\ddagger}_{nes}$ represents all nonelectrostatic contributions to the activation energy, such as solvation interactions, steric hindrance, etc., which are assumed to be much less sensitive to ionic strength. To describe $\Delta G^{\ddagger}_{es}$, a simple Poisson-Boltzmann model is proposed to represent the potential energy of a probe ssDNA ion in an electrical potential field near a target ssDNA surface. In this electrostatic activation energy model, the effective electrical charge of the portion of the probe ssDNA participating in the transition state is represented by z_{ts}, in elementary charge equivalents. The electrical potential energy of the interaction between probe and target ssDNA in the transition state is proportional to the product of z_{ts} and the potential near the target ssDNA surface. The zeta potential, ζ_{target}, provides an estimate of surface electrical

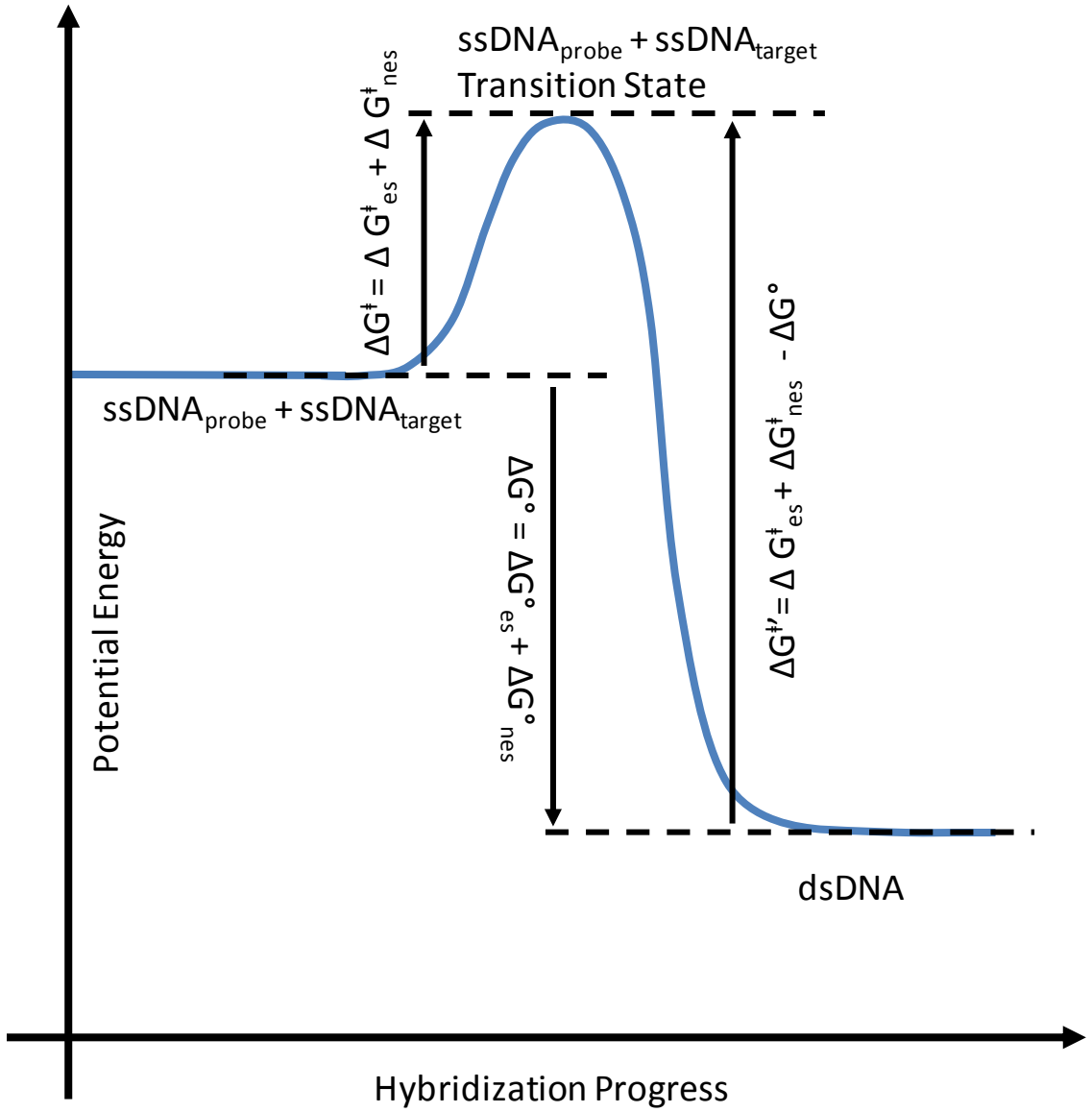

Figure 3.12. Diagram of DNA hybridization transition state model.

potential along the target ssDNA sugar-phosphate backbone, as it represents the potential at the solvent "slip plane" within a few angstroms of the surface.[47] The zeta potential of DNA has been determined from electrophoretic mobility measurements, and is ~50 mV for 250 mM sodium chloride solutions.[48] In our model, we assume that the transition state is structurally similar to a double helix, so that the shortest distance between ssDNA charged backbones is 1.2 nm in the helical minor groove, which is larger than the distance to the slip-plane region. This assumption is reasonable, because molecular dynamics simulations indicate that single strands are in close contact during the hybridization transition state, and that base-pair repeats, such as the "GGG" repeat in the probe ssDNA, act as nucleation sites for hybridization.[49] Beyond the slip plane, diffusing electrolyte ions screen the zeta potential according to Gouy-Chapman theory, where potential, φ, as a function of distance from the DNA backbone, x, is represented with an exponential decay function:

$$\varphi = \zeta_{\text{target}} e^{-\kappa x} \qquad 3.13$$

The electrical potential experienced by the probe in the bound duplex is set to φ_{es}, the potential evaluated at the distance between phosphate groups in the dsDNA minor groove, x = 1.2 nm. Since φ decays exponentially with distance, the other distances between ssDNA backbones in the double helix, the 2.4 nm double-helix diameter and 2.2 nm major groove thickness, contribute little to the total potential. We have found that increasing x from 1.0 and 2.4 nm results in larger z_{ts} by ~50%, while otherwise having little impact on the trends in electrostatic potential described by this model. The final expression for the magnitude of $\Delta G^{\ddagger}_{es}$ is the product of probe ssDNA charge, z_{ts}, the

electrostatic potential at the transition state, φ_{es}, the elementary charge, e, and Avogadro's number, N_A:

$$\Delta G^{\ddagger}_{es} = z_{ts} e \varphi_{es} N_A \quad 3.14$$

Combining the Eyring relation in equation 3.12, with the expression for the electrostatic activation energy, equation 3.14, provides an expression for $\ln(k_{bind})$ based on a Gouy-Chapman potential decay model:

$$\ln(k_{bind}) = \ln\left(\frac{k_B T}{h \kappa C^0}\right) - \frac{\Delta G^{\ddagger}_{nes}}{RT} - \frac{z_{ts} e \varphi_{es} N_A}{RT} \quad 3.15$$

For each ionic strength studied, φ_{es} was calculated using the parameters described above with x = 1.2 nm, ζ_{target} = 50 mV, using equations 3.8, and equation 3.13. Finally, by plotting ln(k) versus φ_{es}, we can estimate $\Delta G^{\ddagger}_{nes}$, $\Delta G^{\ddagger}_{es}$, and z_{ts} from the slope and intercept of a linear fit to equation 3.15.

Values of $\ln(k_{bind})$ versus φ_{es} and a linear least squares fit of equation 3.15 are shown in Figure 3.13a. From the intercept of the plot, $\Delta G^{\ddagger}_{nes}$ = 34.4 ± 0.8 kJ mol^{-1}. The electrostatic portion of the activation energy was calculated from the intercept of the fitted line, $\Delta G^{\ddagger}_{es} = -RT[\ \ln(k_{bind}) + \Delta G^{\ddagger}_{nes} - \ln(k_B T/h)\ ]$ and is plotted against ionic strength in Figure 3.13b. As expected, $\Delta G^{\ddagger}_{es}$ decreases with ionic strength and has essentially no contribution to the activation energy at 750 mM ionic strength. In addition, $\Delta G^{\ddagger}_{nes}$ exceeds $\Delta G^{\ddagger}_{es}$ even at low ionic strength, indicating that electrostatics are not the primary free energy barrier to hybridization for ionic strengths in this range. The total activation energy for hybridization, $\Delta G^{\ddagger}$ = 38 ± 1 kJ/mol is comparable with previously

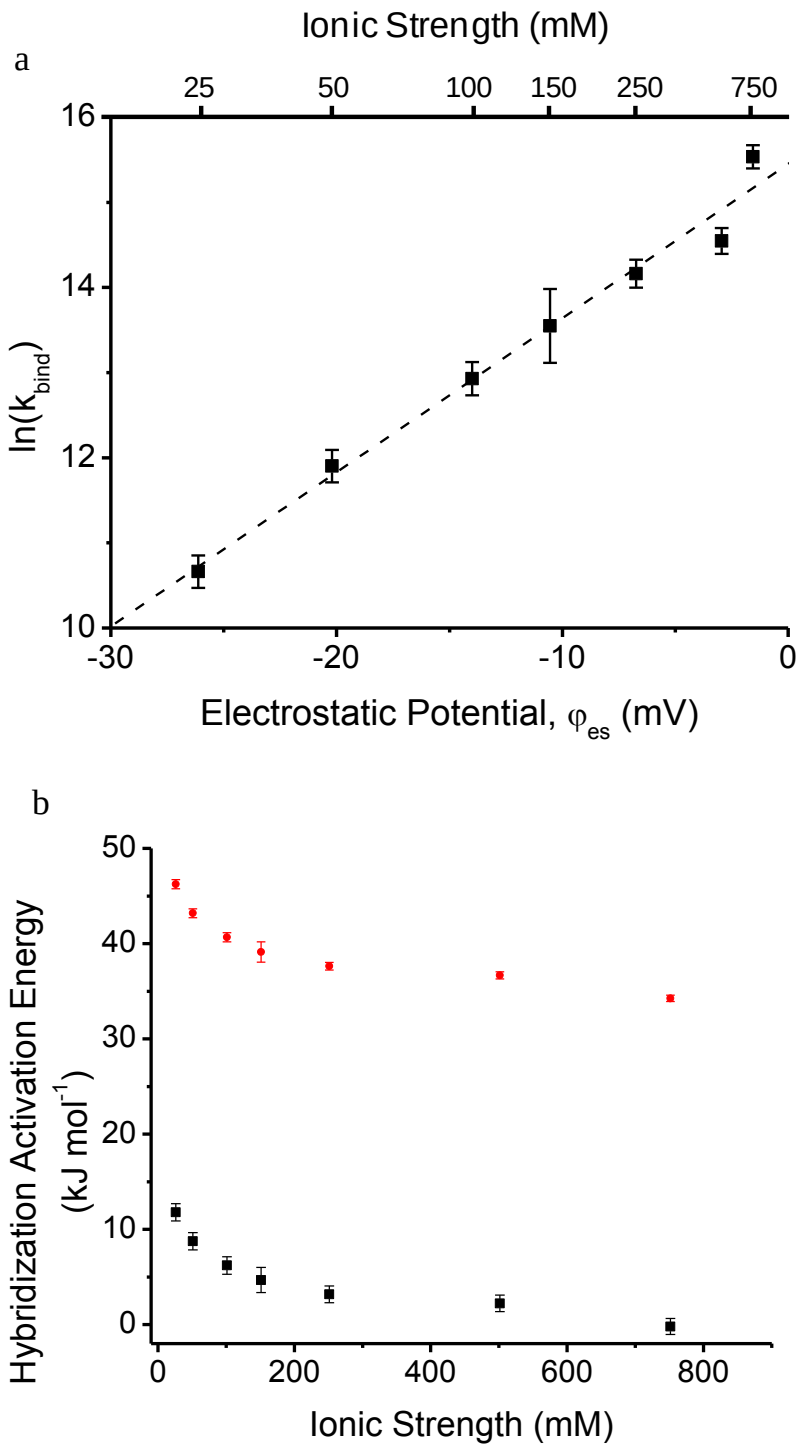

Figure 3.13. Electrostatic contribution to hybridization activation energy, a) plot of $\ln(k_{bind})$ versus bound complex potential to determine activation energies, b) total activation energy for binding, $\Delta G^{\ddagger}$, (red) and electrostatic component of activation energy, $\Delta G^{\ddagger}_{es}$, (black) for hybridization

reported values: 42 ± 13 kJ/mol for 20-mer hybridization on gold nanoparticles,[6] and 42 ± 4 kJ/mol for 10-mer hybridization in bulk solution.[42]

The activation energy for the unbinding process presents a larger energy barrier than in the binding process, because the total free energy of the bound duplex relative to free ssDNA has been lowered by $\Delta G° = -RT\ln(K_a)$. In order to form the transition state, the dsDNA must overcome an unbinding activation energy barrier, $\Delta G^{‡\prime}$, equal to the difference between $\Delta G^{‡}$ and $\Delta G°$:

$$\Delta G^{‡\prime} = \Delta G^{‡} - \Delta G° \tag{3.16}$$

The unbinding activation energy can also be described in terms of electrostatic, $\Delta G^{‡\prime}_{es}$ and nonelectrostatic, $\Delta G^{‡\prime}_{nes}$, components:

$$\Delta G^{‡\prime}_{es} = \Delta G^{‡}_{es} - \Delta G°_{es} \tag{3.17}$$

$$\Delta G^{‡\prime}_{nes} = \Delta G^{‡}_{nes} - \Delta G°_{nes} \tag{3.18}$$

$$\Delta G^{‡\prime} = \Delta G^{‡}_{es} + \Delta G^{‡}_{nes} - (\Delta G°_{nes} + \Delta G°_{es}) \tag{3.19}$$

These expressions can be combined with equation 3.10 to describe the relationship between the unbinding rate and the thermodynamic quantities:

$$\ln(k_{unb}) = \left[\ln\left(\frac{k_B T}{h\kappa C^0}\right) - \frac{\Delta G^{‡}_{nes}}{RT} + \frac{\Delta G°_{nes}}{RT}\right] - \frac{\Delta G^{‡}_{es}}{RT} + \frac{\Delta G°_{es}}{RT} \tag{3.20}$$

The same Gouy-Chapman potential decay model used to describe $\Delta G^{‡}_{es}$ was used to describe $\Delta G°_{es}$, since we assume the bound duplex has a similar DNA backbone spacing

and potential profile. A different value for the charge of the probe strand, z_{bound}, is fit by this function, since there may to be more charged groups interacting in the fully bound duplex than in the transition state. The expression for $\Delta G°_{es}$ is now:

$$\Delta G°_{es} = z_{bound} e \varphi_{es} N_A \qquad 3.21$$

By substituting equation 3.21 into 3.20, we get a new expression describing the unbinding activation energy:

$$\ln(k_{unb}) + \frac{\Delta G^{‡}_{es}}{RT} = \left[\ln\left(\frac{k_B T}{h \kappa C^0}\right) - \frac{\Delta G^{‡}_{nes}}{RT} + \frac{\Delta G°_{nes}}{RT}\right] + \frac{z_{bound} e \varphi_{es} N_A}{RT} \qquad 3.22$$

Values for $\Delta G^{‡}_{es}$, and $\Delta G°_{nes}$ in equation 3.22 are already known from the binding-rate Eyring plot, Figure 3.13a. By plotting $\ln(k_{unb}) + \Delta G^{‡}_{es}/RT$ versus φ_{es}, the slope and intercept from a fit to equation 3.22 will provide $\Delta G°_{nes}$, $\Delta G°_{es}$, and z_{bound}, as shown in Figure 3.14a. In addition, $\Delta G^{‡'}_{es}$ and $\Delta G^{‡'}_{nes}$ can be calculated from equations 3.17 and 3.18. All of these thermodynamic quantities are listed in Table 3.1. The nonelectrostatic free energy of hybridization, $\Delta G°_{nes}$ = -49 ± 2 kJ mol^{-1}, is similar to the total free energy of hybridization at 750 mM ionic strength, -48.9 ± 0.3, indicating that nearly all electrostatic effects on hybridization are gone at high ionic strength. The electrostatic contribution to the free energy of hybridization, $\Delta G°_{es}$ has been plotted in Figure 3.15. As this plot shows, $\Delta G°_{es}$ reduces $\Delta G°$ by a factor of 2 at low ionic strength, but has little contribution to $\Delta G°$ at high ionic strength.

The total the unbinding activation energy, $\Delta G^{‡'}$, plotted in Figure 3.14b, shows less sensitivity to ionic strength than $\Delta G^{‡}$ for binding, because the higher ionic strength stabilizes the dsDNA bound duplex while it also lowers the transition state energy of the

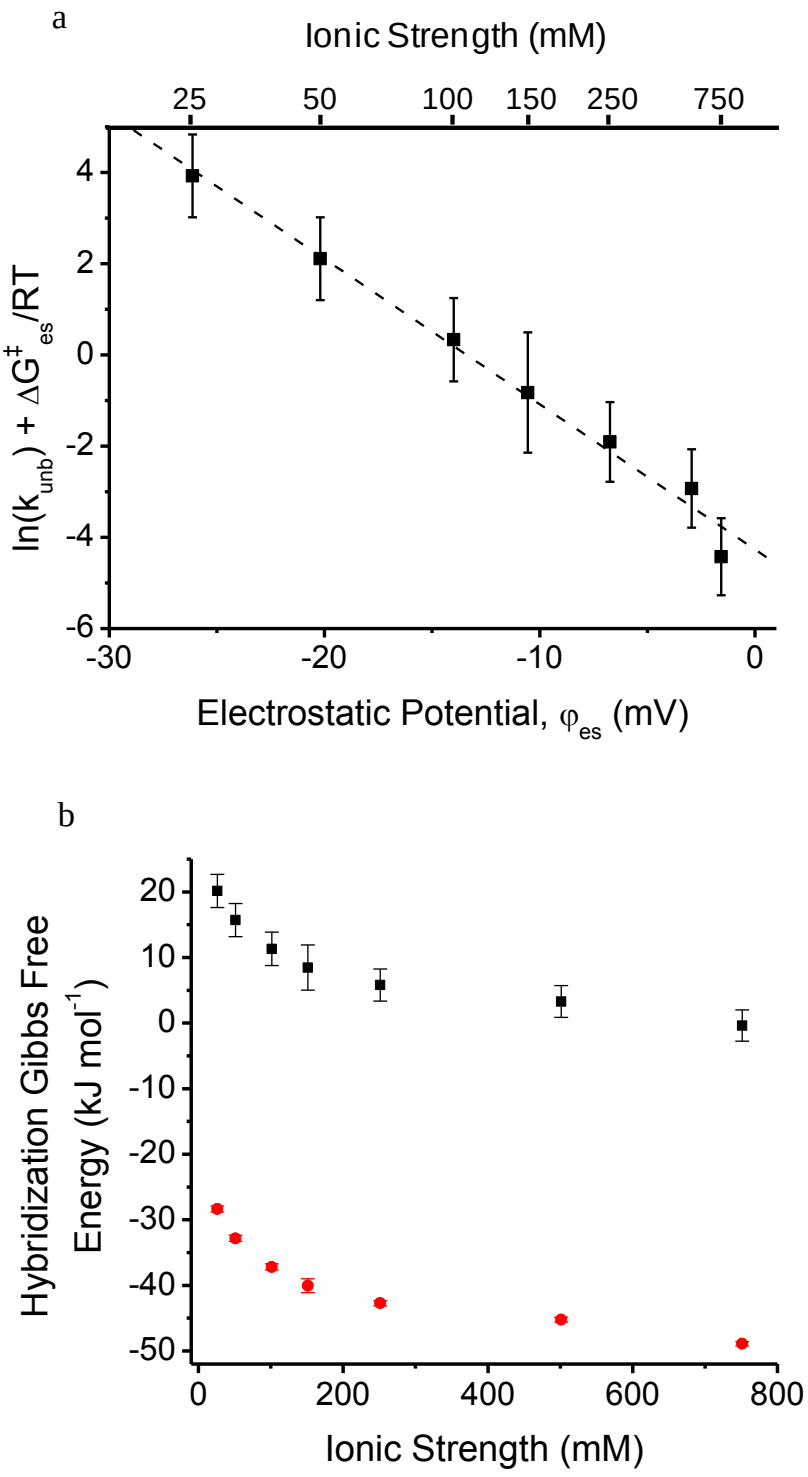

Figure 3.14. Electrostatic contribution to total Gibbs free energy of hybridization, a) plot of $\ln(k_{unb}) + \Delta G^{\ddagger}_{es}$ versus bound complex potential to determine activation energies for unbinding, b) total free energy of hybridization, $\Delta G°$ (red) and electrostatic component of the free energy, $\Delta G°_{es}$ (black)

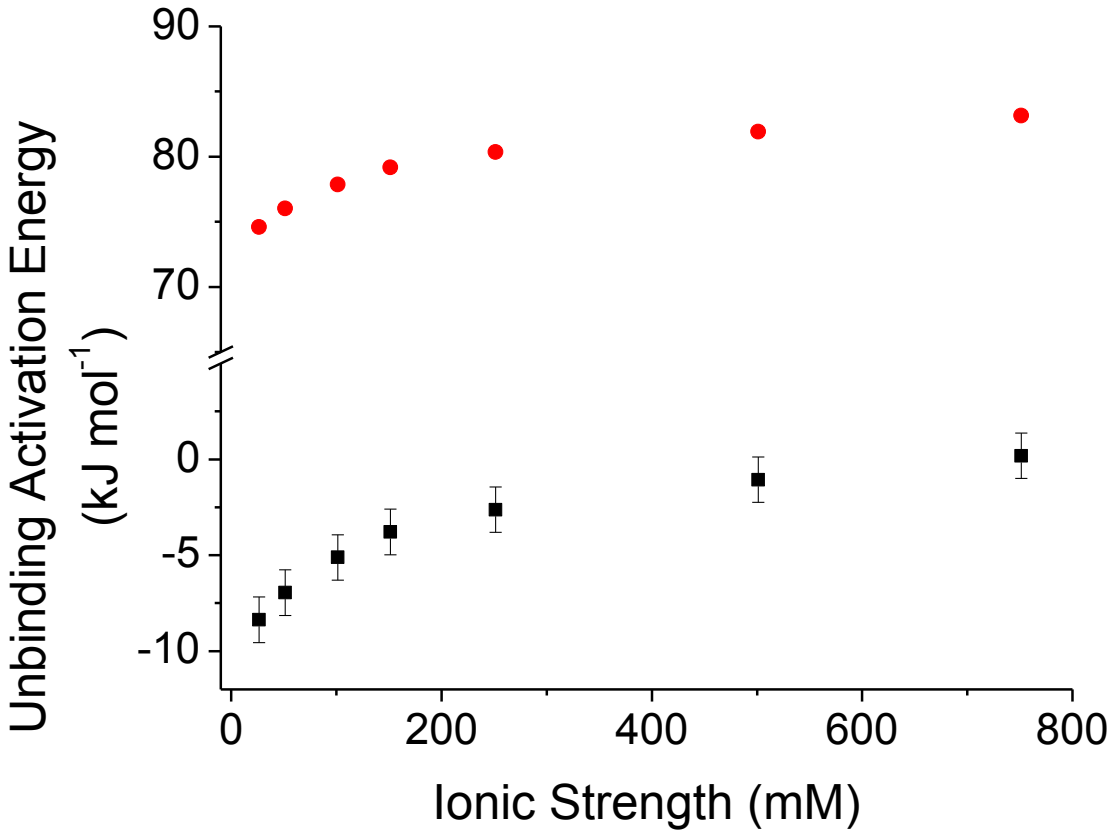

Figure 3.15. Total activation energy for unbinding, $\Delta G^{\ddagger\prime}$, (red) and electrostatic component of unbinding activation energy, $\Delta G^{\ddagger\prime}_{es}$, (black)

electrostatic barrier, $\Delta G^{\ddagger}_{es}$. The net result is that higher ionic strength actually raises the energy barrier to dissociation. Because $\Delta G^{\ddagger\prime}_{es} = \Delta G^{\ddagger}_{es} - \Delta G^{\circ}_{es}$, the increase in $\Delta G^{\ddagger\prime}$ at higher ionic strength is the result of the free energy of the dissociating dsDNA complex, $-\Delta G^{\circ}_{es}$, increasing more than the energy of the transition state, $\Delta G^{\ddagger}_{es}$, is lowered with ionic strength.

The magnitudes of effective charge of the probe ssDNA determined from equations 3.14 and 3.18 provide a clue as to the mechanism of the differing ionic strength dependence on k_{bind} and k_{unb}. The charge at the transition state, $z_{ts} \sim -5$, is less than the charge of the bound duplex, $z_{bound} \sim -8$, indicating that there is considerably more electrostatic repulsion in the fully bound dsDNA complex than at the transition state. This result could describe the mechanism of hybridization: at the transition state, there appear to be fewer bases interacting than in the fully bound duplex. This suggests that hybridization is not an all-or-nothing binding event between all the oligonucleotide bases; rather, only a fraction of the bases are needed to initiate binding, and the double strand forms quickly after reaching this transition state. Another contribution to the differing charges is that counterions associated with ssDNA may be lost during the hybridization process. It is known that sodium ions interact with charged phosphate groups and reduce the net charge on DNA,[21] and it is possible that some of these adsorbed cations are shed during hybridization, resulting in greater net charge on the bound complex versus the transition state.

Other phenomenon, beyond what our simple model can reveal, may also influence the ionic strength dependence of hybridization. Specific ion adsorption to DNA[21] may cause the electrostatics to deviate from the simple Gouy-Chapman model. Ionic strength

also influences DNA structure, such as the persistence length of ssDNA,[50] which may influence hybridization rates. Single stranded DNA persistence length decreases from eight base pairs to a baseline distance of two base pairs from 25 to 150 mM ionic strength. This change in structural flexibility could influence the ability of probe ssDNA to explore conformational space and form base-pair matches with target ssDNA. Nevertheless, the simple Gouy-Chapman model is consistent with the ionic strength dependence of the measured binding and unbinding rates and reveals trends in the electrostatic contributions to kinetic barriers to DNA hybridization and the instability of double-stranded DNA complexes.

3.4 Summary

We have successfully measured association constants and kinetic rate constants for complementary strand hybridization between fluorescently labeled probe and surface-bound target ssDNA. Association constants, K_a, were determined by counting surface-bound probe dsDNA complexes versus solution concentration, and fitting results to a Langmuir model. The total target ssDNA surface density was needed for this analysis, and it was measured by means of a combined single molecule counting-fluorescence intensity binding assay. Double stranded DNA dissociation rates, k_{unb}, were determined by measuring residence times of individual probe DNA molecules on the surface. Hybridization rates were calculated from a two-state binding model, where $k_{bind} = K_a k_{unb}$, and association constants and rates of hybridization were determined at varying ionic strengths. Upon increasing ionic strength from 25 to 750 mM, K_a increased from $1.0 \pm 0.2 \times 10^5$ M^{-1} to $4.3 \pm 0.6 \times 10^8$ M^{-1}, a factor of 3000. The increase in K_a derived from increases in k_{bind} was a factor of 100 and the decrease from k_{unb} was a factor of 30.

Changes in binding and unbinding constants with ionic strength were modeled with Eyring transition-state theory to determine electrostatic and non-electrostatic contributions to the free energies of the transition state and hybridized dsDNA duplex. Charge repulsion between probe and target ssDNA were modeled with the zeta potential of DNA and a potential drop across the electrical double-layer according to Gouy-Chapman theory. The electrostatic free energy of the transition state, $\Delta G^{\ddagger}_{es}$, decreased from 11.8 ± 0.9 to 0 ± 0.8 kJ mol^{-1} upon increasing the ionic strength from 25 to 750 mM, respectively. The electrostatic free energy of the bound duplex, ΔG°_{es}, was positive at low ionic strengths, indicating that electrostatic repulsion destabilized the dsDNA complex. Upon increasing the ionic strength from 25 to 750 mM, ΔG°_{es} decreased from 20 ± 3 to 0 ± 3 kJ mol^{-1} respectively, indicating that electrostatic repulsion was completely screened by counterions at 750 mM ionic strength. The net electrostatic free energy of the disassociation transition state, $\Delta G^{\ddagger\prime}_{es}$, increased with increasing ionic strength, from -8 ± 1 to 0 ± 1 kJ mol^{-1}, because the electrostatic repulsion contributing to the free energy of the bound duplex, $-\Delta G^{\circ}_{es}$, decreased more with higher ionic strength than $\Delta G^{\ddagger}_{es}$. The larger total increase in $\Delta G^{\ddagger}_{es}$ compared to $\Delta G^{\ddagger\prime}_{es}$ with increasing ionic strength explains the larger ionic strength dependence of k_{bind} compared to k_{unb}. Finally, the electrical charge of the hybridized bound duplex, ~8 electron equivalents, was greater than the charge of the transition state, ~5 electron equivalents, indicating that the transition state consists of fewer interacting base pairs than the fully bound DNA duplex.

In future work, we will investigate the influence of sequence, base pair content, and strand length on the electrostatic contribution to the thermodynamics of DNA hybridization. In addition, the high dynamic range in association constants and kinetic

rates, and low detection limit, 15 fM, make this assay capable of characterizing other oligonucleotide-based single molecule interactions, such as aptamer-ligand[16] and peptide nucleic acid binding.[41] Furthermore, the DNA-modified glass slides developed in this work could be used to immobilize other biomolecules, such as DNA, RNA or peptides, in order to perform similar binding experiments. Hybridization to immobilized target ssDNA can be used to capture biomolecules which are covalently linked to complementary probe ssDNA. By using longer strands (>20 bp), the DNA duplex formed would be long-lived, while still allowing facile removal of the immobilized species by melting the duplex with elevated temperature.

3.5 References

(1) Human Genome Sequencing, C. *Nature* **2004**, *431*, 931.

(2) Dalma-Weiszhausz, D. D.; Warrington, J.; Tanimoto, E. Y.; Miyada, C. G. In *Methods in Enzymology*; Alan, K., Brian, O., Eds.; Academic Press: 2006; Vol. Volume 410, p 3.

(3) Williams, L.; Blair, S.; Chagovetz, A.; Fish, D. J.; Benight, A. S. *Analytical Biochemistry* **2011**, *409*, 150.

(4) Stagni, C.; Guiducci, C.; Benini, L.; Ricco, B.; Carrara, S.; Paulus, C.; Schienle, M.; Thewes, R. *Sensors Journal, IEEE* **2007**, *7*, 577.

(5) Fritz, J.; Cooper, E. B.; Gaudet, S.; Sorger, P. K.; Manalis, S. R. *Proceedings of the National Academy of Sciences* **2002**, *99*, 14142.

(6) Chen, C.; Wang, W.; Ge, J.; Zhao, X. S. *Nucleic Acids Research* **2009**, *37*, 3756.

(7) Jungmann, R.; Steinhauer, C.; Scheible, M.; Kuzyk, A.; Tinnefeld, P.; Simmel, F. C. *Nano Letters* **2010**, *10*, 4756.

(8) Pörschke, D.; Uhlenbeck, O. C.; Martin, F. H. *Biopolymers* **1973**, *12*, 1313.

(9) Quartin, R. S.; Wetmur, J. G. *Biochemistry* **1989**, *28*, 1040.

(10) Okahata, Y.; Kawase, M.; Niikura, K.; Ohtake, F.; Furusawa, H.; Ebara, Y. *Analytical Chemistry* **1998**, *70*, 1288.

(11) Kang, S. H.; Kim, Y. J.; Yeung, E. S. *Analytical and bioanalytical chemistry* **2007**, *387*, 2663.

(12) Haeussling, L.; Ringsdorf, H.; Schmitt, F. J.; Knoll, W. *Langmuir* **1991**, *7*, 1837.

(13) Altschuh, D.; Dubs, M. C.; Weiss, E.; Zeder-Lutz, G.; Van Regenmortel, M. H. V. *Biochemistry* **1992**, *31*, 6298.

(14) Attavar, S.; Diwekar, M.; Blair, S. *Lab on a Chip* **2011**, *11*, 841.

(15) Axelrod, D. *Methods in Cell Biology* **1989**, *30*, 245.

(16) Elenko, M. P.; Szostak, J. W.; van Oijen, A. M. *Journal of the American Chemical Society* **2009**, *131*, 9866.

(17) Wayment, J. R.; Harris, J. M. *Analytical Chemistry* **2009**, *81*, 336.

(18) Fox, C. B.; Wayment, J. R.; Myers, G. A.; Endicott, S. K.; Harris, J. M. *Analytical Chemistry* **2009**, *81*, 5130.

(19) Tornøe, C. W.; Christensen, C.; Meldal, M. *The Journal of Organic Chemistry* **2002**, *67*, 3057.

(20) Rostovtsev, V. V.; Green, L. G.; Fokin, V. V.; Sharpless, K. B. *Angewandte Chemie International Edition* **2002**, *41*, 2596.

(21) Schellman, J. A.; Stigter, D. *Biopolymers* **1977**, *16*, 1415.

(22) Tataurov, A. V.; You, Y.; Owczarzy, R. *Biophysical Chemistry* **2008**, *133*, 66.

(23) Wayment, J. R.; Harris, J. M. *Analytical Chemistry* **2006**, *78*, 7841.

(24) Balachander, N.; Sukenik, C. N. *Langmuir* **1990**, *6*, 1621.

(25) Lummerstorfer, T.; Hoffmann, H. *The Journal of Physical Chemistry B* **2004**, *108*, 3963.

(26) Prakash, S.; Long, T. M.; Selby, J. C.; Moore, J. S.; Shannon, M. A. *Analytical Chemistry* **2006**, *79*, 1661.

(27) Kolb, H. C.; Finn, M. G.; Sharpless, K. B. *Angewandte Chemie International Edition* **2001**, *40*, 2004.

(28) Devaraj, N. K.; Miller, G. P.; Ebina, W.; Kakaradov, B.; Collman, J. P.; Kool, E. T.; Chidsey, C. E. D. *Journal of the American Chemical Society* **2005**, *127*, 8600.

(29) Chan, T. R.; Hilgraf, R.; Sharpless, K. B.; Fokin, V. V. *Organic Letters* **2004**, *6*, 2853.

(30) Chiou, S.-H. *Journal of Biochemistry* **1983**, *94*, 1259.

(31) Mortara, L.; Fowler, A. *Proc. SPIE* **1981**, *290*, 28.

(32) Robbins, M. S.; Hadwen, B. J. *Electron Devices, IEEE Transactions on* **2003**, *50*, 1227.

(33) Peterson, E. M.; Harris, J. M. *Analytical Chemistry* **2010**, *82*, 189.

(34) Hanley, D. C.; Harris, J. M. *Analytical Chemistry* **2001**, *73*, 5030.

(35) Moerner, W. E. *Science* **1997**, *277*, 1059.

(36) Zondervan, R.; Kulzer, F.; Orlinskii, S. B.; Orrit, M. *The Journal of Physical Chemistry A* **2003**, *107*, 6770.

(37) Asanov, A. N.; Wilson, W. W.; Oldham, P. B. *Analytical Chemistry* **1998**, *70*, 1156.

(38) Herron, J. N.; Caldwell, K. D.; Christensen, D. A.; Dyer, S.; Hlady, V.; Huang, P.; Janatova, V.; Wang, H. K.; Wei, A. P.; 1 ed.; Lakowicz, J. R., Thompson, R. B., Eds.; SPIE: Los Angeles, CA, USA, 1993; Vol. 1885, p 28.

(39) Smith, K. A.; Conboy, J. C. *Biochimica et Biophysica Acta (BBA) - Biomembranes* **2011**, *1808*, 1611.

(40) Lee, J.-Y.; Li, J.; Yeung, E. S. *Analytical Chemistry* **2007**, *79*, 8083.

(41) Uno, T.; Tabata, H.; Kawai, T. *Analytical Chemistry* **2006**, *79*, 52.

(42) Morrison, L. E.; Stols, L. M. *Biochemistry* **1993**, *32*, 3095.

(43) Watterson, J. H.; Piunno, P. A. E.; Wust, C. C.; Krull, U. J. *Langmuir* **2000**, *16*, 4984.

(44) Gouy, L. G. *J. Phys.* **1910**, *4*.

(45) Chapman, D. L. *Phil. Mag.* **1913**, *6*, 475.

(46) Wei, F.; Qu, P.; Zhai, L.; Chen, C.; Wang, H.; Zhao, X. S. *Langmuir* **2006**, *22*, 6280.

(47) Lyklema, J.; Rovillard, S.; De Coninck, J. *Langmuir* **1998**, *14*, 5659.

(48) Ross, P. D.; Scruggs, R. L. **1964**, *2*, 231.

(49) Sambriski, E. J.; Schwartz, D. C.; de Pablo, J. J. *Proceedings of the National Academy of Sciences* **2009**, *106*, 18125.

(50) Tinland, B.; Pluen, A.; Sturm, J.; Weill, G. *Macromolecules* **1997**, *30*, 5763.

CHAPTER 4

SINGLE MOLECULE FLUORESCENCE IMAGING OF DNA AT AN ELECTRICAL POTENTIAL-CONTROLLED INTERFACE

4.1 Introduction

Interactions of charged surfaces with polyelectrolytes and charged particles are important in numerous fields, such as environmental science, e.g. humic acid adsorption to metal oxide surfaces,[1-4] solar energy, e.g. assembly of polyelectrolytes as components of solar cells,[5,6] and bioanalytical techniques, such as surface plasmon resonance (SPR),[7-9] and total internal reflection fluorescence binding assays.[10-12] Polyelectrolytes may feature hydrophobic, steric, and electrostatic interactions with surfaces.[13] Because large polyelectrolytes, such as DNA, peptides or humic acids, can have thousands to millions of charged surface groups, electrostatic interactions with surfaces are expected to be significant. A quantitative understanding of these electrostatic interactions will help describe the affinity of polyelectrolytes for charged surfaces, such as humic acid surface binding,[14,15] or nonspecific interactions in bioanalytical techniques.[16,17]

To investigate potential-dependent behavior of individual polyelectrolyte molecules in the thin electrical double-layer region near a charged surface, an interface-sensitive detection scheme with ultra-low detection limits is needed. Total internal reflection fluorescence (TIRF) microscopy[18] allows imaging of fluorescent molecules in a

thin (≈ 150 nm thick) surface region illuminated by an evanescent field from light internally reflected at the interface. Single molecule fluorescence imaging is a powerful tool for measuring biophysical interactions at solid-liquid interfaces, such as biomolecule-ligand binding kinetics,[19,20] biomolecule-surface binding and interactions,[21,22] and protein-protein interactions.[23] Single molecule imaging has several advantages over bulk techniques for probing chemistry at interfaces. Single molecule techniques have low detection limits, 10-100 yoctomol,[24,25] which are ideal for observing populations of dilute molecules (pM to nM) in the interfacial region. Interfacial populations and concentrations can be directly determined by counting molecules in images where no intensity calibration is needed.[25] Interfacial diffusion can be directly determined on a per-molecule basis by tracking the positions of molecules versus time.[22,26-29] Probing individual molecules also reveals sample heterogeneity that would be lost in bulk techniques which report an ensemble average of molecular behavior.[30,31]

The imaging of individual, fluorescently labeled DNA at liquid-solid interfaces was pioneered by Yeung, Porter, and co-workers who have investigated the interfacial behavior of DNA at self-assembled monolayers on gold,[32,33] at bare glass,[34,35] and at transparent carbon electrodes.[36] At the carbon electrode surface, reversible increases in the interfacial DNA population could be observed under the influence a positive applied potential, showing the utility of this methodology to investigate interfacial electrolyte populations of under potential control. Fluorescence experiments performed near thick (opaque) gold metal electrodes have successfully probed the influence of the electrical double-layer on the orientation and conformation of surface-tethered DNA.[37,38]

In the present work, we build on these measurement concepts with a goal of quantifying DNA populations in the double-layer region in response to applied potential. An indium-tin-oxide (ITO) thin film sputter-coated onto glass provides a uniform and highly transparent electrode surface for control of the potential, while simultaneously allowing low-background imaging of individual labeled DNA molecules near the interface. ITO has previously been used in bulk fluorescence measurements to investigate the effect of applied potential on streptavidin-biotin interactions[12] and the accumulation of individual labeled antibodies at a charged surface.[24] Using through-the-objective TIRF microscopy, we quantify the interfacial DNA population at an ITO surface in response to applied potential at varying electrolyte ionic strengths by counting individual molecules in fluorescence images. To investigate whether the DNA molecules are adsorbed to the ITO surface, diffusion coefficients were measured at each applied potential by tracking individual molecules in images. The results show that the interfacial DNA population grows with increasing positive applied potential, while the diffusion of individual molecules at the interface remains similar to their diffusion in free solution. The DNA accumulation with applied potential is interpreted with a Gouy-Chapman model for ion concentrations in the electrical double layer at the electrode interface, which both indicate that the DNA accumulates at the interface like an anion with low net charge. The results are consistent with DNA charge largely screened by counterions and the DNA being free to diffuse at the interface with no apparent surface adsorption.

4.2 Experimental Section

4.2.1 Chemicals and Materials

The 14,876 base pair (bp) supercoiled plasmid, PTX21, (see Appendix B.1) was graciously provided by the Eric Jorgensen Lab (University of Utah). Oxazole yellow dimer (YOYO-1) iodide DNA intercalating dye (1 mM solution in DMSO) was purchased from Invitrogen (Carlsbad, CA) and used as received. All buffers and solutions were made using water distilled from a quartz still and purified with a Barnstead NANOpure II system (Boston, MA) to a solution resistivity of approximately 18 MΩ·cm. Indium tin oxide (ITO) sputter-coated 20 x 20 mm No. 1 glass coverslips (sheet resistivity of 15-30 Ω/square) were purchased from SPi Supplies (West Chester, PA). Buffers and supporting electrolyte solutions were made with ACS grade sodium phosphate monobasic monohydrate, sodium chloride, and sodium hydroxide from Mallinckrodt (Phillipsburg, NJ). Spectroscopy grade Omnisolv methanol from EMD chemicals (Darmstadt, Germany) was used for cleaning ITO coverslips. Conductive silver epoxy resin was purchased from VWR (West Chester, PA).

4.2.2 DNA Solutions

All solutions used for fluorescence imaging were prepared in sodium phosphate buffer adjusted to pH 8.0 with sodium hydroxide in addition to varying amounts of sodium chloride supporting electrolyte. 14,876 bp plasmid DNA stock solutions were prepared with 180 pM DNA, 160 nM YOYO-1 (DNA bp to dye ratio of 15 to 1), 75 μM sodium chloride, and 75 μM sodium phosphate buffer. The DNA-YOYO-1 stock solution was allowed to incubate at room temperature for approximately 4 h to allow the YOYO-1 fluorescent label to intercalate into the double-stranded DNA before being

further diluted to concentrations of 5.3, 10.5, 21, and 42 pM in buffers of varying ionic strength. The 10.5, 12.8, and 25.6 pM solutions were all prepared with 75 µM phosphate buffer in addition sodium chloride electrolyte at 75 µM, 3 mM, and 30 mM respectively. The 5.3 pM DNA solution was prepared with low concentration electrolyte containing 2.3 µM phosphate buffer and 2.3 µM sodium chloride.

4.2.3 Preparation of ITO Substrates

ITO electrodes were prepared by first rinsing for 10 min each in 18 MΩ·cm water and methanol. The ITO coated side of the coverslip was then cleaned for 25 min in a UV ozone cleaner, Jelight Co. model 342. Copper wire leads were attached to the edge of the ITO coated coverslip using conductive silver epoxy resin which was then placed in a 120 ºC oven overnight to allow the conductive paste to harden. The slides with attached wire leads were then UV ozone cleaned again for 25 min and assembled into an imaging electrochemical flow cell shown in Figure 4.1. This cell consists of a wired ITO slide separated from a top glass plate by a silicone gasket. The top has an inlet port and outlet port which allow solution to be flowed, and access by a platinum counter electrode and a Cypress Systems (ESA, inc.) model EE009 Ag-AgCl reference electrode. The flow cell is held together tightly by a stainless-steel top and bottom plate whose interior is covered with Parafilm to prevent electrical shorts to ground. A Pine model AFCBP1 3-electrode potentiostat was used to apply surface potentials.

4.2.4 Fluorescence Microscopy

Dilute YOYO-1 labeled DNA solutions at an ITO interface were imaged with an Olympus iX71 inverted microscope using through-the-objective TIRF illumination

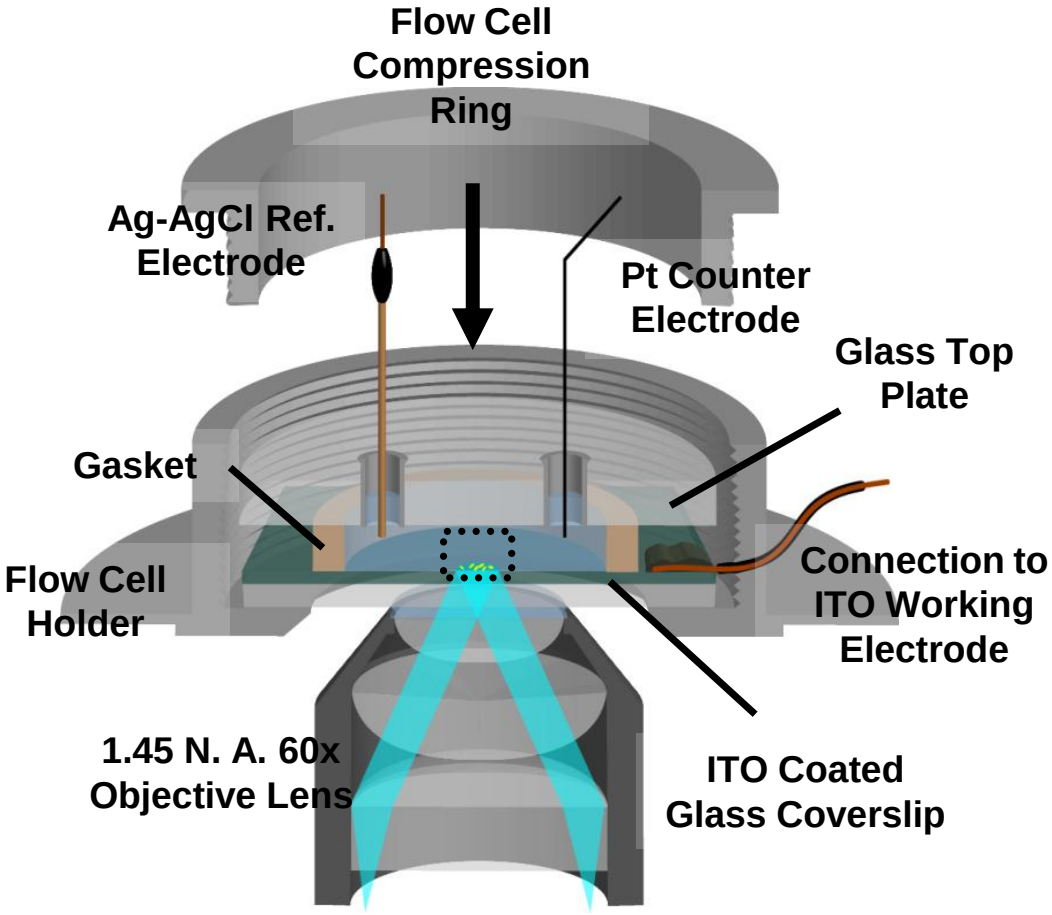

Figure 4.1. Sample flow cell assembled into microscope stage holder with through-the-objective TIRF illumination.

described previously[25] with several modifications. Briefly, 488 nm illumination from a Coherent Innova 90C argon ion laser is coupled into a polarization maintaining optical fiber (Thorlabs) and directed to the back of the microscope frame. Light emitted from the fiber is collected and collimated using a planoconvex lens and then passed through a 488 nm laser band-pass filter (Chroma). The laser beam is then focused with another planoconvex lens onto the back focal plane of a 60× 1.45 N.A. oil immersion objective lens, creating a collimated beam emerging from the objective lens. By translating the optical fiber tip horizontally relative to the objective lens optical axis, the angle of the beam emerging from the objective increased until total internal reflection was achieved at the glass-ITO-aqueous interface. The ~200 nm thick ITO film is not expected to impact the ability to generate an evanescent field at the ITO-aqueous interface according to calculations of the excitation radiation spatial intensity distribution versus incident angle for three-phase dielectric thin film structures.[39] A total laser power of 1 mW was incident on the back of the objective lens, corresponding to approximately 13 W cm^{-2} at the sample surface. Before any potential-control and imaging experiments were conducted, the ITO surface was poised at 0.8 V versus Ag-AgCl and illuminated with 1 mW 488 nm laser radiation for 30 min to bleach any adsorbed fluorescent impurities. Imaging was performed using an electron multiplying charge coupled device (EMCCD) camera (Andor iXon^{EM}+ 897) using a 256 × 256 pixel region of the sensor (70 × 70 μm region at 60× magnification). Videos were collected by imaging continuously for 140 s with 27.5 ms integration times (36.4 fps) in frame transfer mode with the electron multiplying gain set at 50×.

4.2.5 Image Analysis

Image analysis was performed using custom programs written in the Matlab (Mathworks) software environment. Fluorescently-labeled DNA molecules in each image were counted using an algorithm described previously.[25] Molecules in images were counted by locating regions with at least three adjacent pixels with intensity higher than a detection intensity threshold, $I_{thold} = n_{std}\sigma_{bg} + \mu_{bg}$, set at a number, n_{std}, of background standard deviations, σ_{bg}, higher than the mean background intensity, μ_{bg}. Before analysis, the analog-to-digital unit (ADU) intensity was converted to photoelectron counts. The conversion was made using a linear calibration fit to a plot of pixel intensity variance versus mean pixel intensity in ADU generated from images of flat white light noise (see Appendix B.2).[40]

The detection intensity threshold establishes a depth into solution in the evanescent field illumination region that molecules can be detected. The intensity from individual labeled plasmids varies from being indistinguishable from background when they are far from the surface to some maximum fluorescence intensity from DNA at its distance of closest approach to the surface. The intensity-distance relationship diverges from a simple exponential decay function due to scattered light from the interface penetrating into solution, and the large size of the plasmids relative the evanescent field (400 nm diameter DNA vs. ≈ 100 to 200 nm evanescent field,[39] see Appendix B.3). Detection intensity thresholds were chosen to minimize counting molecules illuminated by scattered light far from the interface. The detection threshold was set for individual video series at different DNA concentrations at n_{std} = 5.1 to 6.7, in accordance with their individual signal-to-noise ratios. A description of the process used to set I_{thold} and the

effect of I_{thold} on fitted parameters from the population thresholds are presented in Appendix B.4.

At $n_{std} > 5$, the false positive rate is expected to be negligible.[25] Before imaging experiments were conducted, ITO substrates were covered with blank phosphate buffer, poised at 0.8 V and illuminated with laser radiation for 30 min to photobleach any fluorescent contamination on the surface. Due to the high detection threshold, low integration times, low illumination intensity, and bleaching before observation, less than 0.05 spots per video frame were detected in blanks.

DNA diffusion coefficients were determined by tracking the intensity center-of-mass of individual molecules with sub-pixel precision. The DNA is larger than the point spread function of the microscope,[25] and diffused during single image integrations, so the center of mass should be a better estimate of the molecule center coordinate than a fit to a point spread function. Single molecule trajectories were generated by selecting a molecule coordinate at the beginning of the video and searching for another coordinate in the subsequent frame within a detection radius of 1.3 μm of the previous coordinate. This process was repeated using the new coordinate on the next video frame until no additional coordinates were located, indicating that the molecule had diffused out of the evanescent field. The detection radius was four times the mean step size predicted by the measured DNA diffusion coefficient. To reduce the probability of collecting spurious traces by jumping between different molecules which happen to be in the same detection radius, only video frames with fewer than 40 counted molecules were used for tracking, typically the first 3 to 15 s of each accumulation. For 4,900 μm^2 (70 × 70 μm) images, and a detection area of 5.3 μm^2 (1.3 μm detection radius), the probability of a molecule

randomly appearing in the detection radius of a different molecule from the previous frame is less than 4.3 %, the ratio of the detection area to the total image area multiplied by the total number of molecules.

4.3 Results and Discussion

4.3.1 Counting YOYO-1 Labeled DNA Populations near an ITO Interface

The effect of positive applied potential on the population of YOYO-1 labeled 14,876 bp supercoiled plasmid DNA is demonstrated by Figure 4.2a. Figure 4.2a shows representative fluorescence images of anionic DNA in pH 8.0 buffer diffusing in the evanescent field near an ITO-aqueous interface ~120 s after applying potentials between 0 and 0.9 V vs. a Ag-AgCl reference electrode. Under positive applied potential, the population of DNA interacting with the electrical double-layer increases dramatically, up to a factor of 200 times the population at a negatively charged interface. The potential response is reversible, and all DNA appears to freely diffuse near the surface when the applied potential is less than approximately 1.3 V (i.e., no stationary adsorbed DNA is observed). When the potential is stepped from 1.3 V back down to 0 V, the population declines to its equilibrium values at 0 V within 5 seconds. At applied potentials higher than 1.4 V, DNA adsorbs to the surface irreversibly. Interfacial populations of YOYO-1 labeled DNA were determined using image analysis that required molecular spots to exceed an intensity threshold in multiple adjacent pixels to distinguish DNA from single-pixel detector noise (see above). Figure 4.2b shows DNA detected in a representative image of 10.5 pM DNA solution in 0.28 mM ionic strength electrolyte at a surface potential of 0.8 V. The DNA populations detected in this manner, N_{DET}, were determined 120 s after each potential step by averaging the molecule counts in the final 500 frames,

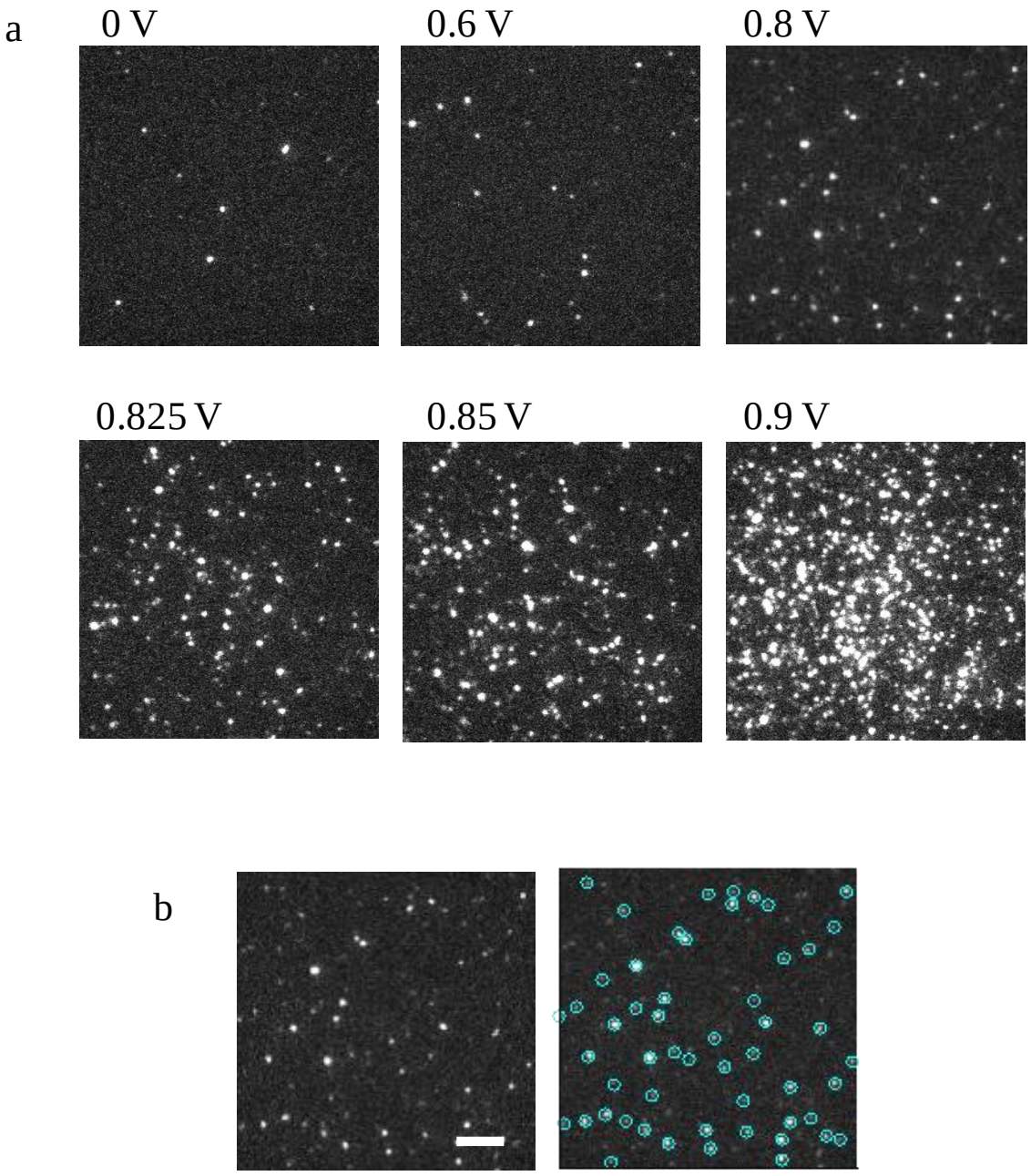

Figure 4.2. Comparison of interfacial DNA population at varying applied potential. a) Sample image of 10.5 pM DNA, 0.28 mM ionic strength solution over ITO ~120 s after indicated potential step versus Ag-AgCl ref. electrode. b) Molecules located by counting algorithm in 0.8 V sample image; scale bar is 10 microns.

or 13.8 s. Plots of N_{DET} against applied potential for ionic strengths of 8.4 μM, 0.28 mM, 3.2 mM and 30 mM are shown in Figure 4.3a-d.

4.3.4 Interfacial DNA Diffusion under Potential Control

Even when high potentials, between 0.7 to 1.3 V vs. Ag-AgCl, are applied to the ITO-solution interface, resulting in labeled DNA population increases of up to 200 fold, the DNA molecules appear to freely diffuse in the evanescent field region. If the accumulation of DNA was a result of adsorption of the DNA to the ITO surface, then the diffusion coefficient of DNA would be expected to decrease significantly with increasing positive applied potential. By tracking the locations of individual molecules between video frames, we were able to measure the effect of applied potential on the diffusion coefficient of DNA at the ITO-solution interface. The same video data used for measuring DNA populations were analyzed to determine the trajectories of individual molecules. The center-of-mass of each molecular spot was tracked with sub-pixel (< 260 nm) resolution. From the trajectories, the mean square displacement, $\langle r^2 \rangle = \langle x^2 + y^2 \rangle$, was determined and plotted versus elapsed time, t. The resulting plots are linear (see Appendix B.5) as expected from the Einstein equation in two dimensions: $\langle r^2 \rangle = 4Dt$. From the slopes of these plots, the interfacial diffusion coefficient of labeled DNA versus applied potential was determined at ionic strengths of 8.4 μM, 0.28 mM, and 3.2 mM and the results are plotted in Figure 4.4, and summarized in Table 4.1.

For comparison, the diffusion coefficient of YOYO-1 labeled DNA diffusing in free solution was also measured using an epi-illumination fluorescence microscope focused approximately 10 μm beyond a glass coverslip in solution. The details of the epi-illumination instrument have previously been reported by Hanley et al.,[41] and are

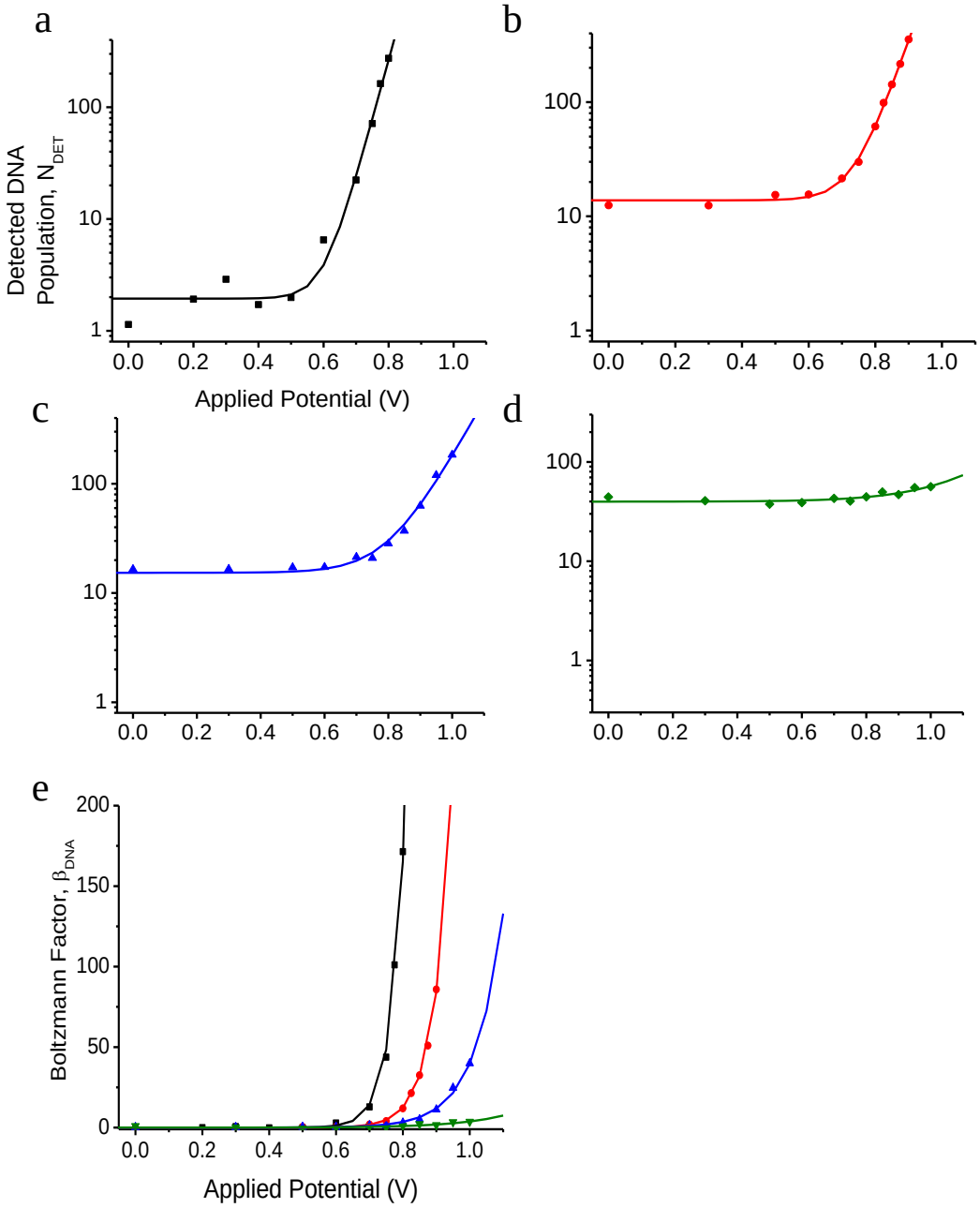

Figure 4.3. Mean equilibrium molecule counts after potential step with Boltzmann fit using equation 4 (solid line) for a) 8.5 µM (black squares), b) 290 µM (red circles), c) 3.2 mM (blue triangles), and d) 30 mM (green diamonds) ionic strength., e) Boltzmann factor, $\beta_{DNA} = [N_{DET} - (N_E^0 - N_D^0)]/ N_D^0$.

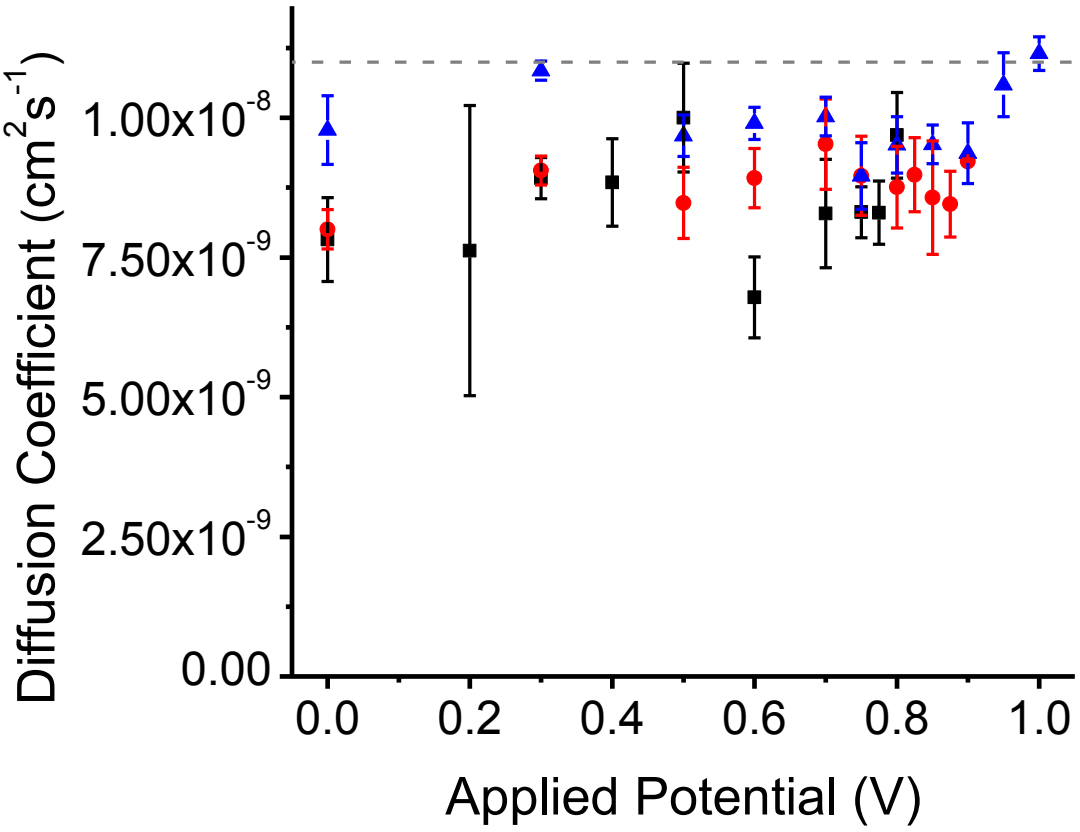

Figure 4.4. DNA diffusion coefficients, D, plotted versus applied potential for 8.4 µM (black squares), 0.28 mM (red circles), and 3.2 mM (blue triangles) ionic strengths. The dotted line is the measured bulk solution DNA diffusion coefficient. Error bars are two standard deviations of the mean.

Table 4.1

Parameters from Boltzmann Model for DNA Accumulation at the Interface with Applied Potential

DNA concentration (pM)	Phosphate buffer conc. (μM)	Sodium chloride conc. (mM)	Ionic strength (mM)	Theoretical Debye length, κ^{-1} (nm)[b]	OHP zero potential (V) , φ_{PZC}[c]	Boltzmann exponential factor, β (V^{-1})[c]	Evanescent field DNA population, N_E^0 (molecule counts)[c]	Double-layer DNA population, N_D^0 (molecule counts)[c]	Fraction of DNA under potential influence, $N_D^0 N_E^{0-1}$ [c]	Diffusion coefficient × 10^8, D ($cm^2 s^{-1}$)[d]
1.6[a]	75[a]	.075[a]	0.28[a]	18[a]	-	-	-	-	-	1.11 ± 0.03[a]
5.3 pM	2.3	.0023	.0084	100	0.59 ± 0.02	25 ± 4	3.5 ± 1	1.5 ± 0.5	0.45 ± 0.2	0.85 ± 0.06
10.5 pM	75	.075	0.28	18	0.67 ± 0.01	19 ± 1	18 ± 1	4.0 ± 0.2	0.22 ± 0.02	0.88 ± 0.03
21.0 pM	75	3	3.2	5.3	0.70 ± 0.02	12 ± 2	20 ± 2	4.2 ± 0.6	0.22 ± 0.03	0.98 ± 0.04
42.0 pM	75	30	30	1.7	0.80 ± 0.06	7 ± 5	44 ± 2	3.6 ± 2	0.1 ± 0.05	-

[a] Quantities evaluated in bulk solution 10 μm away from the interface

[b] Calculated from Equation 1

[c] Parameter from fit of Equation 4 to data in Supporting Information. Uncertainties are 2 standard deviations of the mean (95 % confidence), determined using bootstrap method with resampled residuals from fit.

[d] Diffusion coefficient D calculated from linear least squares fit of mean squared displacement versus time to the diffusion equation: $\langle x^2 \rangle = 4Dt$. Uncertainties are at 95 % confidence interval from the uncertainty in fitted least squares slope.

[e] Lifetime τ determined from exponential decay constant from fit to data in Figure 8. Uncertainties are at 95 % confidence interval from uncertainty in fitted exponential decay time constants.

summarized in Appendix B.3 along with plots of mean squared molecule displacement, $\langle r^2 \rangle$, versus elapsed time, t, for free-solution DNA at 0.28 mM ionic strength. From these results, the labeled DNA diffusion coefficient in free solution was determined to be $D = 1.11 (\pm 0.03) \times 10^{-8}\ cm^2 s^{-1}$. This diffusion coefficient is somewhat lower than other estimates for DNA of similar molecule weight,[29,42-44] possibly due to the intercalating YOYO-1 fluorescent label relaxing supercoiling[45] and reducing the compactness of the DNA. The equivalent hard-sphere diameter of the DNA in solution can be estimated from the Stokes-Einstein equation:

$$d = \frac{kT}{3\pi\eta D} \qquad [4.1]$$

where the solution viscosity is assumed to be that of water, $\eta = 0.9$ cP, and the resulting diameter of DNA was found to be 400 ± 10 nm. The validity of the Stokes-Einstein relationship was verified by measuring D for fluorescently labeled latex spheres of known size, and the results are found in Appendix B.3.

As shown in Figure 4.4, diffusion coefficients of labeled DNA near the electrode surface are very close to those measured in free solution, $0.85 \pm 0.06 \times 10\text{-}8\ cm^2 s^{-1}$, $0.88 \pm 0.03 \times 10\text{-}8\ cm^2 s^{-1}$, $0.98 \pm 0.04 \times 10\text{-}8\ cm2s^{-1}$ for 8.4 µM, 0.28 mM, and 3.2 mM ionic strength solution, respectively. There is no trend in D versus applied potential, matching behavior previously reported for DNA on optically transparent carbon electrodes.[36] This result indicates that DNA plasmids do not adsorb to the surface at potentials between 0 V and 0.9 V. At potentials beyond 0.9 V, the interfacial DNA population rapidly became too high for tracking of individual molecules. DNA can be made to adsorb onto ITO and become immobile, but this requires very high applied potentials, greater than 1.3 V. This

process is irreversible as potential steps back to 0 V from 1.3 V do not cause adsorbed DNA to unbind from the surface. The slight increase in D with increasing electrolyte ionic strength is likely due to compaction of the DNA random coil as electrostatic repulsion between phosphate groups is screened by excess electrolyte.[46]

4.3.2 Gouy-Chapman Model for the Response of Interfacial DNA Populations to Applied Potential

Since an applied potential between 0.7 and 1.3 V significantly increases the interfacial population of DNA, while having no significant influence on diffusion near the interface, we hypothesize that the DNA remains in solution and accumulates in the electrical double layer formed at the polarized ITO-aqueous interface. The negatively charged DNA gathers at the interface because of electrostatic attraction to the positively charged electrical double layer, while diffusion parallel to the surface is unaffected by applied potential because there is no potential gradient in the interfacial plane. A simple Gouy-Chapman model was developed to account for the potential-dependent accumulation of DNA in the electrical double layer at the ITO interface.

The model begins with Gouy-Chapman theory, which describes the electrical potential and ion concentration in the diffuse layer near an interface. At small applied potentials, φ^0, the Gouy-Chapman potential profile, $\varphi(x)$, decays exponential with distance into solution, x:[47,48]

$$\varphi(x) = \varphi^0 e^{-\kappa x} \qquad [4.2]$$

The dimensions of the electrical double layer are conveniently described by the Debye length, κ^{-1}, the decay constant of the potential profile. The Debye length for a 1:1

electrolyte, κ^{-1}, is a function of the bulk ion concentration, C^0, the ion charge, z, the elementary charge, e, the electrical permittivity of a vacuum, ε_0, the relative permittivity, ε, Boltzmann's constant, k, and the solution temperature, T.

$$\kappa^{-1} = \left(\frac{\varepsilon\varepsilon_0 kT}{2C^0 z^2 e^2}\right)^{1/2} \quad [4.3]$$

The spatial profile of the ion population in the double layer, $N_D(x)$, depends on the local potential, $\varphi(x)$, and the bulk ion population, N^0_D, at $x >> \kappa^{-1}$:

$$N_D(x) = N_D^0 e^{-\frac{ze\varphi(x)}{kT}} \quad [4.4]$$

Because the DNA plasmids investigated are polyanions, they are expected to exhibit electrostatic Boltzmann accumulation near a charged interface. Because the 150 nm evanescent field penetration depth is larger than the Debye lengths (2 to 100 nm) predicted for the ionic strength, not all detected molecules are expected to be under potential control. For this reason, $N_D(x)$ only describes the DNA population in the double layer region, where N_D^0 is the expected double-layer population at zero surface charge. The DNA population in the entire evanescent field detection volume is N^0_E, so that the DNA population outside the double layer, but inside the detection volume is $N^0_E - N^0_D$. The potential profile of the electrical double layer for real systems at high applied potential arise from complex ion distributions[49] and even changes in solvent structure.[50] We simplify this model by defining an average population of DNA within the double layer, N_D, which experiences a mean electrical potential, φ. This simplification allows us to define a simple Boltzmann parameter describing sensitivity to

applied potential, $\beta = -Ze/kT$, where Z is the net charge of the portion of the DNA molecule averaged over the double-layer region.

The interfacial DNA population is governed by the electrical potential at the distance of closest approach for ions at the electrode surface. This distance, the outer Helmholtz plane (OHP), represents the thickness of an adsorbed layer of water and ions. The potential term from equation 4.4 must be modified to include the potential applied by the potentiostat, E, and an offset, the threshold OHP potential, φ^0_{OHP}, representing the potential required to generate zero net charge at the OHP. The threshold OHP potential is similar to the potential of zero charge (φ_{PZC}); φ_{PZC} is the potential required to neutralize all charge on the *electrode* side of the interface, while φ^0_{OHP} is the potential which neutralizes charge on the *solution* side of the interface. When $E = \varphi_{PZC}$ the potential in the electrical double layer is not zero, due to excess charge from specifically adsorbed ions and charged groups on the ITO surface. Additional applied potential, $E = \varphi^0_{OHP}$, is required to neutralize this excess surface charge so that the net potential accessible to ions in solution is proportional to $E - \varphi^0_{OHP}$. The OHP potential is not exactly equal to $E - \varphi^0_{OHP}$, because of potential drop across the Stern layer. This potential drop is captured by a fractional factor built into the empirical Boltzmann sensitivity parameter, β.

These modifications to equation 4.4 yield equation 4.5, which describes the interfacial DNA population in the evanescent –field region as a function of applied potential:

$$N_{DET} = (N_E^0 - N_D^0) + N_D^0 e^{-\beta(E-\varphi^0_{OHP})} \qquad [4.5]$$

Using a non-linear least-squares search, equation 4.5 was fit to measured N_{DET} to determine values for N^0_E, N^0_D, β and φ^0_{OHP}, and the results are plotted in Figure 4.3a-d, with fitted parameters listed in Table 4.1. Uncertainties in reported parameters were estimated using the bootstrap method[51] generated by adding randomized residuals to a best fit curve. The residuals included $(N_{DET})^{1/2}$ scaling to reflect the Poisson distribution of errors in N_{DET}. Standard deviations of the mean for each parameter were estimated by fitting a Gaussian function to a histogram of bootstrap parameter values. The DNA concentration increase in the double layer, $\exp[-\beta(E- \varphi^0_{OHP})]$, can be determined from $[N_{DET} - (N^0_E - N^0_E)]/N^0_D$. These results are summarized in Figure 4.3e and demonstrate the sensitivity of DNA accumulation to ionic strength. As the double-layer extends further into solution, the influence of applied potential on the interfacial population increases significantly.

As the ionic strength is decreased and the Debye length increases, not only should the potential sensitivity increase but also the fraction of DNA molecules in the evanescent field region that are within the double layer region. To test this hypothesis, the ratio N^0_D/ N^0_E, the fraction of molecules detected that experience electric potential, was plotted versus the Debye length, and the results are shown in Figure 4.5. The increasing trend in $N_D{}^0/ N_E{}^0$ with κ^{-1} is a result of the double layer region becoming a larger fraction of the imaging detection volume.

The evanescent field imaging depth can be estimated by determining the distance into solution required to supply $N_E{}^0$ molecules to a 70 μm × 70 μm image area at a given DNA concentration. The average sampling depth estimated from $N_E{}^0$ at four DNA concentrations is 410 ± 260 nm (95% confidence). While the average is larger than the

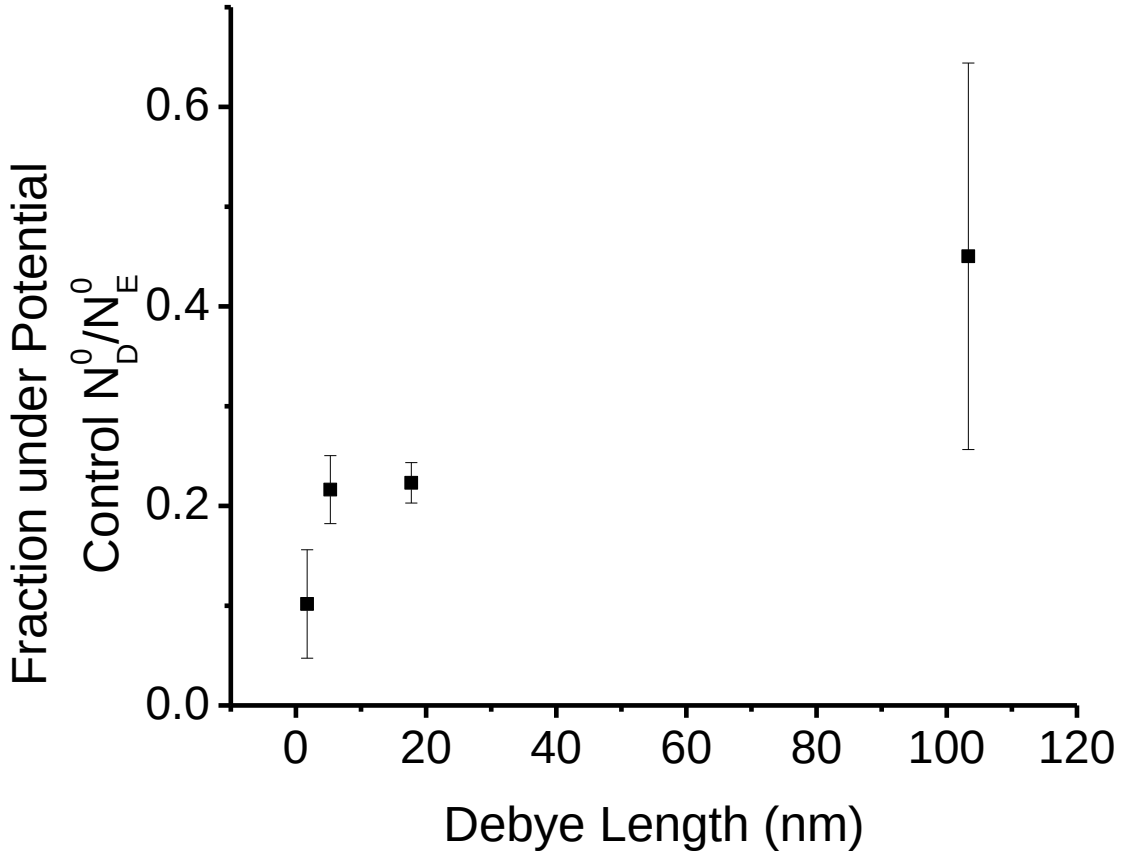

Figure 4.5. Fraction of DNA population in the evanescent detection volume influenced by the double-layer region, N_D^0/ N_E^0 from fit to Equation 4, plotted versus Debye length, κ^{-1}. Error bars are two standard deviations of the mean estimated using bootstrap method.

expected evanescent field depth of 150 nm from our angle of incidence,[39] the result includes the expected value within the large uncertainty bounds. Anomalously high numbers of YOYO-1 labeled DNA diffusing near silica surfaces have been reported by He *et al.*,[35] and the results correspond to sampling depths that were 500 to 800 nm, or 3 to 6 times greater than the evanescent wave depth of 140 nm. These elevated molecule counts were attributed to diffusion of DNA into and out of the evanescent field region during the 257-ms image integration times and confirmed with random-walk simulations. This phenomenon should have less impact on the present experiments because the integration times were $1/10^{th}$ or 26 ms, which reduces the distance over which DNA can diffuse during the acquisition of an image by a factor of $(1/10)^{1/2}$ or 0.32. Excess molecular counts at the interface may also arise simply from the large size of the DNA molecules. The hard-sphere equivalent diameter of the DNA determined from its solution diffusion coefficient is 400 nm (see Appendix B.3), and it is highly labeled. Therefore, it is possible for DNA with a center of mass hundreds of nanometers away from the surface to have labeled base pairs inside the evanescent field region. Because of the size of DNA and its possible diffusion within the observation time, the population of DNA, N_E^0, sampled within the evanescent field region will likely include molecules whose center of mass distances from the surface exceed 150 nm.

The fitted Boltzmann potential sensitivity parameters in V^{-1} are plotted verses Debye length, κ^{-1} in nm, in Figure 4.6. The parameter β represents the sensitivity of interfacial DNA population to applied potential, and it varies significantly with electrolyte concentration. For large κ^{-1} the DNA population exhibits a larger increase with applied potential than for short κ^{-1} because the double layer penetrates into a larger

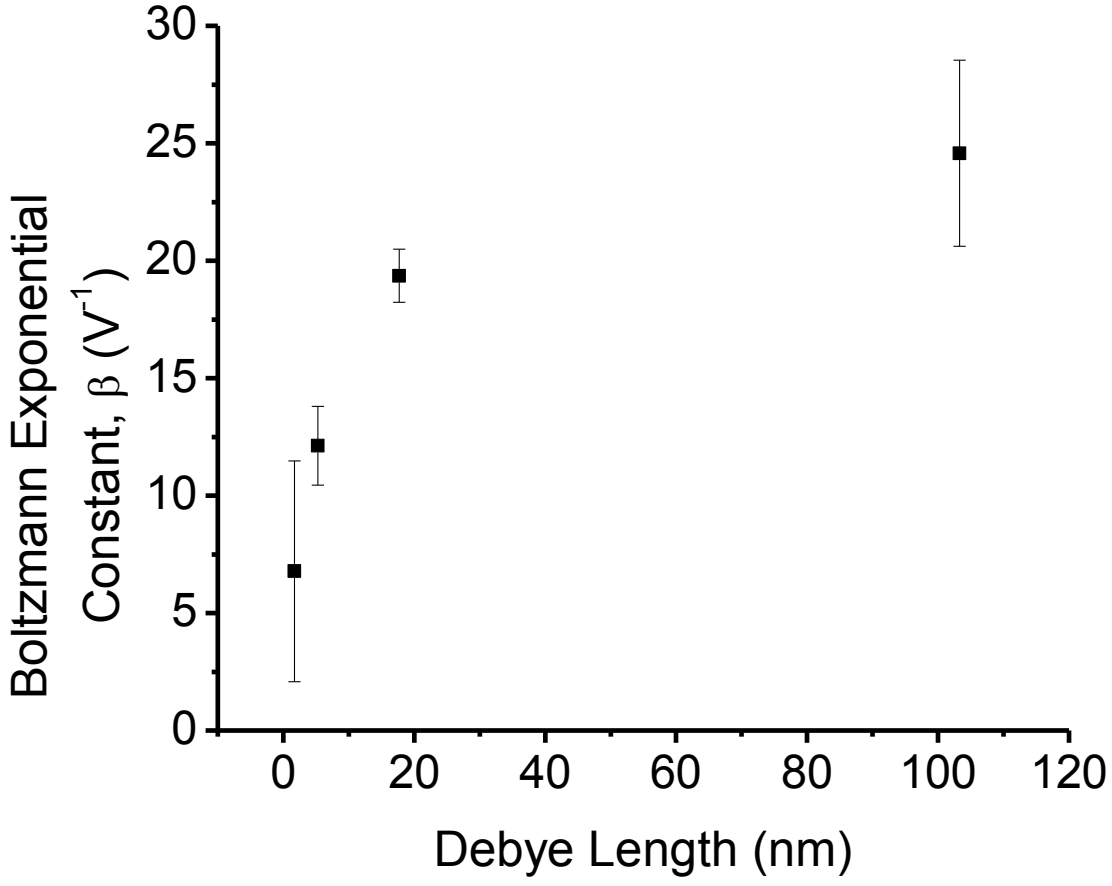

Figure 4.6. Boltzmann potential sensitivity constant, β, from fit to Equation 3 plotted versus Debye length , κ^{-1}. Error bars are two standard deviations of the mean estimated using bootstrap method.

fraction of the imaging detection volume. For all Debye lengths, β is less than 38.9 V^{-1}, the sensitivity expected for a monovalent ion experiencing the full applied potential. The results indicate that the DNA exhibits a small net charge and experiences a small fraction of the applied potential.

The final parameter of the DNA accumulation fit to equation 4.4 is the threshold OHP potential, φ^0_{OHP}, which increases from 0.59 V to 0.80 V for 8.4 μM to 30 mM ionic strengths respectively, as listed in Table 4.1. The relatively high positive φ^0_{OHP} for these ITO surfaces in contact with pH 8.0 buffer indicates that there is net negative charge on the surface that must be overwhelmed with a positive applied potential before DNA begins to accumulate. This result is consistent with negative zeta potentials observed for aqueous ITO colloids at pH higher than their isoelectric pH of 5 to 6.[52,53] The increasing trend in φ^0_{OHP} may be a result of increasing chloride ion adsorption to the electrode surface at high electrolyte concentrations requiring higher applied potential to overcome the additional negative surface charge.

4.3.3 Gouy-Chapman Model for DNA Accumulation with Applied Potential

The simple Gouy-Chapman model in equation 4.4 describes the relative DNA potential sensitivity and the fraction of DNA under potential control, but it does not accurately model the distance dependence of ion build-up in the diffuse double-layer. Molecule counts in the evanescent wave are better modeled by integrating the ion concentration in the entire electrical double-layer. From this double-layer model one can directly compare DNA accumulation to electrolyte ion accumulation, and estimate the net electrical charge on DNA. We employ a simple Gouy-Chapman model to describe ionic

strength dependence of DNA accumulation in the double-layer: DNA concentration is modeled by numerically integrating equation 4.3, the Boltzmann distribution for the ion concentration profile, from the ITO surface to the evanescent field depth of 150 nm. The potential distribution, $\varphi(x)$, is approximated with an exponential decay function, equation 4.1, with a decay constant κ, equation 4.2, calculated for each experimental ionic strength. DNA net charge is approximated as a parameter in a fit of the integral of equation 4.4 to the experimental DNA accumulation curves normalized to N_E^0 and offset by φ^0_{OHP}, where values for N_E^0 and φ^0_{OHP} were taken from fits of the data to equation 4.5. As shown in Figure 4.7 the model fits the data well with, DNA net charges between Z = 0.6 and 0.8 excess electrons, indicating that DNA charge is almost completely screened by counterions. These results are, fortunately, not very sensitive to the sampling depth that governs the value of N_E^0 and the integration of charge in the double layer. If the effective sampling depth is increased to the experimental result of 410 nm (due to the size and diffusional motion of DNA relative to the evanescent field, see above) and used in the integration, the DNA net charge increases by only 20% compared to the above values, ranging from Z = 0.96 to 0.79 for low to high ionic strength, respectively.

Estimates of the effective charge per base pair vary in the literature, ranging from 0.6 electron equivalents measured for capillary zone electrophoresis,[54] to as low as 0.06 electron equivalents measured for immobilized DNA stretched in an electric field.[55] Both of these methods predict significant net charge on large oligonucleotides; however, the static double-layer concentration has several key differences with electrophoresis experiments. During electrophoresis, counterions in the diffuse layer around polyelectrolytes are sheared away as they migrate in opposite directions due to their

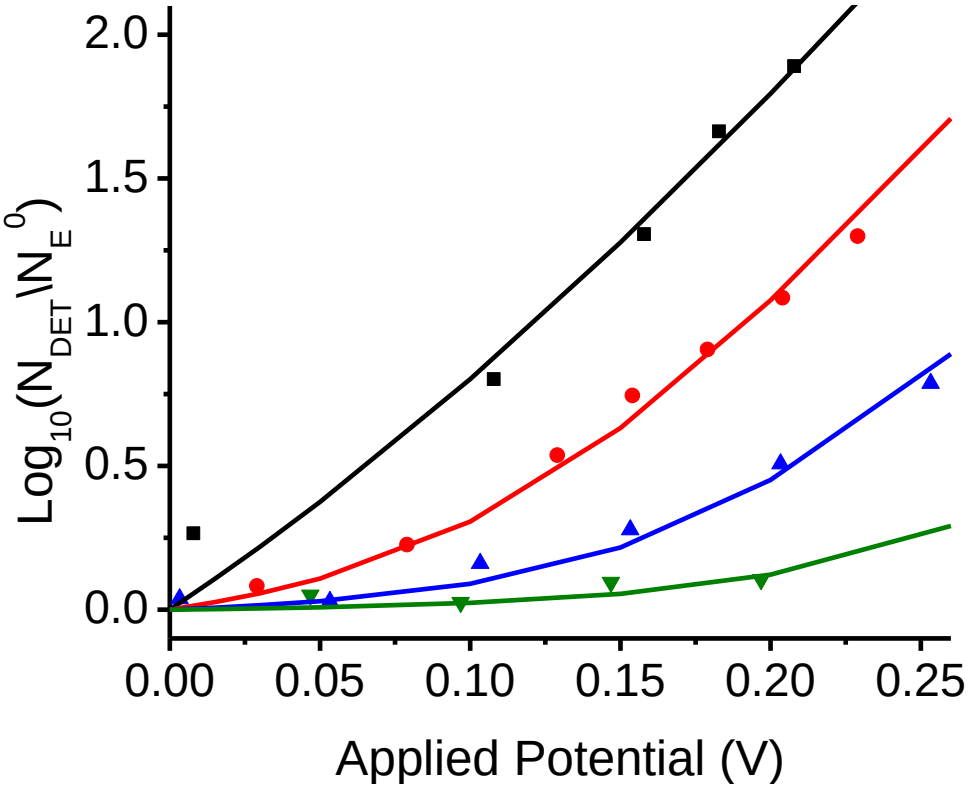

Figure 4.7. DNA concentration factor, N_{DET}/N_E^0, plotted versus applied potential for 8.4 µM (black squares), 0.28 mM (red circles), 3.2 mM (blue triangles), and 30 mM (green triangles) electrolyte ionic strengths. Solid lines are models of Gouy-Chapman double-layer ion concentration integrated through the evanescent field (150 nm from surface) fit to N_{DET}/N_E^0 with net DNA charge in electron equivalents of Z = 0.79, 0.79, 0.70, 0.61, respectively.

opposing charges. The zeta potential, which determines the magnitude of the electrophoretic mobility, is the potential at the "slip plane" where counterions are sheared away. The slip, or shear, plane is thought to be slightly beyond a stagnant water layer several angstroms thick adsorbed to the outer Helmholtz plane. At ionic strengths below 100 mM, this shear plane is within the diffuse double-layer, and the surface charge on the polyelectrolyte is screened primarily by adsorbed ions in the Stern layer. In the present static double-layer accumulation experiment, there is no electrophoresis and no shearing of counterions. The counterions in the diffuse layer are still present as the DNA approaches the surface, and they significantly screen the DNA surface charge. In addition, although the DNA molecules contain thousands of charged phosphate groups, the molecule is large and only a fraction of the charged groups reside in the thin double-layer region.

A detailed description of interacting double-layers in the absence of shear or flow is provided by Derjaguin and Landau, Verwey and Overbeek (DLVO) theory,[56,57] which has been applied to the case of hard spheres approaching a charged interface.[58] Bhattacharjee et al. calculate the potential profile for small particles of radius close to κ^{-1} and surface electrical potential of 25 mV approaching a charged interface of the same potential. Maximum interaction potentials for particles close to the charged interface are only a few kT, indicating that most of the total charge is screened by counterions. An exact DLVO description of polyelectrolytes such as DNA is difficult because they have no definite surface boundary or charge density, but the results of this theory for simple spherical colloids are consistent with the DNA accumulation results.

4.4 Summary

Using single molecule TIRFM techniques, we have developed a quantitative description of the effect of surface potential and electrolyte ionic strength on the interfacial population and diffusion of aqueous DNA. Fluorescently labeled DNA plasmids were imaged near a transparent indium tin oxide electrode surface while interfacial electrical potential was increased from 0 to 1.0 V. After potential steps from 0 V to 0.7 V and above, DNA populations increase to an elevated equilibrium value. This process is reversible; DNA populations relax after the potential is returned to 0 V. Diffusion at the interface was investigated by tracking single molecules trajectories at the interface, and no potential dependence was observed. Interfacial diffusion coefficients were similar to bulk diffusion coefficients, indicating that the DNA does not significantly adsorb to the surface as it accumulates at the interface. At high applied potentials, we hypothesize that the DNA gathers at the interface due to attractive electrostatic interactions with the electrical double layer. Plots of interfacial DNA population versus potential were fit by a Boltzmann model containing parameters for the fraction of the DNA population under potential influence, the outer Helmholtz plane zero potential, and the potential sensitivity, β, of the DNA potential response. As ionic strength decreased, the resulting increase in the double-layer thickness increased both the fraction of observed DNA molecules under potential control, and β. A Gouy-Chapman model of ion accumulation in the double-layer suggests that the DNA has a low net charge, between 0.6 and 0.8 electron equivalents, which accounts for the low sensitivity to applied potential. The significant electrical charge on the phosphate-sugar backbone (~15,000 electron equivalents) is largely screened by counterions, and the large DNA plasmid

interacts only weakly with the potential at the interface. Until the threshold for DNA adsorption is reached, applied surface potential does not lead to strong DNA-surface interactions, even as the DNA population increases a hundred fold.

4.5 References

(1) Vermeer, A. W. P.; van Riemsdijk, W. H.; Koopal, L. K. *Langmuir* **1998**, *14*, 2810.

(2) Kaneco, S.; Itoh, K.; Katsumata, H.; Suzuki, T.; Masuyama, K.; Funasaka, K.; Hatano, K.; Ohta, K. *Environmental Science & Technology* **2003**, *37*, 1448.

(3) Weng; Van Riemsdijk, W. H.; Koopal, L. K.; Hiemstra, T. *Environmental Science & Technology* **2006**, *40*, 7494.

(4) Yang, K.; Lin, D.; Xing, B. *Langmuir* **2009**, *25*, 3571.

(5) He, J.-A.; Mosurkal, R.; Samuelson, L. A.; Li, L.; Kumar, J. *Langmuir* **2003**, *19*, 2169.

(6) Han, J.; Kim, H.; Kim, D. Y.; Jo, S. M.; Jang, S.-Y. *ACS Nano* **2010**, *4*, 3503.

(7) Haeussling, L.; Ringsdorf, H.; Schmitt, F. J.; Knoll, W. *Langmuir* **1991**, *7*, 1837.

(8) Altschuh, D.; Dubs, M. C.; Weiss, E.; Zeder-Lutz, G.; Van Regenmortel, M. H. V. *Biochemistry* **1992**, *31*, 6298.

(9) Liu, J.; Eddings, M. A.; Miles, A. R.; Bukasov, R.; Gale, B. K.; Shumaker-Parry, J. S. *Analytical Chemistry* **2009**, *81*, 4296.

(10) Watts, T. H.; Gaub, H. E.; McConnell, H. M. *Nature* **1986**, *320*, 179.

(11) Kalb, E.; Engel, J.; Tamm, L. K. *Biochemistry* **1990**, *29*, 1607.

(12) Asanov, A. N.; Wilson, W. W.; Oldham, P. B. *Analytical Chemistry* **1998**, *70*, 1156.

(13) Claesson, P. M.; Go¨lander, C.-G. *Journal of Colloid and Interface Science* **1987**, *117*, 366.

(14) Murphy, E. M.; Zachara, J. M.; Smith, S. C. *Environmental Science & Technology* **1990**, *24*, 1507.

(15) Jones, K. D.; Tiller, C. L. *Environmental Science & Technology* **1999**, *33*, 580.

(16) Sofia, S. J.; Premnath, V.; Merrill, E. W. *Macromolecules* **1998**, *31*, 5059.

(17) Schlapak, R.; Armitage, D.; Saucedo-Zeni, N.; Hohage, M.; Howorka, S. *Langmuir* **2007**, *23*, 10244.

(18) Axelrod, D. *Methods in Cell Biology* **1989**, *30*, 245.

(19) Wayment, J. R.; Harris, J. M. *Analytical Chemistry* **2008**, *81*, 336.

(20) Elenko, M. P.; Szostak, J. W.; van Oijen, A. M. *Journal of the American Chemical Society* **2009**, *131*, 9866.

(21) Liang, H.; Cheng, X.; Ma, Y. *Analytical Chemistry* **2009**, *81*, 2059.

(22) Fox, C. B.; Wayment, J. R.; Myers, G. A.; Endicott, S. K.; Harris, J. M. *Analytical Chemistry* **2009**, *81*, 5130.

(23) Miyake, T.; Tanii, T.; Sonobe, H.; Akahori, R.; Shimamoto, N.; Ueno, T.; Funatsu, T.; Ohdomari, I. *Analytical Chemistry* **2008**, *80*, 6018.

(24) Li, L.; Tian, X.; Zou, G.; Shi, Z.; Zhang, X.; Jin, W. *Analytical Chemistry* **2008**, *80*, 3999.

(25) Peterson, E. M.; Harris, J. M. *Analytical Chemistry* **2010**, *82*, 189.

(26) Smith, D. E.; Perkins, T. T.; Chu, S. *Macromolecules* **1996**, *29*, 1372.

(27) Ke, P. C.; Naumann, C. A. *Langmuir* **2001**, *17*, 3727.

(28) Ludes, M. D.; Wirth, M. J. *Analytical Chemistry* **2002**, *74*, 386.

(29) McHale, K.; Mabuchi, H. *Journal of the American Chemical Society* **2009**, *131*, 17901.

(30) McCain, K. S.; Hanley, D. C.; Harris, J. M. *Analytical Chemistry* **2003**, *75*, 4351.

(31) Takimoto, B.; Nabika, H.; Murakoshi, K. *The Journal of Physical Chemistry C* **2009**, *113*, 3127.

(32) Li, H.-W.; Park, H.-Y.; Porter, M. D.; Yeung, E. S. *Analytical Chemistry* **2005**, *77*, 3256.

(33) Park, H.-Y.; Li, H.-w.; Yeung, E. S.; Porter, M. D. *Langmuir* **2006**, *22*, 4244.

(34) Kang, S. H.; Shortreed, M. R.; Yeung, E. S. *Analytical Chemistry* **2001**, *73*, 1091.

(35) He, Y.; Li, H.-W.; Yeung, E. S. *The Journal of Physical Chemistry B* **2005**, *109*, 8820.

(36) Donner, S.; Li, H.-W.; Yeung, E. S.; Porter, M. D. *Analytical Chemistry* **2006**, *78*, 2816.

(37) Rant, U.; Arinaga, K.; Fujita, S.; Yokoyama, N.; Abstreiter, G.; Tornow, M. *Nano Letters* **2004**, *4*, 2441.

(38) Kaiser, W.; Rant, U. *Journal of the American Chemical Society* **2010**, *132*, 7935.

(39) Hansen, W. *Journal of the Optical Society of America* **1968**, *58*, 380.

(40) Mortara, L.; Fowler, A. *Proc. SPIE* **1981**, *290*, 28.

(41) Hanley, D. C.; Harris, J. M. *Analytical Chemistry* **2001**, *73*, 5030.

(42) Dawson, J. R.; Harpst, J. A. *Biopolymers* **1971**, *10*, 2499.

(43) Liu, M. K.; Giddings, J. C. *Macromolecules* **1993**, *26*, 3576.

(44) Robertson, R. M.; Laib, S.; Smith, D. E. *Proceedings of the National Academy of Sciences* **2006**, *103*, 7310.

(45) Larsson, A.; Carlsson, C.; Jonsson, M.; Albinsson, B. *Journal of the American Chemical Society* **1994**, *116*, 8459.

(46) Fulmer, A. W.; Benbasat, J. A.; Bloomfield, V. A. *Biopolymers* **1981**, *20*, 1147.

(47) Gouy, L. G. *J. Phys.* **1910**, *4*.

(48) Chapman, D. L. *Phil. Mag.* **1913**, *6*, 475.

(49) Williams, G. D.; Soper, A. K.; Skipper, N. T.; Smalley, M. V. *The Journal of Physical Chemistry B* **1998**, *102*, 8945.

(50) Tikhonov, A. M. *The Journal of Physical Chemistry B* **2006**, *110*, 2746.

(51) Efron, B. *The Annals of Statistics* **1979**, *7*, 1.

(52) Sun, J.; Velamakanni, B. V.; Gerberich, W. W.; Francis, L. F. *Journal of Colloid and Interface Science* **2004**, *280*, 387.

(53) Tseng, W. J.; Tzeng, F. *Colloids and Surfaces A: Physicochemical and Engineering Aspects* **2006**, *276*, 34.

(54) Schellman, J. A.; Stigter, D. *Biopolymers* **1977**, *16*, 1415.

(55) Smith, S. B.; Bendich, A. J. *Biopolymers* **1990**, *29*, 1167.

(56) Verwey, E. J. W. *The Journal of Physical and Colloid Chemistry* **1947**, *51*, 631.

(57) Derjaguin, B. V.; Landau, L. *Acta Physiochim. U.R.S.S.* **1941**, *14*.

(58) Bhattacharjee, S.; Elimelech, M. *Journal of Colloid and Interface Science* **1997**, *193*, 273.

CHAPTER 5

CHARGED COLLOIDAL PARTICLES AS AN IN SITU PROBE FOR PHOTO-INDUCED CHARGING AT A SEMICONDUCTOR INTERFACE

5.1 Introduction

Semiconductor optically transparent electrodes are valuable tools which allow simultaneous spectrometric and electrochemical characterization of chemical processes at interfaces. Transparent electrodes have been used spectroscopically to detect electrochemically generated species[1] and to study electrochemical kinetics. Transparent semiconductors have also been used to study photophysics in fluorescent molecules, such as photo-induced electron transfer between semiconductors and single fluorophores,[2-4] and the effects of local electric field on fluorescence emission.[5-7] Recently, optically transparent semiconductors have been used in biosensors that allow simultaneous fluorescence and electrochemical detection of biomolecules. In addition, control of electrical potential at the electrode surface allows for regenerable biosensors via electrostatic desorption[8,9] and electrostatic immobilization of biomolecules.[10]

Spectroelectrochemistry at semiconductor interfaces presents challenges, however, since the light used for spectroscopic detection may also excite electronic transitions in the semiconductor and lead to undesirable behavior, such as shifts in surface potential or conductivity. In this work, we report photo-induced shifts in the

electrical potential of a transparent semiconductor electrode, indium tin oxide (ITO), by radiation with photon energy below the primary band gap. Charged 100 nm particles are used as an *in situ* probe of electrical potential in the electrical double-layer of an ITO-aqueous interface. The particle population in a 150 nm interfacial evanescent field region was quantified by counting fluorescent carboxylate-terminated polystyrene particles in images collected using total internal reflection fluorescence microscopy. The population of charged colloidal particles at the ITO interface increases with positive applied potential, and a Poisson-Boltzmann model describes the population response in terms of its potential sensitivity and an onset potential for accumulation. By increasing the 488 nm illumination intensity at the interface, particle population versus applied potential curves shifted to less positive applied potentials, indicating a build-up of positive charge at the ITO interface. A kinetic model relating the rates of photoinduced charge separation and charge recombination suggests that photoexcitation is one-photon, and is possibly the result of photoexcitation into an indirect band-gap or photoexcitation of defect sites into the direct band gap of ITO. Potential scans with red-absorbing fluorescent particles imaged with 647 nm illumination far outside the ITO indirect band-gap and defect energy gap show only weak shifts in potential with illumination intensity, confirming the photoinduced charge separation hypothesis.

5.2 Experimental Section

5.2.1 Chemicals and Materials

Carboxylate-modified Fluosphere fluorescent microspheres were purchased from Invitrogen (Carlsbad, CA) as suspensions in water at 2 weight percent. "Yellow-green" microspheres with 100-nm nominal diameter had fluorescence excitation and emission

maxima of 505 and 515 nm respectively, and “dark red” 200-nm microspheres had excitation and emission maxima of 660 and 680 nm. All buffers and solutions were made using water purified with a Barnstead NANOpure II system (Boston, MA) to a solution resistivity of approximately 18 MΩ·cm. Indium tin oxide (ITO) sputter-coated 22 x 22 mm No. 1 glass coverslips (sheet resistivity of 15-30 Ω/square) were purchased from SPi Supplies (West Chester, PA). Buffers and supporting electrolyte solutions were made with ACS grade sodium phosphate monobasic monohydrate, sodium chloride, and sodium hydroxide from Mallinckrodt (Phillipsburg, NJ). Spectroscopy grade Omnisolv methanol from EMD chemicals (Darmstadt, Germany) was used for cleaning ITO coverslips. Conductive silver epoxy resin, and Gold Seal glass 22 x 22 mm no. 1.5 coverslips were purchased from VWR (West Chester, PA).

5.2.2 Microsphere Solutions

Before use, microspheres were first sonicated for 15 min in a Fisher Scientific FS-28 ultrasonic bath to break up any aggregates. Microsphere solutions for imaging experiments were prepared by serial dilutions of 2 % microsphere suspensions into deionized water, followed by a final dilution into 75 μM pH 8.0 phosphate buffer and 75 μM sodium chloride (approximately 0.3 mM ionic strength). The concentration of fluorescent microspheres used for imaging was 5 pM for “yellow-green” microspheres, and 2 pM for “dark red” microspheres. Buffers used to dilute bead suspensions were filtered with a 0.2 μm Whatman Puradisc polyether sulfone 25 mm syringe filter before use to remove particulate contamination.

5.2.3 Preparation of ITO Substrates

ITO electrodes were prepared by first rinsing for 10 min each in 18 MΩ·cm water and methanol. The ITO coated side of the coverslip was then cleaned for 25 min in a UV ozone cleaner, Jelight Co. model 342. Copper wire leads were attached to the edge of the ITO coated coverslip using conductive silver epoxy resin which was then placed in a 120 ºC oven overnight to allow the conductive paste to cure. The slides with attached wire leads were then UV ozone cleaned again for 25 min and assembled into an imaging electrochemical flow cell. This cell consists of a wired ITO slide separated from a top glass plate by a silicone gasket affixed to each surface with acrylic-polyester double-stick tape (3M, model number 9495MPF). The top has an inlet port and outlet port, which allow solution flow, and access by a platinum counter electrode and a Cypress Systems (ESA, inc.) model EE009 Ag-AgCl reference electrode. Metal clips hold the flow cell onto a stainless-steel microscope-stage insert whose interior is covered with Parafilm to prevent electrical shorts to ground. A Pine model AFCBP1 3-electrode potentiostat was used to apply potentials to the ITO working electrode.

5.2.4 TIRF Microscopy

Dilute microsphere solutions at the ITO-solution interface were imaged with a Nikon TE-200 inverted microscope using through-the-objective TIRF illumination, as described in Chapter 2. Two laser sources of fluorescence excitation were used in this experiment. The blue laser source used 488.0 nm emission from a Lexel model 95 argon ion laser coupled into a single-mode polarization-maintaining optical fiber (Thorlabs) with a focusing lens (Thorlabs PAF-X-5-A FiberPort). The red illumination was 647.1-nm radiation from a Coherent Innova 90C krypton ion laser coupled into a similar optical

fiber and focusing lens (Thorlabs F240FC-B fiber collimator). Illumination light intensity between 0.1 and 15 mW from the emerging end of the optical fiber was collected by a collimating plano-convex lens, directed through a band pass filter (Semrock), and focused onto the back focal plane of the microscope objective by a second plano-convex lens. The by an oil-immersion microscope objective (60x apo TIRF 1.49 numerical aperture, Nikon) generated a collimated beam that illuminated the sample. Translating the optical fiber normal to the optical axis shifted the angle of the illumination beam relative to the ITO surface, generating total internal reflection (TIR) at the ITO-solution interface. The ~200 nm thick ITO film is not expected to impact the ability to generate an evanescent field at the ITO-aqueous interface according to calculations of the excitation radiation spatial intensity distribution versus incident angle for three-phase dielectric thin film structures.[11]

Images of the interface were acquired with an Andor iXon 897 electron multiplying charge coupled device (EMCCD) camera in a 53 x 53 μm (200 x 200 pixel) region using 15 ms integrations and 0.25-s time-lapse intervals. For images of the "yellow-green" microspheres, electron-multiplying gain was reduced from 50× to 1× to minimize variations in microsphere intensity signal-to-noise ratio (SNR) as the illumination intensity was increased. Images of the "dark red" particles exhibited higher SNR than the 100 nm "yellow-green" particles, due to their ~8 times greater volume-loaded fluorophore content. Even at the lowest excitation power density, 1 W cm^{-2}, the electron multiplying gain could not be increased above 5× in images of "dark red" particles without occasional bright particles saturating the sensor well depth. Since the electron multiplying gain can only be adjusted in integer units, there was not enough

dynamic range in gain level to compensate for the dynamic range of excitation power density required by the experiment. As an alternative method of normalizing the particle count across all excitation intensities, the intensity detection threshold in images of "dark red" particles was increased with excitation intensity to achieve a constant particle count at low applied potentials, as described below. To characterize the illumination beam profile at the sample plane, 1.0 s exposures were collected of the laser excitation beam, at 10 mW total power, internally reflected at a glass-air interface. All images were collected as 16-bit monochrome TIF image stacks using Andor Solis ver. 4.16.

5.2.5 Calibrating Illumination Power Density in Images

In order to report accurate illumination power densities in the imaging region, the diameter of the illumination beam at the sample must be calibrated. Illumination in this experiment was provided by a single transverse mode laser beam internally reflected at the ITO-aqueous interface. At the oblique illumination angles used in TIRF microscopy, the beam was elongated in the direction of reflection at the surface, resulting in an elliptical, two-dimensional Gaussian-shaped illumination region. The area of this illumination region was measured by capturing a long exposure image of the illumination beam internally reflected at a glass-air interface. The illumination beam excited background fluorescence in the glass substrate, creating an elliptical spot in the middle of the image. An empirical two-dimensional Gaussian function was fit to this background fluorescence profile using nonlinear least squares optimization to provide parameters for the center coordinate and size of the beam in both directions. Using these fitted parameters, the total laser power in any region on the surface can be determined by numerically integrating the fitted 2D Gaussian function over the dimensions of the sub-

region of acquisition and dividing it by the integral of the entire Gaussian function. The power density at the surface was thus determined from the fraction of the total beam area represented by the 53 × 53 μm (200 × 200 pixel) acquisition region at the center of the Gaussian beam profile, and multiplying that fraction by the total illumination power measured at the base of the microscope objective.

5.2.6 Image Analysis for Locating Microspheres

Image analysis was performed using custom programs written in the Matlab (Mathworks) software environment. Individual microspheres were located in TIRF images using methods described in Chapters 1[12] and 4. Briefly, microsphere spots were detected by locating 0.480 x 0.480 μm (3 x 3 pixel) regions with three or more pixels brighter than an intensity threshold, I_{thold}, set n_{std} background standard deviations, σ_{bg}, above the mean background intensity, μ_{bg}: $I_{thold} = n_{std} \cdot \sigma_{bg} + \mu_{bg}$. The microspheres imaged in this work were highly fluorescent and were detected with high signal-to-noise ratios in all images. Values for μ_{bg} and σ_{bg} were determined for each illumination intensity and camera acquisition setting by calculating the mean and standard deviation pixel value, respectively, in blank images. The intensity threshold was set between n_{std} = 6 and 20 for images of 100 nm microspheres, depending on the SNR, and resulted in consistent microsphere populations across all illumination intensities for applied potentials less than 0.6 V where a constant evanescent field population is sampled. The 200 nm “dark red” microspheres were significantly more intense than 100 nm microspheres, and n_{std} was set between 10 and 100. To calculate equilibrium populations of microspheres at each applied potential, the microsphere populations were averaged in 150 images collected 60 s after the potential step.

5.3 Results and Discussion

5.3.1 Microsphere Response to Applied Potential

The fluorescent polystyrene microspheres used in this work have a high density of carboxylate groups on their surface. In the basic pH 8.0 phosphate buffer used in this work, the microspheres are highly negatively charged, with ~1.5×10^5 carboxylate groups per particle, much like the DNA plasmids described in Chapter 4. When positive potentials are applied to an ITO electrode in contact with a suspension of microspheres, the microspheres accumulate at the interfcace as shown in Figure 5.1a. Figure 5.1a shows representative fluorescence images of carboxylate microspheres diffusing near an ITO surface 60 s after the potential had been stepped to between 0 and 1.0 V versus a Ag-AgCl reference electrode. At applied potentials in this range, particles appear to freely diffuse, and adsorption to the surface is rare. Accumulation at the interface is reversible, and populations return within 5 seconds to their original values when the potential is stepped back to 0 V. Microsphere were identified and counted at each applied potential using image analysis that requires spots in fluorescence images to exceed an intensity threshold in multiple adjacent pixels. The fluorescent microspheres were volume-labeled with thousands of fluorescent probes and could be detected at high SNR at all illumination intensities; see above for details about the detection algorithm. Figure 5.1b shows a representative plot of equilibrium microsphere populations versus applied potential. Populations were counted 60 s after stepping to the specified potential, and potential steps were made sequentially in increasing order from 0 V. Populations in Figure 5.1b were measured for a 5 pM 100 nm diameter microsphere suspension in 75 μM phosphate buffer with 75 μM sodium chloride. When microsphere suspensions were

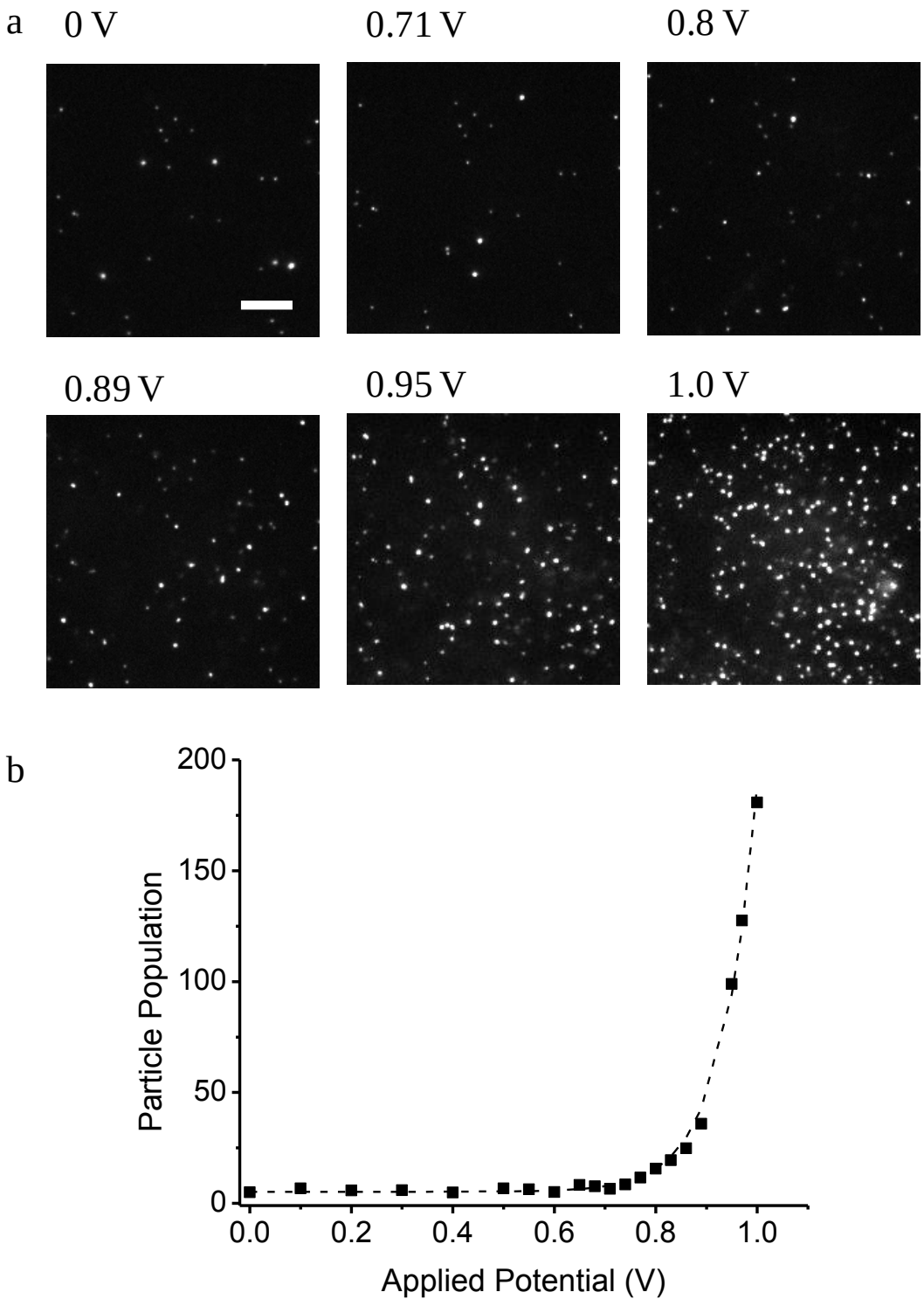

Figure 5.1. Microsphere interfacial population response to applied potential a) images of microspheres after potential step, scale bar is 10 μm, b) plot of equilibrium populations after potential step (black squares), with fit to equation 5.3 (dashed line).

initially added to the imaging flow cell, between 5 and 10 microspheres adsorbed to the surface in each imaging region. These immobile, adsorbed microspheres were excluded from the population counts because they were insensitive to applied potential.

The population of microspheres detected in the evanescent field volume, N_{DET}, represents the total population of molecules in the evanescent field volume near the ITO surface. As Figure 5.1b shows, N_{DET} increases exponentially with potential beyond a threshold potential of ~0.7 V. In Chapter 4, a Poisson-Boltzmann model was developed to describe this exponential population response to applied potential. In this model, the average population of particles in the electrical double layer near the surface, N_D, is modulated by an average electrical potential, φ, according to a Poisson-Boltzmann relationship, where N^0_D is the bulk ion population, z is the charge of the particle in electron equivalents, e is the charge of an electron, k_B is Boltzmann's constant, and T is the temperature:

$$N_D = N_D^0 e^{-\frac{ze\varphi}{k_B T}} \qquad 5.1$$

The thickness of the electrical double layer is described by the Debye length, κ^{-1}, which is a function of the bulk ion concentration, C^0, the electrical permittivity of a vacuum, ε_0, and the relative permittivity, ε:

$$\kappa^{-1} = \left(\frac{\varepsilon\varepsilon_0 k_B T}{2C^0 z^2 e^2}\right)^{1/2} \qquad 5.2$$

For the buffer composition used in this experiment, κ^{-1} is ~18 nm, which is significantly smaller than the 100 nm evanescent field that defines our detection population, N_{DET}. When there is no net charge on the surface, N_{DET} is equal to the evanescent field

population at zero charge, N^0_E. We simplify the argument of the exponential expression in equation 5.1 by defining a parameter, $\beta = -ze/kT$, which describes the sensitivity of the potential response with a net electrical charge, z, for the microparticle averaged over the double-layer region. As can be seen in Figure 5.1b, a threshold potential must be reached before microspheres begin accumulating at the interface. This threshold potential is designated as the outer Helmholtz plane (OHP) zero potential, E^0_{OHP}, the potential required to neutralize charged ITO surface groups and adsorbed anions and reverse the potential at the solution side of the interface. Additional applied potential, E, is required to neutralize this excess surface charge, so that the net potential available to ions in solution is $E - E^0_{OHP}$.

Combining these modifications to equation 5.1 yields a new expression for N_{DET} as a function of applied potential:

$$N_{DET} = (N^0_E - N^0_D) + N^0_D e^{-\beta(E - E^0_{OHP})} \qquad 5.3$$

The expression for N_{DET} was fit to the particle accumulation data using a non-linear least squares search to determine values for N^0_E, N^0_D, β and E^0_{OHP}, and is plotted as the dotted line in Figure 5.1b. Uncertainties of the parameters are reported as ± 2 standard deviations, estimated using the bootstrap method[13] using simulated data sets generated by adding random residuals to a best-fit curve, where the residuals were scaled by a factor $(N_{DET})^{½}$ to account for the Poisson distribution of errors in N_{DET}. The behavior of 100 nm microspheres near ITO surfaces is generally consistent with the 400 nm diameter DNA plasmids investigated in Chapter 4 using similar techniques. The ratio N^0_D/N^0_E is the fraction of molecules in the evanescent field region that responds to potential

variation. A larger fraction of detected microspheres, $N^0_D/N^0_E = 0.5 \pm 0.1$, compared to DNA, $N^0_D/N^0_E = 0.2 \pm 0.02$ were influenced by applied potential, but this can be ascribed to several differences in instrumentation between the two experiments. First, the microparticles were imaged with a higher numerical aperture objective lens than DNA, 1.49 N. A. versus 1.45 N. A., which allows for higher total internal reflection angles, generating shorter evanescent field decay lengths and reducing N^0_E. In addition, the 100 nm microparticles are smaller than the 400 nm DNA plasmids, so that the center of a microparticle must approach closer to the interface than DNA in order for it to be detected in the evanescent field. The population of microspheres exhibit slightly less sensitivity to applied potential, $\beta = 14 \pm 2\ V^{-1}$, than DNA, $\beta = 19 \pm 1\ V^{-1}$, possibly due to differences in surface charge density of the particles compared to DNA. Overall, populations of microspheres near ITO behave qualitatively similar to populations of DNA, and are an equivalent probe of surface potential.

5.3.2 Microsphere Potential Response to 488 nm Illumination

During measurements of microsphere population response to applied potential, we noticed anomalous behavior when changing the fluorescence excitation intensity, I_{exc}, at high applied potentials. At applied potentials beyond 0.7 V, populations near the interface increased with the excitation intensity. Figure 5.2a shows a series of representative images captured at equilibrium for 5 pM 100 nm "yellow-green" microspheres near an ITO surface poised at 0.82 V illuminated by varying I_{exc} of 488.0 nm light. At potentials below 0.6 V, illumination intensity had no measurable effect on interfacial populations, while at 0.82 V, higher illumination intensity greatly increased populations, as shown in plots of microsphere population versus illumination intensity in

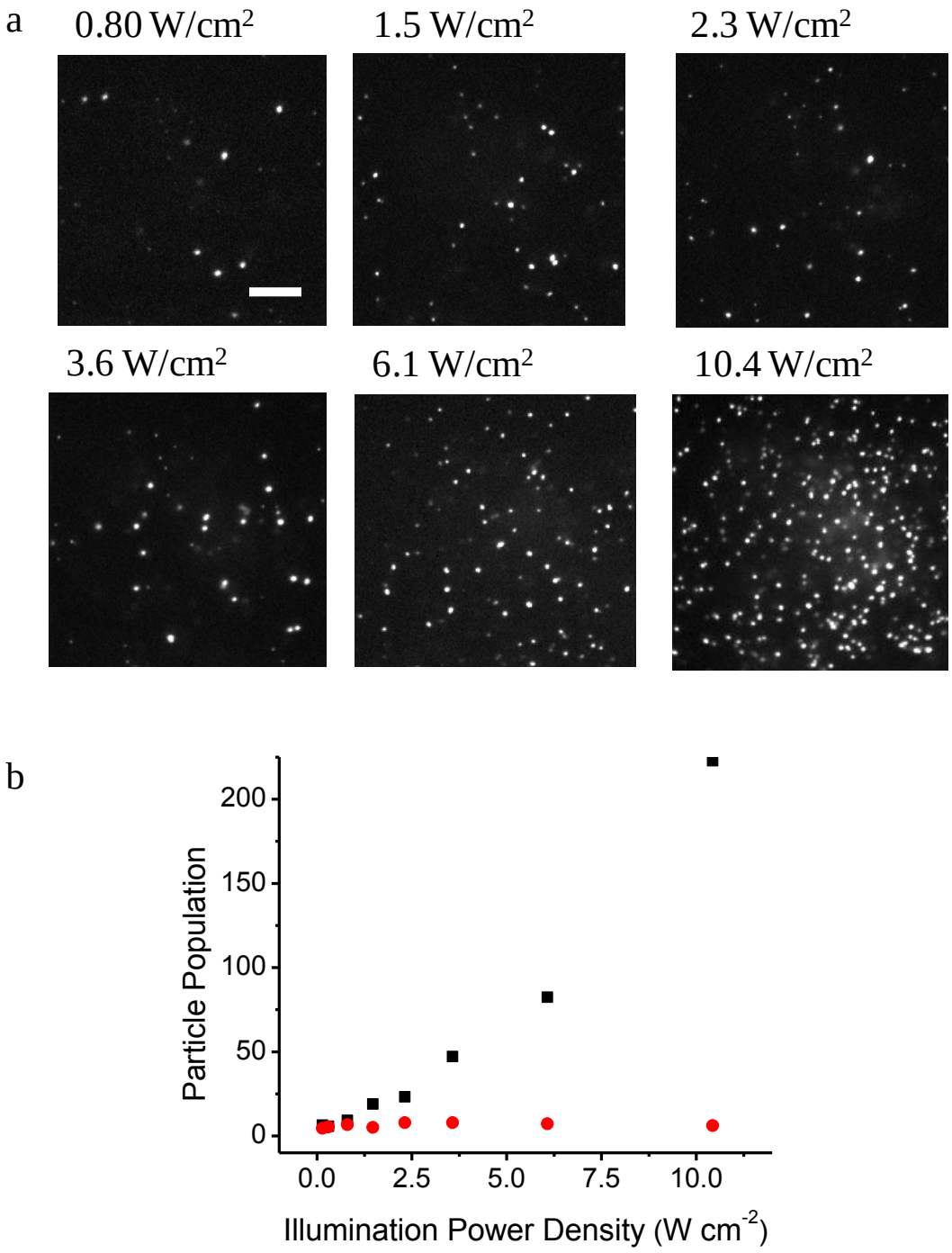

Figure 5.2. Microsphere interfacial population response to illumination intensity, a) images of microspheres at 0.82 V applied potential at varying illumination intensity, scale bar is 10 μm, b) plot of equilibrium populations at 0.82 V (black squares) and 0.6 V (red circles) at varying 488.0 nm illumination intensity.

Figure 2b. These increasing populations are not simply a result of increasing the imaging depth due to increasing the total illumination intensity, because intensity thresholds were increased in proportion to the SNR to maintain level baseline counts at low potentials. To investigate this intensity-dependent behavior in more detail, potential scan experiments were performed at varying I_{exc}, as described above. Plots of 100 nm "yellow-green" microsphere populations versus applied potential at 488.0 nm illumination intensities are shown in Figure 5.3. As these data show, increased illumination intensity appears to shift the threshold potential for accumulating particles to lower potentials, while having little impact on the sensitivity to applied potential. To account for these changes in potential response, data were fit with equation 5.3 to provide parameters describing the potential sensitivity and the potential threshold relative to illumination intensity. As shown in Figure 5.4a, the Boltzmann exponential factor, β, has no dependence on illumination intensity. Past the threshold potential for accumulation, populations of microspheres all show the same exponential dependence on applied potential. In addition, illumination intensity does not affect the fraction of molecules in the evanescent field under potential control, N^0_D/N^0_E, as shown in Figure 5.4b. The changes in microsphere potential response with illumination intensity correspond to shifts in the OHP zero potential, E^0_{OHP}. As shown in Figure 5.4c, E^0_{OHP} shifts from 0.9 to 0.6 V as the illumination power density is varied from 0.14 and 10.4 W cm^{-2}. This shift in onset potential accounts for the changes in particle populations shown in Figure 5.2a, in going from 0.14 to 10.4 W cm^{-2} illumination, the potential *relative* to the E^0_{OHP} has shifted from -0.08 V to 0.22 V, resulting in an exponential increase in population.

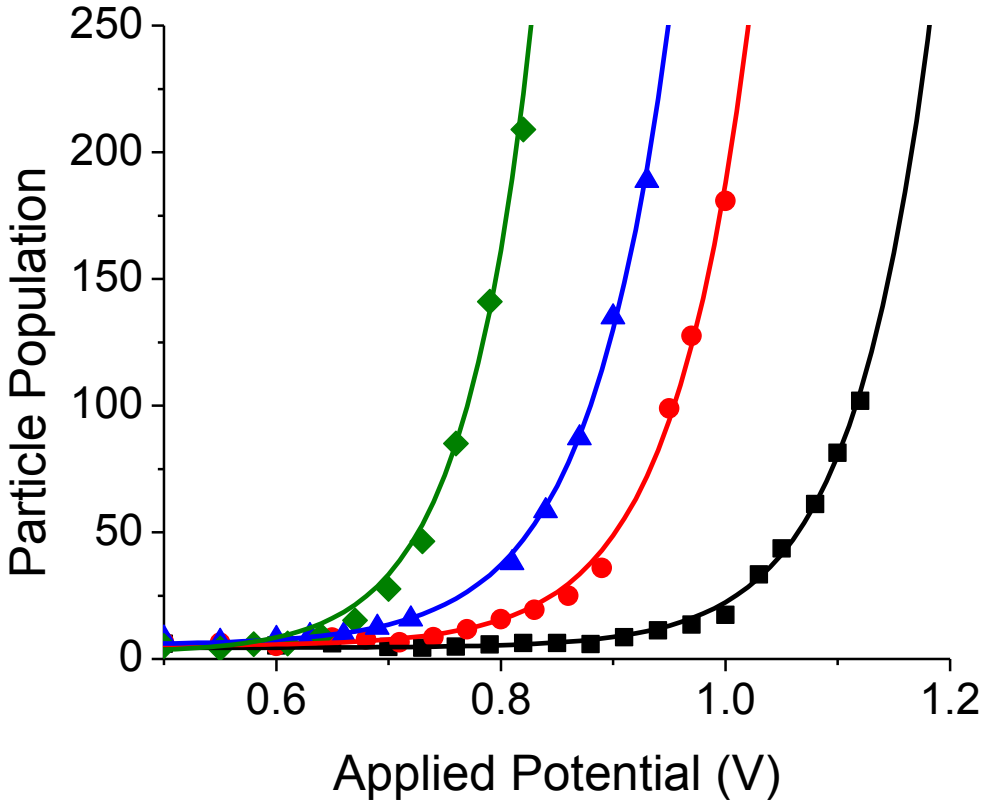

Figure 5.3. Plot of equilibrium populations versus potential for 0.3 Wcm^{-2} (black squares), 1.4 Wcm^{-2} (red circles), 3.6 Wcm^{-2} (blue triangles), 10.4 Wcm^{-2} (green diamonds) excitation illumination at 488.0 nm, with fits from equation 5.3.

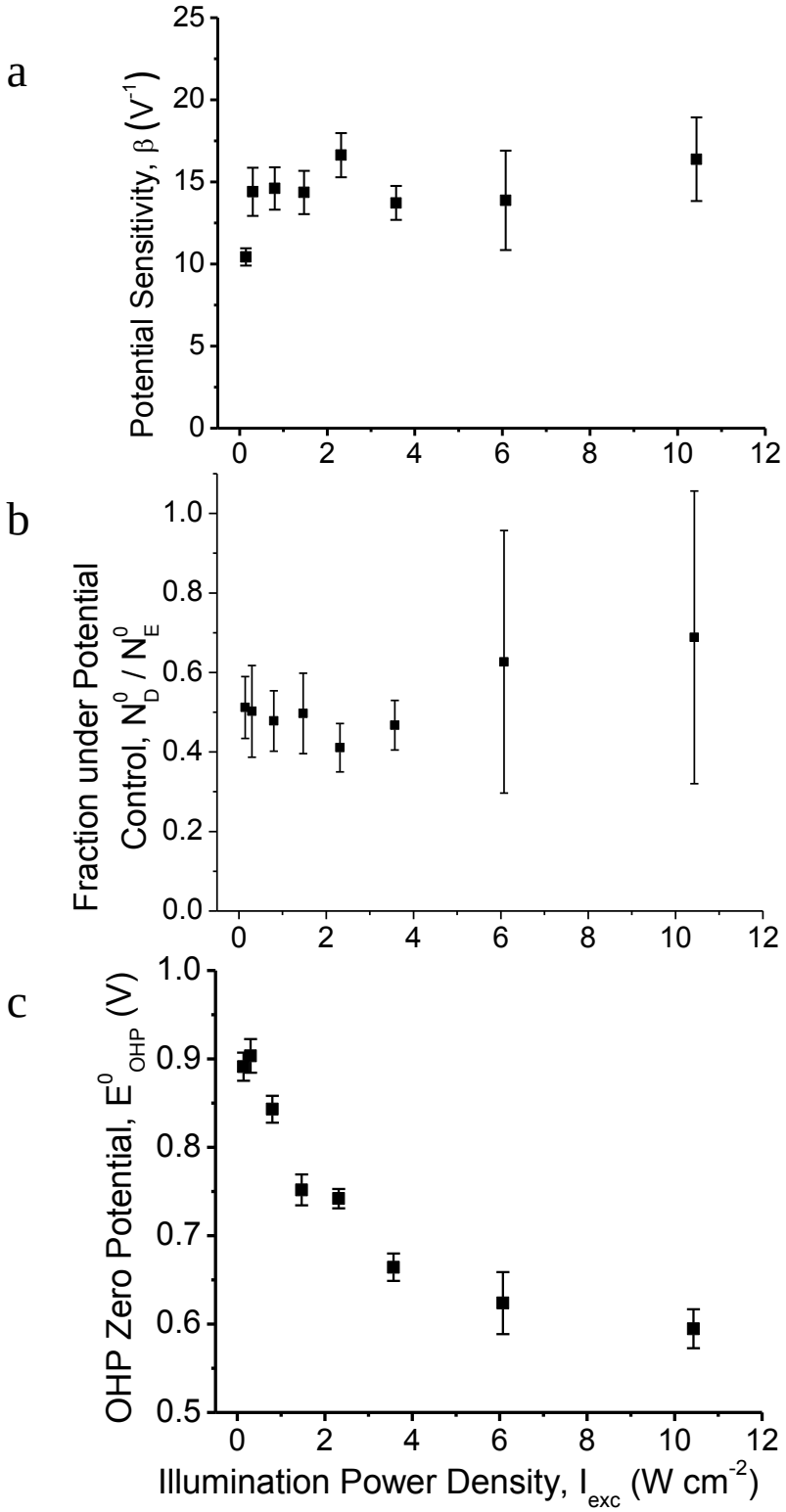

Figure 5.4. Plot of parameters from equation 5.3 for illumination at 488.0 nm, a) potential sensitivity, β, b) fraction of particles under potential control, N^0_D / N^0_E, c) OHP zero potential, E^0_{OHP}.

In our model for particle accumulation at the interface, E^0_{OHP} represents the potential needed to neutralize excess charge at the outer Helmholtz plane. The OHP is the distance of closest approach to the electrode surface for ions in solution, and it represents the thickness of an adsorbed layer of water and ions. This threshold potential is analogous to the potential of zero charge for metal electrodes,[14] and the flat band potential for semiconductor electrodes in contact with an electrolyte solution.[15] The flat band potential is the applied potential required to neutralize all charge on the electrode side of the interface, while E^0_{OHP} is the potential required to neutralize charge on the solution side of the interface. The flat band potential for ITO is approximately -0.4 V versus Ag-AgCl in neutral pH solution,[16] because of significant negative surface charge from anion adsorption[17] and anionic deprotonated surface hydroxyl groups.[18] The excess negative charge on the interface causes positive charge to build on the semiconductor side of the interface, requiring excess negative potential to neutralize this charge. Changes in interfacial chemical ion composition, such as pH, can change the density of surface charge groups and shift the flat band potential.[16] On the solution side of the interface, this excess negative charge must be neutralized with excess positive applied potential, E^0_{OHP}, to reverse the potential on the solution side and attract anions. Therefore, a shift in E^0_{OHP} with increasing I_{exc} suggests a photoinduced change in ITO surface charging and corresponding surface potential.

Optical trapping is another possible mechanism for particle accumulation at high I_{exc}. High laser intensity gradients can cause high refractive index particles migrate due to optical scattering forces.[19] Focused laser beams have been used to optically trap polystyrene particles at the center of the laser focus.[20] Because of the short decay length

of the evanescent wave, the intensity gradient normal to the interface in an evanescent field can exceed the gradient in a tightly-focused laser beam,[21] so evanescent fields could be expected to trap polystyrene particles at an interface. In the present work, however, optical trapping is not a significant contribution to particle accumulation. The power densities used for imaging produce 10^3 times smaller intensity gradients than those needed for optical trapping of this size of polystyrene particles in water.[19]

5.3.3 Photo-Induced Charge Separation in ITO

We hypothesize that shifts in E^0_{OHP} with higher illumination intensity are a result of photo-induced charging of the surface. Excitation of the direct band gap of ITO, 3.5 to 4.2 eV[22,23] (340 to 280 nm), with ultraviolet light has been used to charge ITO surfaces and drive electrochemical reactions.[24] However, in the present work, the sample is illuminated with light at much lower photon energy than the band gap. A UV-visible light absorption spectrum for the ITO film-glass coverslip samples used in this work (baseline subtracted with an uncoated glass coverslip) is shown in Figure 5.5. As can be seen in Figure 5.5, the absorbance of the ITO film does not begin to increase until below 400 nm, indicating that the band gap is far from the 488.0 nm light used for the fluorescence imaging experiments. In addition, there is little light absorption in the visible region; optical losses are due to reflection off the high refractive index surface (ITO refractive index is ~2.0), and apparent peaks in the spectrum are a result of optical interference in the ITO thin film.

Since the observed surface charging is unlikely to be due to direct band gap excitation, we hypothesize that ITO is undergoing either two-photon excitation, or one-photon excitation of the indirect band gap or lattice defect sites. This photoexcitation

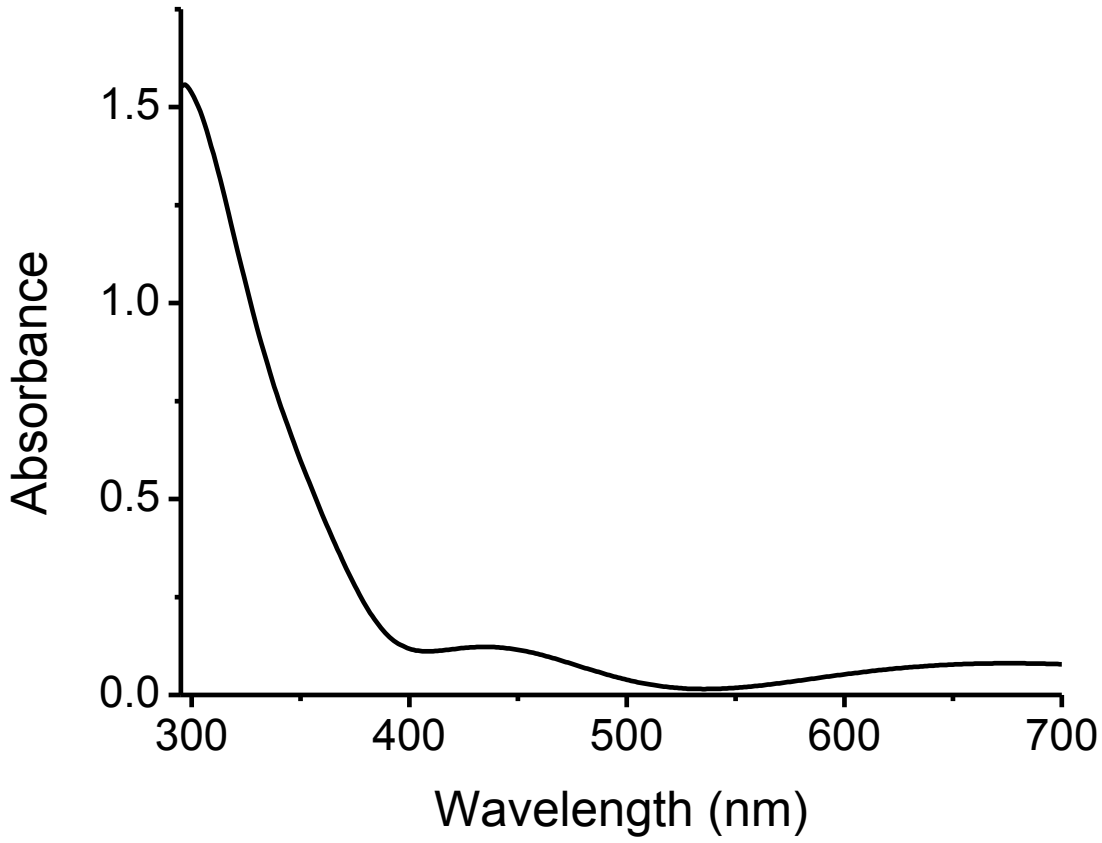

Figure 5.5. UV-Vis absorption spectrum of ITO substrate.

process generates exciton pairs of excited state electrons in the conduction band, and vacancies in the valence band of the lattice or "holes." Two-photon excitation is a non-linear optical process in which an electronic transition is excited by combining the energies of two photons resulting in a second order rate of photoexcitation with respect to photon flux.[25,26] Indirect band gap photoexcitation would correspond to single photon excitation of electrons into a conduction band with a different momentum wave vector than the valence band, following first order kinetics with respect to photon flux. Indirect transitions require a transfer of momentum from vibrational phonon modes in the lattice structure to electrons, and are typically very weak transitions, with low absorption cross sections.[27] The electron-hole pairs generated by either of these photoexcitation processes typically can relax to the ground state via non-radiative electron-hole recombination.

To determine which excitation mechanism governs photoexcitation in our samples, we have developed a kinetic model to evaluate the relative rate order of the photoexcitation and electron-hole recombination process, as outlined in Figure 5.6a. In this model, ITO lattice sites ([ITO]) absorb a number, n, of photons ($h\upsilon$), to form electron (e^-) - hole (h^+) excitons:

$$n\ (h\upsilon) + \mathrm{ITO} \rightarrow e^- + h^+ \qquad 5.4$$

The expression for the rate of hole generation in the absence of charge carrier saturation of the ITO is given by:

$$\frac{d[h^+]}{dt} = k'_1[\mathrm{ITO}][h\upsilon]^n = k_1[h\upsilon]^n \qquad 5.5$$

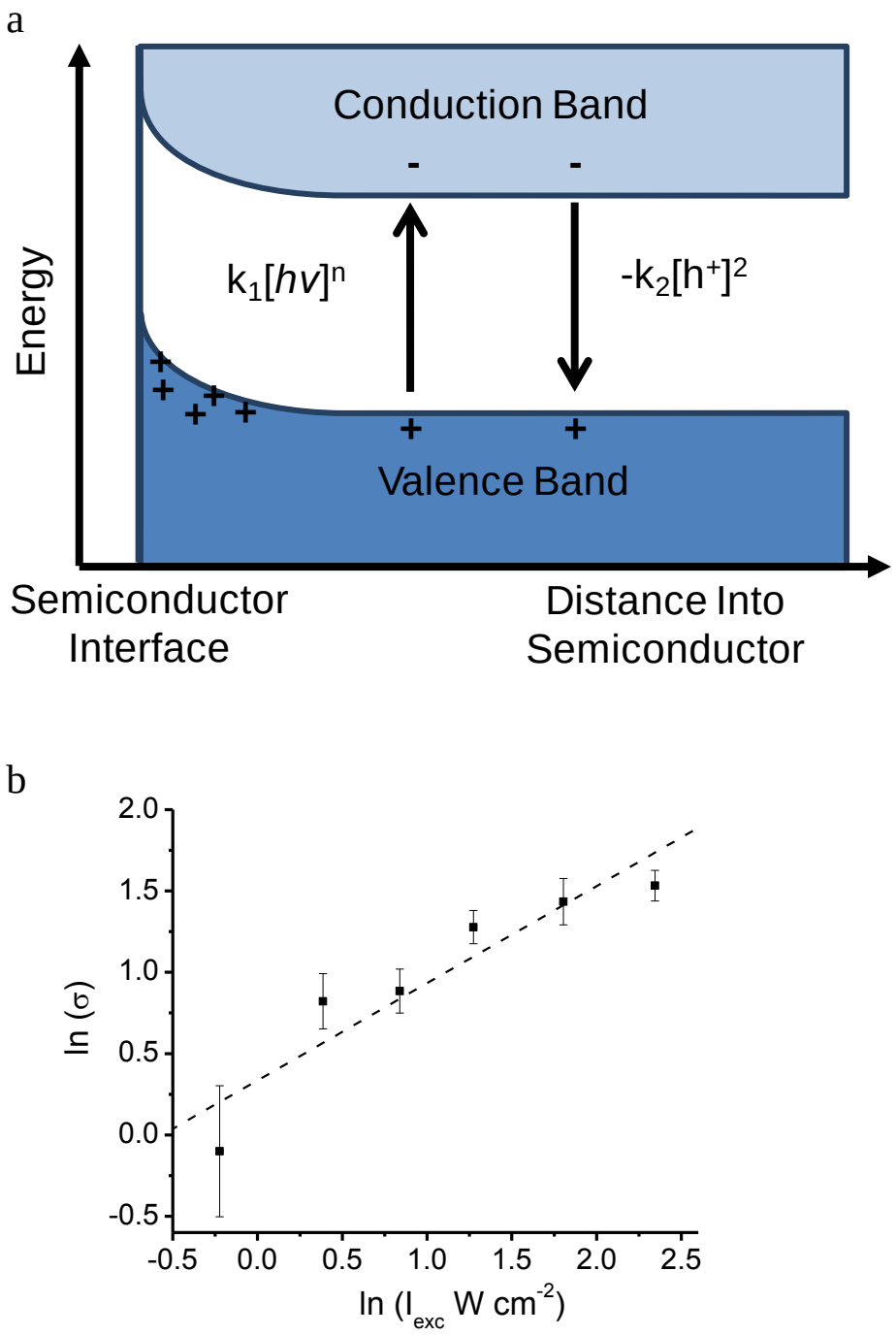

Figure 5.6. Photoexcitation model for ITO surface charging a) Diagram of photoexcitation model, see text for details, b) plot of the natural log of the charge density (μC cm^{-2}) versus the natural log of the illumination intensity (W cm^{-2}), with linear least squares fit (dashed line).

Due to the negative charge on the ITO surface, holes migrate to the space-charge layer at the electrode surface, neutralizing negative surface charge and shifting E^0_{OHP} to more positive potentials. At the interface, excitons can be destroyed via electron-hole recombination, which is typically a nonradiative process that occurs at the numerous lattice defect sites in amorphous semiconductors like ITO:

$$e^- + h^+ \rightarrow [ITO] \tag{5.6}$$

Since electrons and holes are generated by the same process, the concentration of electrons is equivalent to the concentration of holes. The resulting rate expression for electron hole recombination with rate constant k_2 is:

$$\frac{d[h^+]}{dt} = -k_2[h^+][e^-] = -k_2[h^+]^2 \tag{5.7}$$

At steady-state, the rate of hole generation and exciton recombination is zero:

$$k_1[h\upsilon]^n = -k_2[h^+]^2 \tag{5.8}$$

The excess hole concentration, $[h^+]$ during photoexcitation is equivalent to the excess charge density, σ, near the interface, and the photon flux is proportional to the excitation intensity, I_{exc}. By taking the natural logarithm of equation 5.8, we get a linear expression that tells us the order of the exciton generation process in terms of photon flux and excess surface charge density:

$$\ln([\sigma]) \propto \frac{n}{2} \ln([I_{exc}]) + \frac{1}{2}[\ln(k_1) + \ln(k_2)] \tag{5.9}$$

The experimentally measured shift in surface potential, was determined by subtracting E^0_{OHP} for each illumination intensity from its value at low light limit, $E^0_{OHP} \approx$ 0.9 V. Surface charge density was estimated by multiplying the shift in potential by a typical Helmholtz layer capacitance[14] of 15 μF cm^{-2}. We can estimate the order of this process in photons, n, from the slope of a plot of ln(σ) versus ln(I_{exc}). This plot is shown in Figure 5.6b and from the slope of a line fit using linear least squares, n = 1.2 ± 0.4, suggesting the photoexcitation process is first order in photon flux. This result is plausible, because two-photon absorption processes have low absorption cross section typically require 10^6 greater illumination power densities than that used in this work.[28] A one-photon process is possibly consistent with indirect band gap excitation, since researchers have reported indium oxide indirect band gaps between 450 to 500 nm,[29-31] close to our 488 nm excitation wavelength. However, density functional theory calculations predict that there is no indirect band gap near 500 nm, and that light absorption in the visible spectrum is the result of photoexcitation of surface states and defects caused by the high level of n-type doping in ITO.[32] Whether the photoexcitation is due to an indirect band gap or defect sites, photoexcitation is still expected to be a one-photon process, and it has been reported that photoexcitation rates decrease significantly with decreasing excitation photon energy.[33]

5.3.4 Microsphere Potential Response with 647 nm Illumination

If the apparent charging of the ITO-solution interface is a result of photoexcitation by photon energy in the indirect band gap, or defects with energy near 2.5 eV (488 nm), we would expect illumination with photon energy far below the indirect band gap or the defect energy gap to have a negligible effect on surface charge. To test this hypothesis,

the potential-controlled microsphere accumulation experiment was repeated with 647 nm excitation. In this experiment, populations of 200 nm "dark red" fluorescent carboxylated-polystyrene microspheres were counted near an ITO surface at potentials between 0 and 1.6 V versus a Ag-AgCl reference electrode. The "dark red" microspheres had similar high charge density to the "yellow-green" microspheres, with ~10^6 carboxylate groups per microsphere. Supporting electrolyte and buffer concentration were the same used to image "yellow-green" micrsospheres, and the particle concentration was 2 pM. Potential scans were performed at illumination power densities between 1 and 15 W cm^{-2}, as shown in Figure 5.7a. Equation 5.3 was fit to each curve to determine parameters describing the potential sensitivity, β, and E^0_{OHP}, which are plotted in Figures 5.7b and 5.7c, respectively. As Figure 5 shows, there is little sensitivity in either β or E^0_{OHP} to illumination intensity far below the indirect band gap, suggesting that shifts in E^0_{OHP} are indeed due to a photoexcitation process, and providing further evidence that there is no optical trapping by the evanescent field.

5.4 Summary

In this work, we demonstrated the use of charged fluorescent polystyrene microspheres as probes of surface charge density by measuring particle populations attracted to an ITO electrode with applied potential. The population response to potential was fit by an empirical function which provides parameters describing the potential sensitivity and the onset potential for particle accumulation. Increasing excitation intensity shifted the threshold potential for particle accumulation to more positive potentials, while the potential sensitivity of particle accumulation was unaffected. We attributed the shift in onset potential to photo-induced charge separation in ITO, which

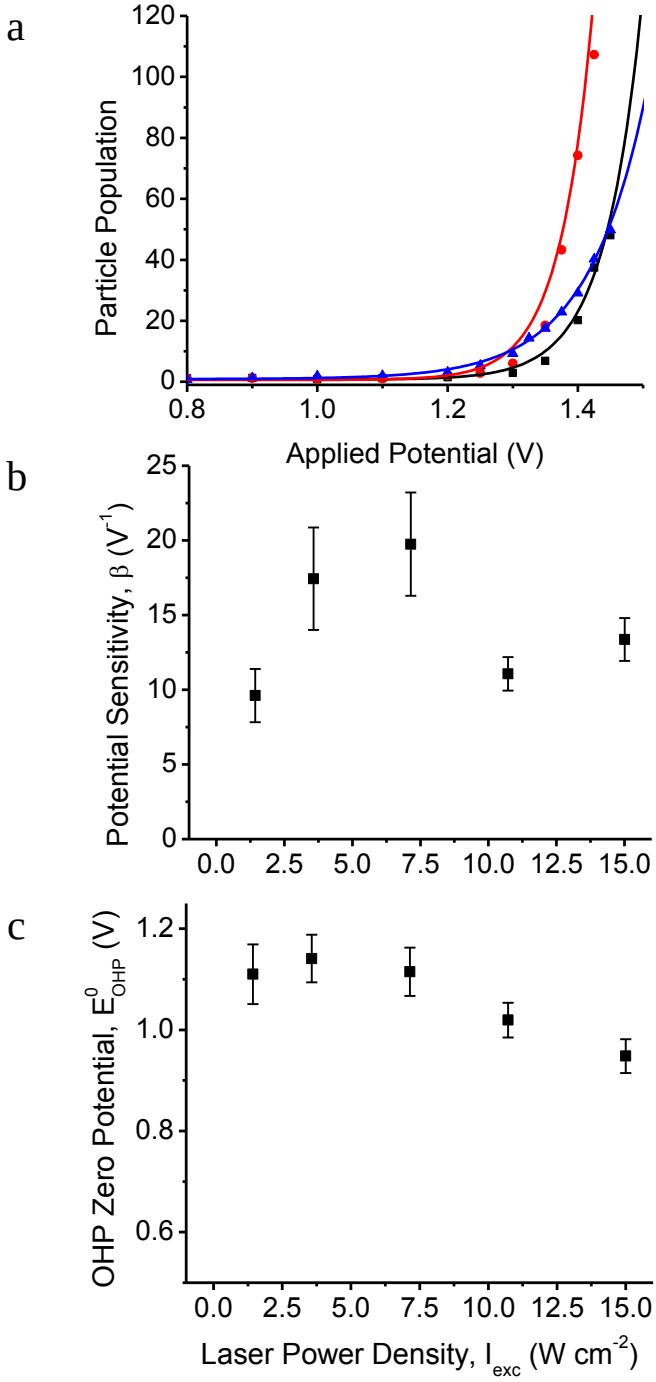

Figure 5.7. Red excitation absorbing 200 nm particles illuminated with 647 nm light, a) plot of population versus applied potential at 3.6 W cm^{-2} (black squares), 7.1 W cm^{-2} (red circles), and 10.7 W cm^{-2} (blue triangles) with fitted functions from equation 5.3, b) potential sensitivity, β, and c) OHP zero potential, E^0_{OHP} from fit to equation 5.3.

caused positively charged holes to accumulate at the interface. From a steady-state kinetics analysis of the change in surface charge density versus photon flux, the surface charging is consistent with one-photon photoexcitation of the indirect band gap or defects sites. The photoexcitation hypothesis was confirmed by a control experiment which showed no photo-induced charging of the interface by radiation having photon energies well below the indirect band gap (or defect energy gap). The illumination intensity used this work is typical for fluorescence imaging measurements, and illumination wavelengths below 530 nm are commonly used to image fluorophores such as FITC,[34] Alexafluor 488,[35] cy3,[36] and green fluorescent protein[7,9] near ITO surfaces. Our results suggest that moderate illumination intensities influenced the surface charge density of ITO, shifting surface potentials by as much as 0.3 V with power densities between 6 and 10 W cm^{-2} (see Figure 5.4c). For this reason, low excitation intensities and fluorescence excitation sources above 600 nm are recommended to avoid unwanted photoexcitation of ITO and shifting of its surface potential.

5.5 References

(1) Pinyayev, T. S.; Seliskar, C. J.; Heineman, W. R. *Analytical Chemistry* **2010**, *82*, 9743.

(2) Lu, H. P.; Xie, X. S. *The Journal of Physical Chemistry B* **1997**, *101*, 2753.

(3) Palacios, R. E.; Chang, W.-S.; Grey, J. K.; Chang, Y.-L.; Miller, W. L.; Lu, C.-Y.; Henkelman, G.; Zepeda, D.; Ferraris, J.; Barbara, P. F. *The Journal of Physical Chemistry B* **2005**, *113*, 14619.

(4) Palacios, R. E.; Fan, F.-R. F.; Bard, A. J.; Barbara, P. F. *Journal of the American Chemical Society* **2006**, *128*, 9028.

(5) Ara, A. M.; Iimori, T.; Nakabayashi, T.; Maeda, H.; Mizuno, K.; Ohta, N. *The Journal of Physical Chemistry B* **2007**, *111*, 10687.

(6) Smith, T. M.; Kim, J.; Peteanu, L. A.; Wildeman, J. *The Journal of Physical Chemistry C* **2007**, *111*, 10119.

(7) Nakabayashi, T.; Hino, K.; Ohta, Y.; Ito, S.; Nakano, H.; Ohta, N. *The Journal of Physical Chemistry B* **2011**, *115*, 8622.

(8) Asanov, A. N.; Wilson, W. W.; Oldham, P. B. *Analytical Chemistry* **1998**, *70*, 1156.

(9) Luo, W.; Westcott, N. P.; Pulsipher, A.; Yousaf, M. N. *Langmuir* **2008**, *24*, 13096.

(10) Tang, C. S.; Dusseiller, M.; Makohliso, S.; Heuschkel, M.; Sharma, S.; Keller, B.; Vörös, J. *Analytical Chemistry* **2005**, *78*, 711.

(11) Hansen, W. *Journal of the Optical Society of America* **1968**, *58*, 380.

(12) Peterson, E. M.; Harris, J. M. *Analytical Chemistry* **2010**, *82*, 189.

(13) Efron, B. *The Annals of Statistics* **1979**, *7*, 1.

(14) Grahame, D. C. *Chemical Reviews* **1947**, *41*, 441.

(15) Laidler, K. J.; King, M. C. *The Journal of Physical Chemistry* **1983**, *87*, 2657.

(16) Bolts, J. M.; Wrighton, M. S. *The Journal of Physical Chemistry* **1976**, *80*, 2641.

(17) Swint, A. L.; Bohn, P. W. *Langmuir* **2004**, *20*, 4076.

(18) Donley, C.; Dunphy, D.; Paine, D.; Carter, C.; Nebesny, K.; Lee, P.; Alloway, D.; Armstrong, N. R. *Langmuir* **2001**, *18*, 450.

(19) Ashkin, A.; Dziedzic, J. M.; Bjorkholm, J. E.; Chu, S. *Opt. Lett.* **1986**, *11*, 288.

(20) Cherney, D. P.; Bridges, T. E.; Harris, J. M. *Analytical Chemistry* **2004**, *76*, 4920.

(21) Walz, J. Y.; Prieve, D. C. *Langmuir* **1992**, *8*, 3073.

(22) Mason, M. G.; Hung, L. S.; Tang, C. W.; Lee, S. T.; Wong, K. W.; Wang, M. *Journal of Applied Physics* **1999**, *86*, 1688.

(23) Kim, H.; Horwitz, J. S.; Kushto, G.; Pique, A.; Kafafi, Z. H.; Gilmore, C. M.; Chrisey, D. B. *Journal of Applied Physics* **2000**, *88*, 6021.

(24) Tansil, N. C.; Xie, H.; Gao, Z. *The Journal of Physical Chemistry B* **2004**, *108*, 16850.

(25) Kaiser, W.; Garrett, C. G. B. *Physical Review Letters* **1961**, *7*, 229.

(26) Bechtel, J. H.; Smith, W. L. *Physical Review B* **1976**, *13*, 3515.

(27) Eyring, H. *The Journal of Chemical Physics* **1935**, *3*, 107.

(28) McClain, W. M. *Accounts of Chemical Research* **1974**, *7*, 129.

(29) Weiher, R. *J. Appl. Phys.* **1966**, *37*, 299.

(30) McCann, J. F.; Bockris, J. O. M. *Journal of The Electrochemical Society* **1981**, *128*, 1719.

(31) van den Meerakker, J. E. A. M.; Meulenkamp, E. A.; Scholten, M. *Journal of Applied Physics* **1993**, *74*, 3282.

(32) Erhart, P.; Klein, A.; Egdell, R. G.; Albe, K. *Physical Review B* **2007**, *75*, 153205.

(33) Hamberg, I. *J. Appl. Phys.* **1986**, *60*, R123.

(34) Hwang, H.; Park, J.-K. *Analytical Chemistry* **2009**, *81*, 9163.

(35) Li, L.; Tian, X.; Zou, G.; Shi, Z.; Zhang, X.; Jin, W. *Analytical Chemistry* **2008**, *80*, 3999.

(36) Schlapak, R.; Armitage, D.; Saucedo-Zeni, N.; Hohage, M.; Howorka, S. *Langmuir* **2007**, *23*, 10244.

APPENDIX A

PHOTOELECTRON CONVERSION AND PHOTOBLEACHING OF RHODAMINE 6G

This Supporting Information contains a plot of mean pixel ADU counts versus pixel ADU count variance and photobleaching kinetics measured for rhodamine 6G deposited at a glass-air interface.

A.1 Pixel ADU count mean vs. variance plot

A plot of mean pixel ADU intensity counts versus pixel ADU intensity count variance was collected for 50 300 x 300 pixel images of uniform white light at image integration times between 50 and 1000 ms, as shown in Figure A.1. These data are fit well by a linear function, indicating Poisson-like behavior in the noise. Pixel ADU intensity counts, C_{ADU}, were converted to pixel photoelectron counts, C_{PE}, using the parameters determined by the linear least squares fit: $C_{PE} = (C_{ADU} - b)/a$ where $a = 6.69 \pm 0.03$ C_{PE}/C_{ADU} and $b = 115 \pm 11$ C_{ADU}.

Photobleaching kinetics of R6G adsorbed on a glass surface

R6G photobleaching was observed by collecting a video of surface-bound R6G molecules continuously illuminated by laser radiation, as described in the experimental section. The photobleaching kinetics were determined by counting single molecules remaining in each video frame and fitting that curve to a double exponential decay

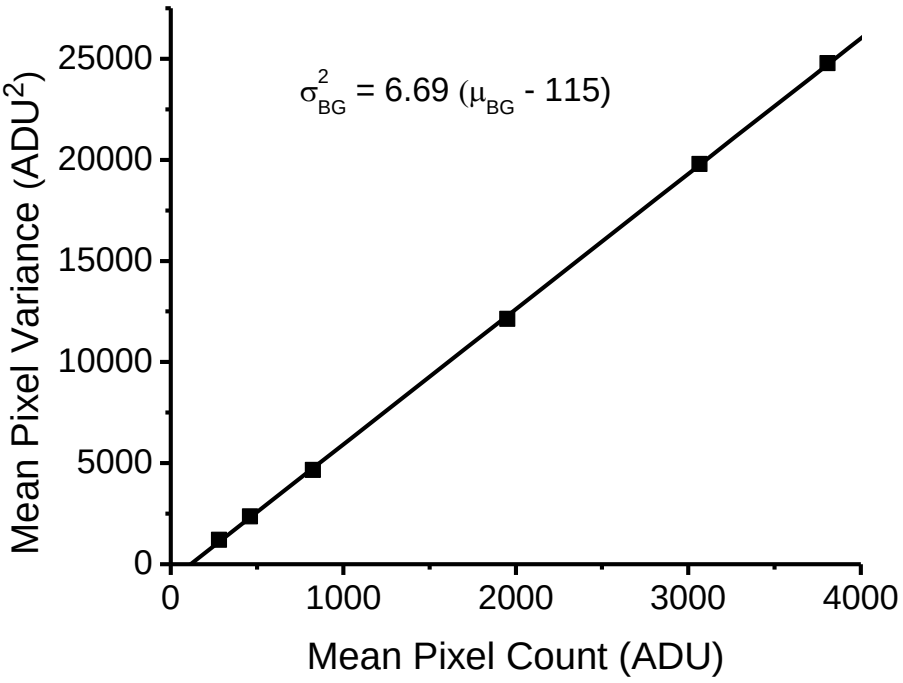

Figure A.1. ADU mean-variance plot to determine photoelectron conversion factor. I_{ADU} is plotted as black squares, and the best fit line plotted as the solid line, with equation shown.

function, as shown in Figure A.2. The two time constants determined were $\tau_1 = 4.5 \pm 0.2$ s and $\tau_2 = 70 \pm 20$ s, with a population weighted average time, $\tau_{avg} = 20$ s.

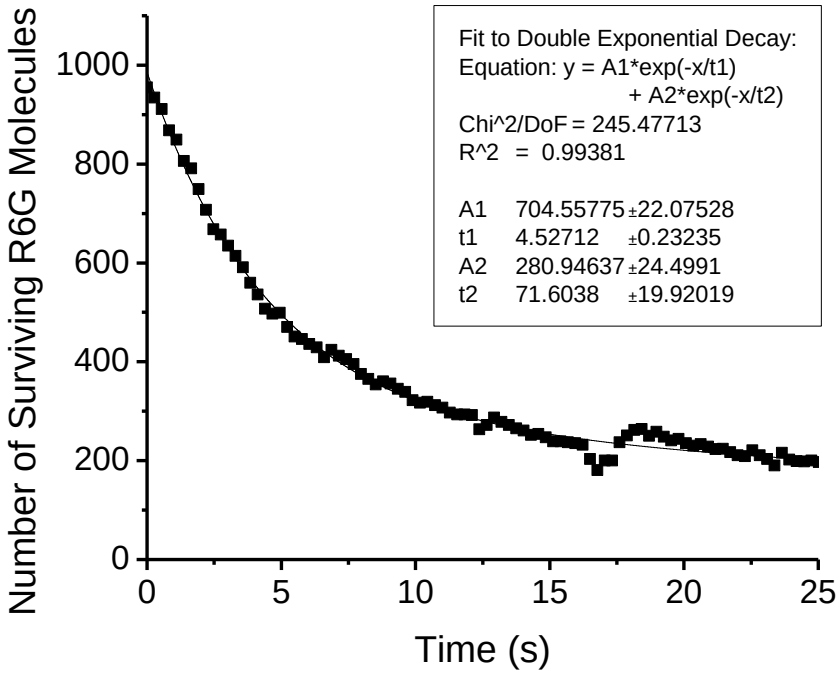

Figure A.2. Photobleaching kinetics of R6G molecules at a glass-air interface; the number of surviving R6G molecules (black squares) is plotted versus time during continuous laser illumination; the population is fit with a bi-exponential decay function (solid black line), with fit parameters shown in the inset.

APPENDIX B

DNA PLASMID INFORMATION, INTENSITY THRESHOLDS FOR FLUORESCENTLY LABELED DNA PLASMIDS, AND DNA DIFFUSION NEAR AN ITO INTERFACE

This appendix contains: B.1) A diagram of plasmid PTX21, B.2) A plot of mean pixel ADU counts versus pixel ADU count variance, B.3) Plots of mean squared displacement versus time for diffusing polystyrene particles and 14,700 bp DNA, with a plot of measured polystyrene diffusion coefficients versus particle diameter plotted with the Stokes-Einstein equation, B.4) A discussion on setting intensity detection thresholds, and B.5) Plots of mean squared displacement versus time for DNA near the interface.

B.1 PTX21 Plasmid

Supercoiled PTX21 plasmid, graciously provided by Chris Hopkins at the University of Utah, encodes a mutant variant of *C. elegans* syntaxin, a protein thought to be involved in synaptic vesicle exocytosis. The content of this plasmid is shown in Figure B.1.

B.2 Analog to Digital Unit Pixel Conversion to Photoelectrons

Images of white light noise were captured using camera readout and amplification settings from the single molecule experiments. The integration time was varied to generate white noise images of different mean pixel intensity. For EMCCD cameras, the

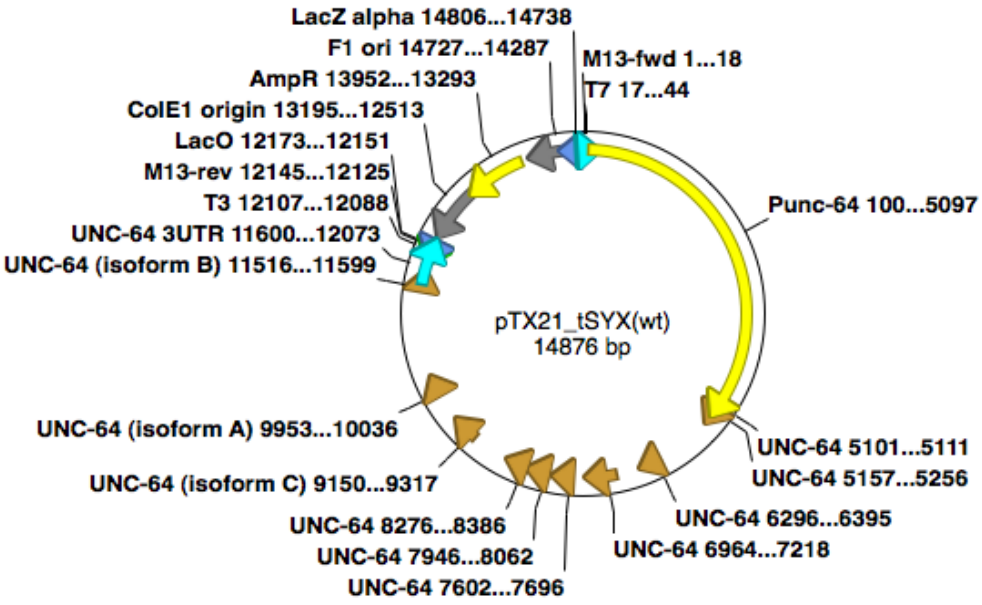

Figure B.1. DNA plasmid used for the potential control experiments.

variance of the photoelectrons counted per pixel is equal to double the photoelectron count. Pixel intensity variance, σ^2_{ADU}, in analog to digital units (ADU), is plotted versus mean pixel intensity, μ_{ADU}, in ADU in the Figure B.2. A linear function was fit (gray dashed line) in order to extract parameters for the camera offset, I_0, and the camera ADU to photoelectron conversion factor, F_{ADU}: $\sigma^2_{ADU} = F_{ADU/PE}(\mu_{ADU} - I^0)$. Fitted parameters values are $I^0 = 96$ ADU and $F_{ADU} = 7.79$. Photoelectron counts, I_{PE}, are determined from ADU counts, I_{ADU}, as follows: $I_{PE} = 2/F_{ADU}(I_{ADU} - I^0)$.

B.3 Free Solution Diffusion

Diffusion in free solution was quantified by imaging YOYO-1 labeled 1.0 pM 14,700 bp DNA solutions in 75 μM pH 8.0 phosphate buffer and 75 μM sodium chloride solution using an epi-fluorescence microscope described by Hanley and Harris.[1] DNA samples were fluorescently detected by illuminating the sample through the objective with 10 mW of 488 nm laser radiation from a Lexel model 95 argon ion laser. A 100x 1.3 N.A. oil-immersion objective was focused 10 μm beyond a coverslip into free solution to observe DNA diffusion. The DNA motion was observed by collecting 65 Hz videos (at 0.0153 ms integration time) of an 80 × 40 μm sample region (512 × 256 pixel). DNA molecules were tracked and plots of mean squared displacement versus time were generated using the same methodology described in the text, as shown in Figure B.3a. This same procedure was employed to image "yellow-green" Fluosphere carboxyl-modified fluorescently labeled latex microspheres supplied by Invitrogen (Carlsbad, CA). Latex spheres of 110 nm, 210 nm and 490 nm diameters at 0.5 pM concentration in the same buffer were imaged and tracked using the same procedure. Between 1000 and 2000 DNA or latex sphere trajectories were used to generate the plots of mean squared

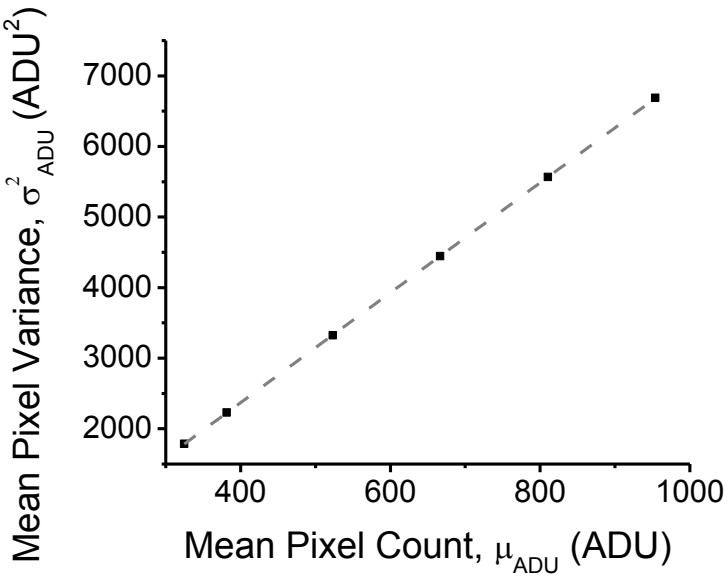

Figure B.2. Pixel variance vs. mean pixel counts (black squares) fit with linear function (dashed line) for ADU to photoelectron conversion.

a

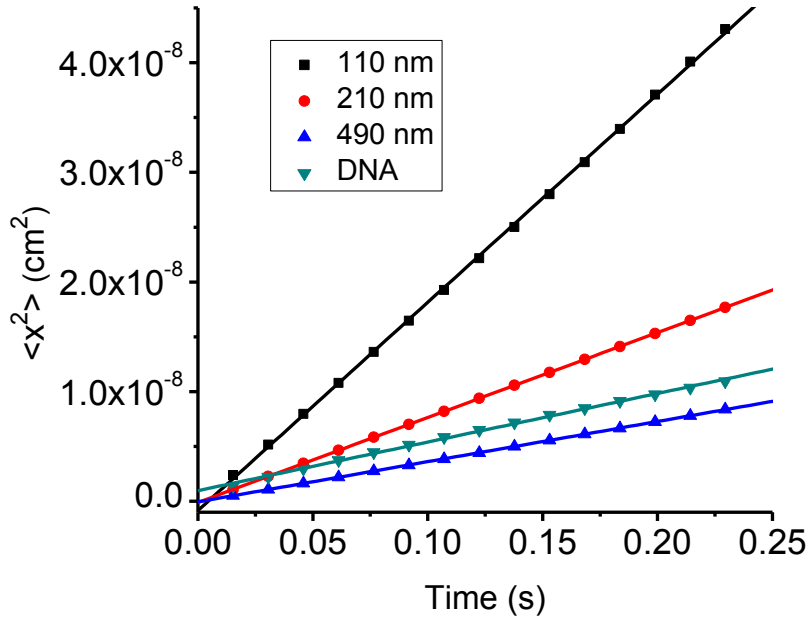

b

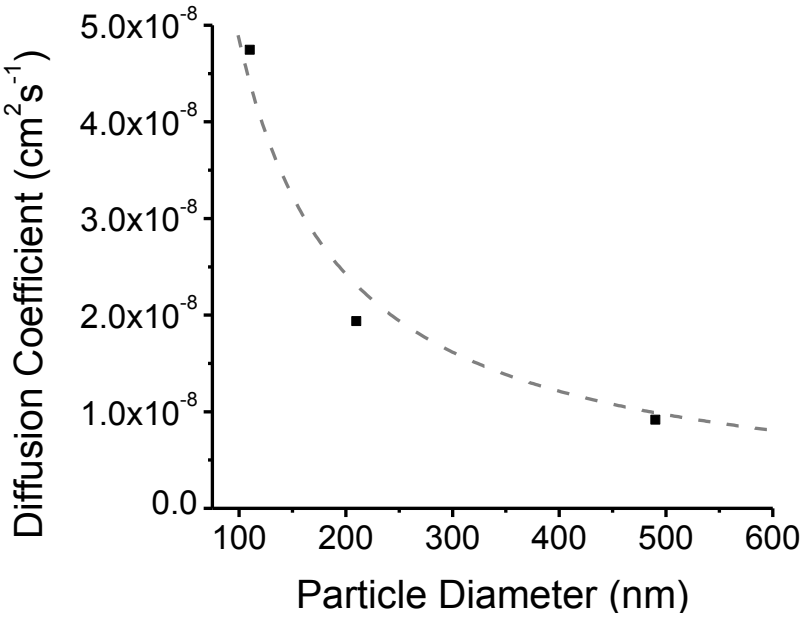

Figure B.3. Diffusion coefficients for standard particles and DNA plasmids. a) Mean squared displacement versus time for 110 nm (black squares), 210 nm (red circles), 490 nm (blue triangles) diameter spheres, and DNA (turquoise inverted triangles) and fitted lines $\langle x^2 \rangle = 4Dt$, b) microspheres diffusion coefficient plotted with the Stokes-Einstein equation.

displacement, $\langle x^2 \rangle$ in cm^2, versus time, as shown in Figure B.3a. The diffusion coefficient D was calculated from the fitted slopes: $4.75 \pm 0.04 \times 10^{-8}$ cm^2s^{-1}, $1.94 \pm 0.01 \times 10^{-8}$ cm^2s^{-1}, $0.916 \pm 0.002 \times 10^{-8}$ cm^2s^{-1}, and $1.11 \pm 0.03 \times 10^{-8}$ cm^2s^{-1} for 110 nm, 210 nm, 490 nm, and DNA, respectively. These values for D show agreement with the Stokes-Einstein equation plotted in Figure B.3b for T = 298 K and η = 0.9 cP. This curve was used to estimate the equivalent hard-sphere DNA diameter, approximately 400 nm.

B.4 Detection Intensity Thresholds

When imaging molecules diffusing through the evanescent field, the detection intensity threshold, I_{thold}, influences both the false positive probability and the detection depth into solution. As I_{thold} is reduced, the false positive probability increases as background pixel intensity randomly exceeds the threshold. Lower detection thresholds also increase the imaging depth, since dim molecules further from the surface in the low-intensity tail of the evanescent field are detected. By increasing I_{thold}, more intense DNA near to the electrode surface and the electrical double-layer is sampled, which may show more sensitivity to applied potential. Because the plasmid diameter is approximately 400 nm the ~200 nm distance of closest approach for DNA center of mass to the surface limits the maximum fluorescence intensity, barring deformation of the DNA. If I_{thold} is increased beyond the fluorescence intensity limited by the distance of closest approach, molecules are excluded from detection.

In order to select an intensity threshold, we investigated the impact of I_{thold} on the DNA population potential response. Each series of videos has different mean background intensities, μ_{bg}, so I_{thold} is described by the number, $n_{std,}$ of background standard deviations above μ_{bg}. Mean DNA populations, N_{DET}, at each applied potential

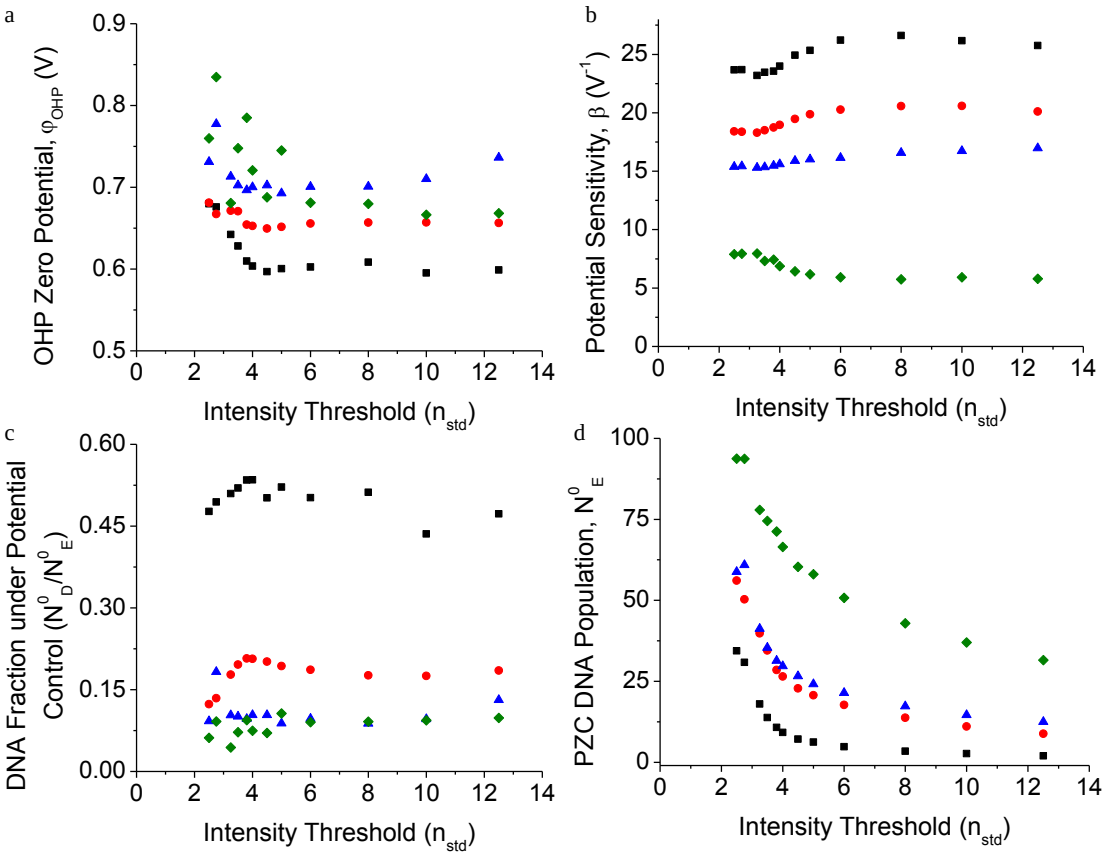

Figure B.4. Influence of detection intensity threshold on Boltzmann model parameters. a) Fitted φ_{OHP} versus intensity detection threshold, n_{std}, for 8.4 μM (black squares), 0.28 mM (red circles), 3.2 mM (blue triangles), and 30 mM ionic strength (green diamonds), b) potential sensitivity, β, versus intensity threshold, n_{std}, c) DNA fraction under potential control, N^0_D/N^0_E, d) evanescent field population, N^0_E.

were determined at varying n_{std} and fit with Equation 4. Plots of population sensitivity to applied potential, β, and the OHP zero potential, φ_{OHP}, versus n_{std} (Figure B.4a-b) show only a 15- 30% variation with increasing n_{std}. The fraction of molecules under potential control, N^0_D/N^0_E, (Figure B.4c) increases with increasing threshold for 8.4 μM and 0.28 mM ionic strength solutions, while remaining relatively constant for 3.2 mM and 30 mM ionic strength electrolyte solutions. For 8.4 μM and 0.28 mM ionic strength solutions the Debye length is within one order of magnitude of the evanescent field thickness, and increasing the detection threshold selects DNA nearer the electrode surface and within the electrical double-layer. In concentrated electrolyte solution DNA interacting with the thin double-layer is only slightly nearer to the surface compared with the entire detection volume population, resulting in insensitivity of N^0_D/N^0_E to I_{thold}.

The intensity threshold was chosen by investigating its effect on N^0_E, the fitted total detection population at φ_{PZC}, shown in Figure B.4d. The decreasing trend in N^0_E with intensity threshold was fit to a biexponential decay function for each ionic strength. The two exponential decay constants represent sampling of DNA in two different illumination environments near the surface: the evanescent field and scattered in the sample. Molecules illuminated by the low intensity scattered light fluoresce weakly, and are excluded from detection at relatively low thresholds, nstd ≈ 4.5. Much higher intensity thresholds, $n_{std} > 15$, are required to exclude intensely fluorescent molecules inside the evanescent field. The threshold was chosen so that molecules illuminated by scattered light, the population with the shorter exponential decay constant, contributed less than 5 % to the total molecule counts. The intensity threshold required for the < 5 %

scattered light population criteria increased slightly with DNA concentration, n_{std} = 5.1, 5.6, 5.6, and 6.7 for 5.3 pM, 10.5 pM, 21.0 pM and 42.0 pM DNA solutions, respectively.

B.5 Diffusion at the ITO\aqueous Interface

Plots of mean squared displacement versus time for DNA molecules diffusing near the ITO interface were generated using the method described in the main text . Imaging was performed with a 60x 1.45 N. A. oil-immersion objective and 70 × 70 μm images (256 × 256 image, pixels correspond to 2.67×10^{-5} cm on a side in the sample plane). Plots of mean squared displacement versus time for 0.0084 mM, 0.28 mM, and 3.2 mM ionic strength electrolyte solution and each applied potential are shown in Figure B.5a-c.

B.6 References

(1) Hanley, D. C.; Harris, J. M. *Analytical Chemistry* **2001**, *73*, 5030.

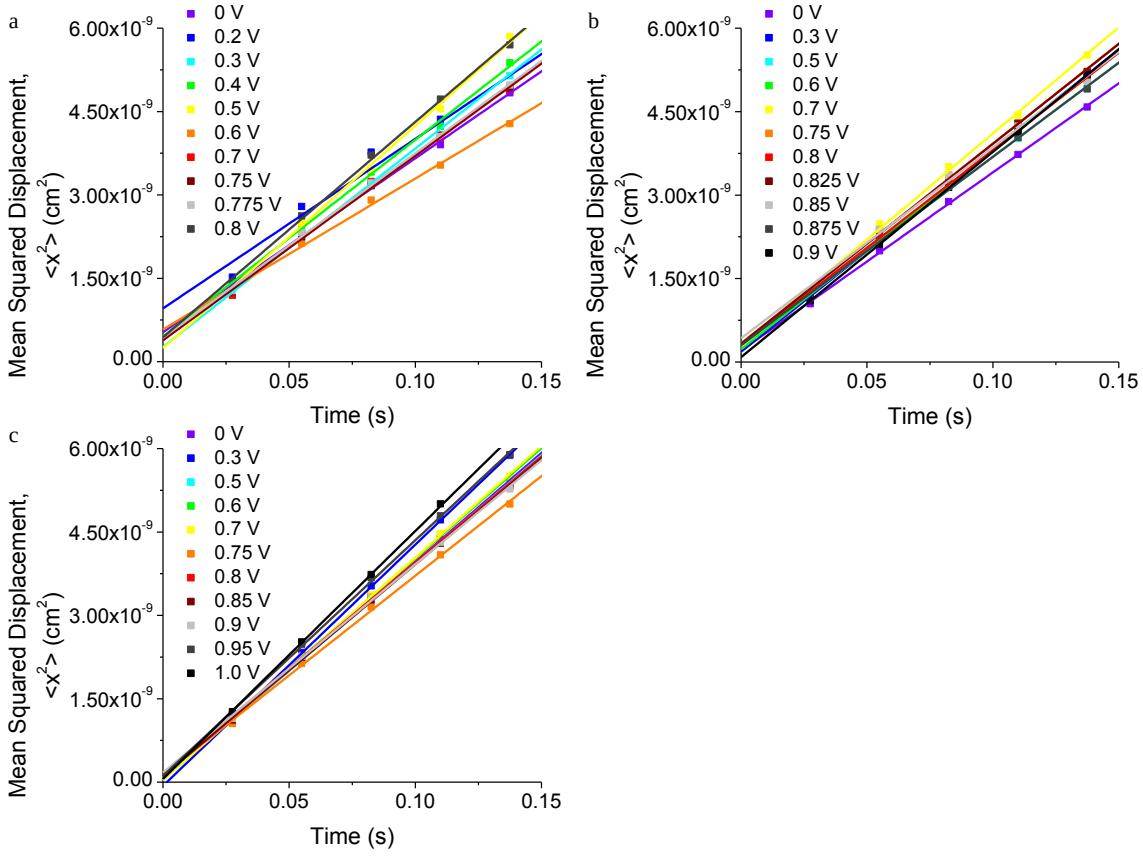

Figure B.5. Mean squared displacement versus time for DNA near the ITO interface for a) 0.0084 μM ionic strength b) 0.28 mM ionic strength, c) 3.2 mM ionic strength, with applied potential in legend.